DESIGN OF MOLECULAR OXIDE AUXETIC MATERIALS AND THEIR EFFECT ON ENERGY STORAGE

A Thesis

Presented in Partial Fulfillment of the Requirements for the

Degree of Master of Science

with a

Major in Materials Science & Engineering

in the

College of Graduate Studies

University of Idaho

by

Stuart R. Whitman

May 2014

Major Professor: Krishnan S. Raja, Ph.D.

Authorization to Submit Thesis

This thesis of Stuart Whitman, submitted for the degree of Master of Science with a Major in Material Science and Engineering and titled "DESIGN OF MOLECULAR OXIDE AUXETIC MATERIALS AND THEIR EFFECT ON ENERGY STORAGE," has been reviewed in final form. Permission, as indicated by the signatures and dates below, is now granted to submit final copies to the College of Graduated Studies for approval.

Major Professor: _____ Date: _____
Dr. Krishnan Raja

Committee Members: _____ Date: _____
Dr. Indrajit Charit

_____ Date: _____
Dr. Batric Pesic

Department
Administrator: _____ Date: _____
Dr. Wudneh Admassu

Dean of the College
of Engineering: _____ Date: _____
Dr. Larry Stauffer

Final Approval and Acceptance

Dean of the College
Of Graduate Studies: _____ Date: _____
Dr. Jie Chen

Abstract

Auxetic materials are substances exhibiting negative compressibility or negative Poisson ratios. It has been theorized that this phenomenon occurs in ceramic materials via a method of rotating polyhedrons. We hypothesize that these rotating polyhedrons lead to higher stability of materials in electrochemical systems and that this same mechanism allows for greater energy storage capacity. From molecular modeling simulations, we determined zirconium tungstate (ZrW_2O_8) to be a promising candidate for experimentation. Mixed oxide nanostructured arrays were formed on the surface of the material by anodization. Several tests including cyclic voltammetry, electrochemical impedance spectroscopy, and Mott-Schottky analysis were performed on the mixed oxide to characterize the material and its capacitance. Several annealing temperatures, two different anodization potentials, three different electrolytes, and a process involving cycling the material one thousand times were all conditions used to determine the best method of production that would lead to the greatest capacitance of the mixed oxide.

Acknowledgements

I would like to thank Dr. Krishnan S. Raja for acting as my major professor and mentor during my time as a graduate student. I would also like to thank the Department of Chemical and Materials Engineering and the University of Idaho for sponsoring my graduate studies. I acknowledge the financial support of the Defense Advanced Research Projects Agency (DARPA) through the grant YFA N66001-12-1-4252.

Dedication

This thesis is dedicated to my family, friends, teachers, and everyone else who kept me sane throughout this whole crazy process.

Table of Contents

List of Figures

List of Tables

CHAPTER 1

Synthesis of Ceramic Auxetic Materials

Unlike the rest of the chapters, this section of the thesis is not a scientific article that will eventually be published in a journal. Instead, it is a summary of several reports detailing the progress made on a project where the goal is to simulate and then synthesize and test ceramic auxetic materials. Since that is the case, an introduction to the concept of auxetic materials and a more detailed description of the project goals is probably necessary.

1. Introduction to Auxetic Materials

Auxetic materials are materials that exhibit negative compressibility. Normally, if a bar of some material is compressed along its axis, it is expected to deform outward in other directions. However, if an auxetic material is compressed, the rest of the material deforms inward. Poisson's ratio, as the relation between a material's deformations along two different axes, makes for a good measurement of compressibility, so auxetic materials have a negative Poisson's ratio.

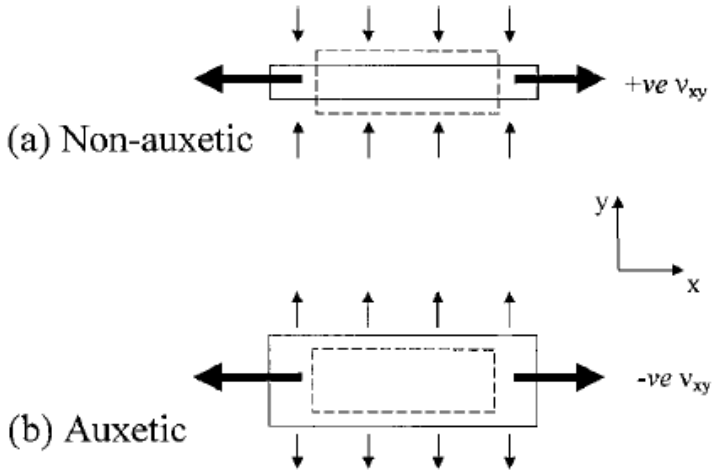

Figure 1.1: Schematic diagram of positive and negative Poisson's ratio deformation. Source: [1]

Originally developed as a novel structure for polymeric foams [2], many pure, single-crystal metals actually exhibit a negative Poisson's ratio in at least one direction. However, because this behavior usually only occurs in one direction, it is rarely ever observed in bulk materials. The alpha polymorph of cristobalite is one example of a polycrystalline auxetic material, but that is only because its single-crystal Poisson ratios are so anisotropic that even in a bulk phase the material is still auxetic [1].

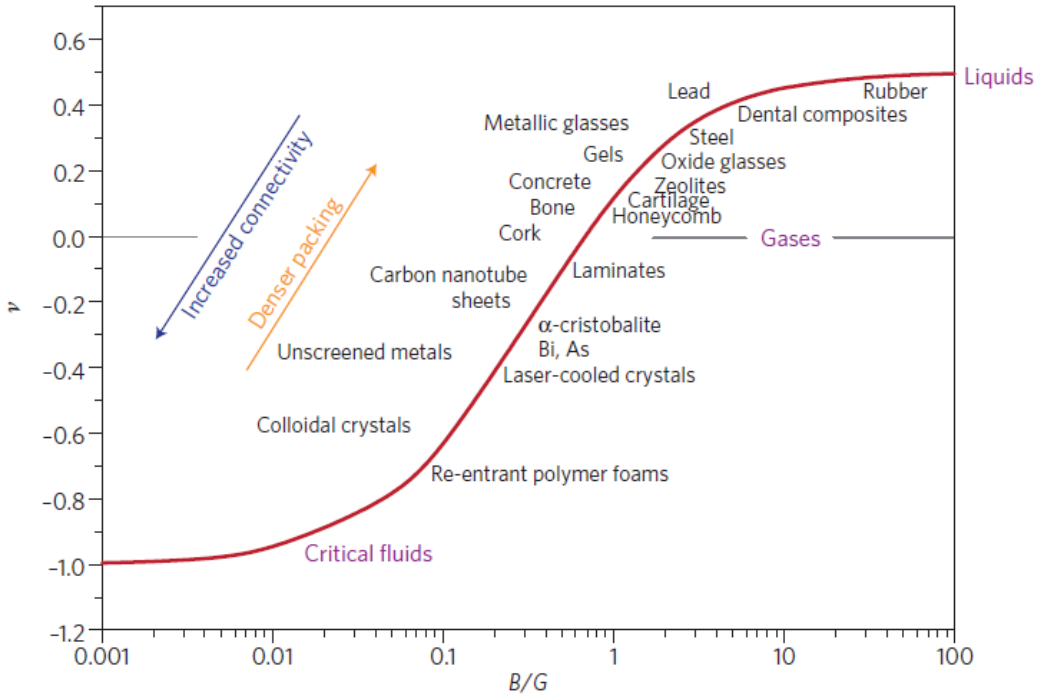

Figure 1.2: Numerical window of Poisson's ratio *ν*, from –1 to ½, plotted as a function of the ratio of the bulk and shear moduli *B*/*G* for a wide range of isotropic classes of materials; Source: [3]

The mechanism behind this behavior usually stems from one of two sources, depending on the type of material being manufactured. With polymeric foams, the microstructure has been designed in such a way that gives the material a negative compressibility. For example, a reentrant structure, like inverted honeycombs or keyed-bricks

would lead to these properties [1]. In ceramic materials, like what we are looking for, one possible mechanism is that molecular polyhedrons rotate under stress conditions. This is also the same process used to explain why some materials have negative thermal expansion [4]. In the later chapters this is part of the reason why we use ZrW_2O_8 as a material for capacitors. Auxetic behavior can be induced under electrical loads [5].

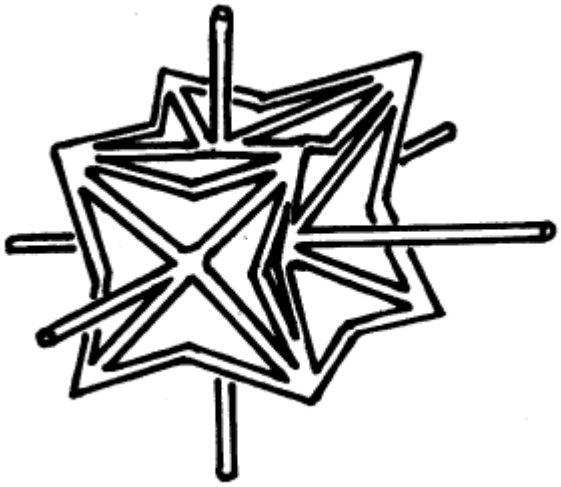

Figure 1.3: Idealized reentrant unit cell produced by symmetrical collapse of 24-sided polyhedron with cubic symmetry; Source: [2]

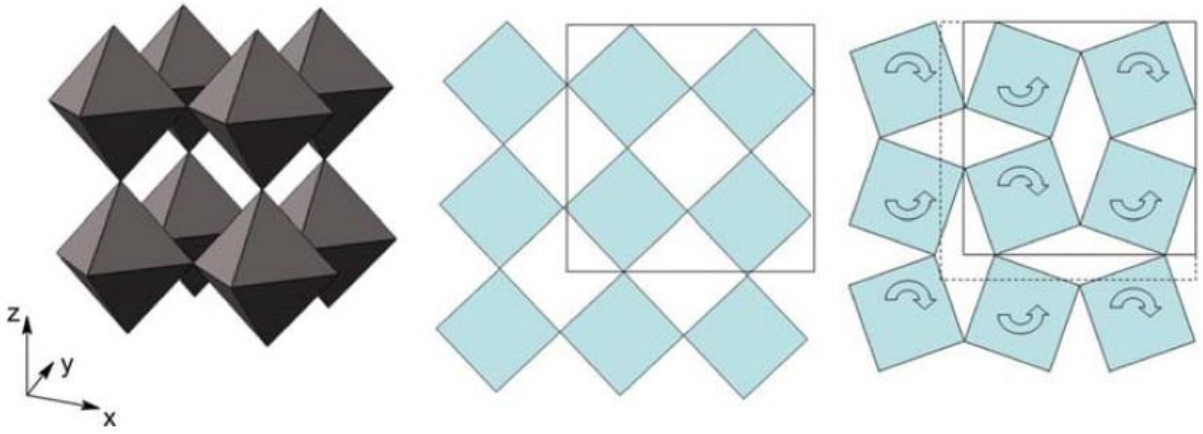

Figure 1.4: Schematic of the perovskite structure shown as octahedral units and 2D representation shown as rotating squares, indicating the rotation mechanism; Source: [8]

Obviously, a substance displaying negative compressibility has many possible and interesting applications for designer materials. For example, mixing auxetic materials with a material that has positive compressibility may result in a material with zero compressibility. As mentioned earlier, auxetic polymeric foams have already been produced, but, like most polymers, they do not handle high temperature/stress environments well. As a result the goal for this project was to find at least three ceramic materials displaying auxetic properties, synthesize and test them.

The first step of the project was to use a molecular modeling program to deduce ceramic options with potential to be auxetic materials. All the references to MS6 below are referring to Materials Studio 6.0 which is a program that consists of several modules useful for simulating and analyzing atomic and molecular structures. The modules we used were CASTEP and Forcite. There are several parameters under which these models are run. MS6's CASTEP module is used to first geometrically optimize the cell, then it calculates the elastic constants of the cell. Among these elastic constants are the Poisson ratios that are the focus of this project. CASTEP uses density functional theory (DFT) to perform the atomic-scale calculations required in this program. Specifically, it uses the Perdew-Burke-Ernzerhof functional. It performs iterative calculations until it is within a set tolerance. For all the simulations so far, the tolerances have been set to "Medium" which requires that the resulting values converge below a certain limit within 100 iterations. The limits are: Energy – 4.0×10^{-6} eV/atom; Max. Force – 0.01 eV/Å; and Max. Displacement – 4.0×10^{-4} Å. It has been noted that the 100 iteration limit may be the reason why some models fail, that it may not be enough to find the convergent solution, but more often than not the modeling process stops before the limit, so it is probably due to diverging results.

The resulting tests, data, and interpretations are given below, but the three ceramics with the most potential that we found were: zirconium tungstate (ZrW_2O_8), lanthanum niobate ($LaNbO_4$), and beta-bismuth oxide (β-Bi_2O_3).

2. Zirconium Tungstate

Materials Studio 6.0 (MS6) was used to model the elastic constants of ZrW_2O_8. Several variations and imperfections have been added to the lattice in an attempt to achieve a negative Poisson's ratio. The initial ZrW_2O_8 structure was acquired from the Crystallography Open Database (COD) which is a free online source for crystal data on many different substances. It can be found with the COD ID: 2002948. [7]

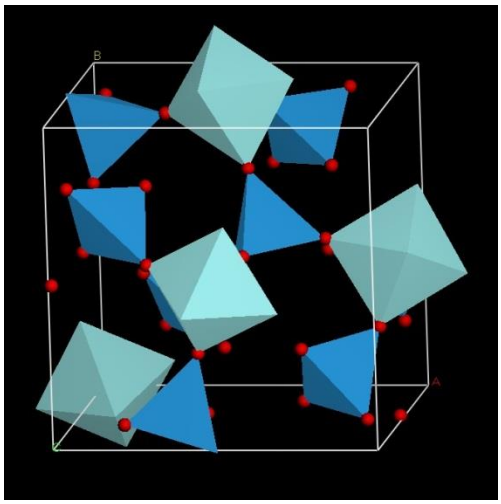

Figure 1.5: Model of ZrW_2O_8 generated from Materials Studio 6.0 with polyhedral representation; red spheres are oxygen, light blue octahedrons are ZrO_2, dark blue tetrahedrons are WO_3

Using the data from COD, a model of zirconium tungstate was constructed. It is displayed in Figure 1.5 with some of the repeating polyhedrons removed. The light blue octahedrons are zirconium oxide and the dark blue tetrahedrons are tungsten oxide. Once the

model was prepared, MS6's CASTEP module was used to, first, optimize the geometry of the system, then it was used to find the elastic constants and the Poisson ratios.

The original unit cell was altered in many different ways. Some changes involved deleting atoms, while others changed the symmetry of the system. The results are collected in Table 1.1, below. It is important to remember that for isotropic materials the limits of Poisson's ratio are $-1 < \nu < 0.5$. However, CASTEP will return values outside these limits even if the model has isotropic symmetry. Fortunately, auxetic properties are anisotropic so these limits don't matter too much anyway.

Alteration-1: The first change made to the unit cell was a small increase in the lattice size. It was performed in a mistaken attempt to get the simulated structure to match exactly the sample structure. Eventually, CASTEP failed to calculate any elastic constants, so there is nothing mentioned in the table below.

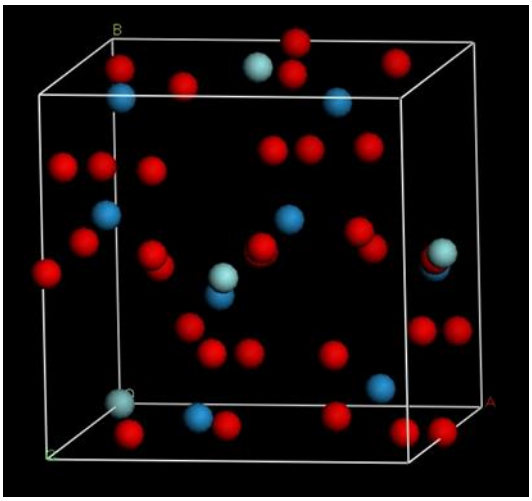

Figure 1.6: MS6 model of ZrW_2O_8 with no bonds; this is the structure used for Alteration-2

Alteration-2: All the bonds were removed from the cell to see if there would be any significant changes in the Poisson ratios. This can be seen in Figure 1.6. It was thought that,

without any bonds, it would be easier for atoms to move within the lattice. Strangely, this resulted in a dramatic increase in the Poisson ratios.

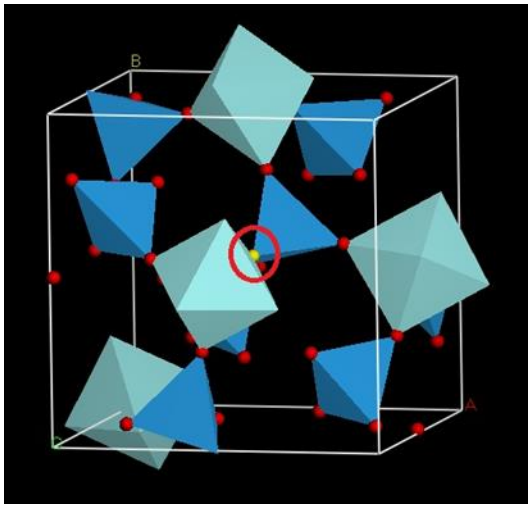

Figure 1.7: MS6 model of ZrW_2O_8 with Zr-O-W oxygen atom circled for deletion; this is the structure used for Alteration-3

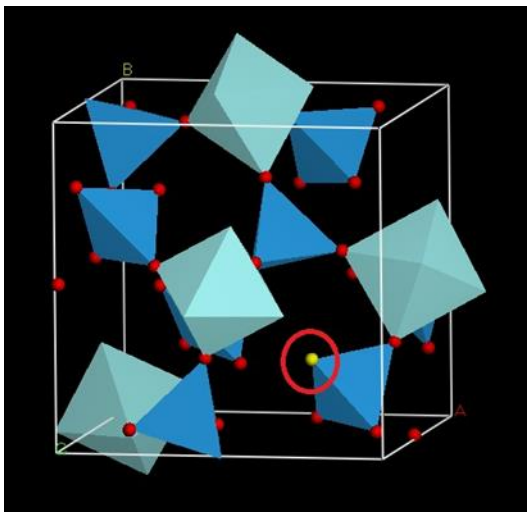

Figure 1.8: MS6 model of ZrW_2O_8 with the WO_3 oxygen atom circled for deletion; this is the structure used for Alteration-4

Alteration-3: In another attempt to enhance atomic movement, a single oxygen atom was removed from the cell to simulate a vacancy defect. Specifically, the deleted atom was one of the atoms that bridge both metal polyhedrons. (Located at X=0.56721512,

Y=0.55629025, Z=0.78665484) Figure 1.7 shows the oxygen atom that was removed from the simulation. This resulted in a decrease in Poisson's ratio in all but one direction. Unfortunately, none of the new ratios were negative.

Alteration-4: Continuing along the same train of thought as Alteration-3, a different oxygen atom was deleted from the cell. This time, it was one of the tungsten-bound atoms that is not bonded to any zirconium atoms. (X=0.73499645, Y=0.26500355, Z=0.76500355) The ratios in one direction were much closer to zero than in any previous test, but there were also some larger ratios for different directions. Figure 1.8 shows the deleted atom circled in red.

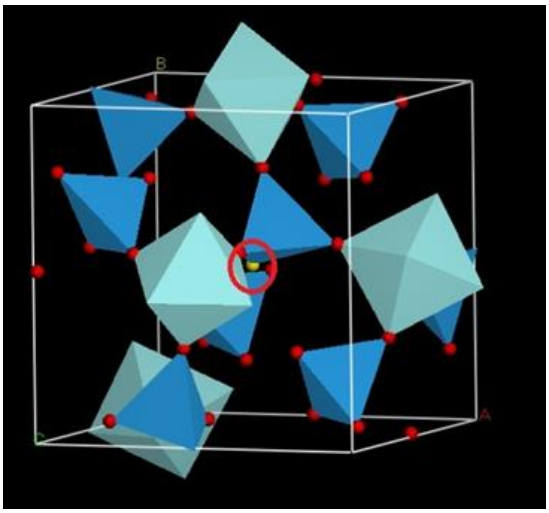

Figure 1.9: MS6 model of ZrW_2O_8 with different Zr-O-W oxygen atom circled for deletion; this is the structure used for Alteration-5

Alteration-5: In this version, much like the previous two alterations, an oxygen atom was deleted. The model is shown in Figure 1.9. The atom at the center of the unit cell (X=0.4919, Y=0.4919, Z=0.4919) was chosen for removal for no particular reason. Like the others, it did not result in any negative Poisson ratios.

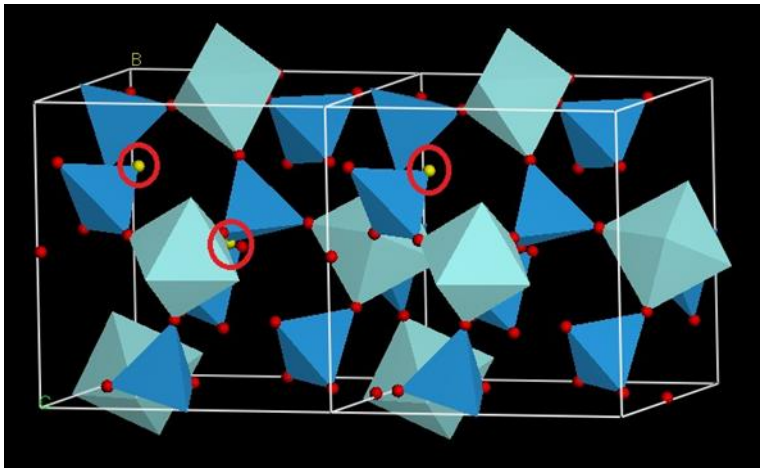

Figure 1.10: MS6 model of two ZrW_2O_8 unit cells with three oxygen atoms circled for deletion; this is the structure used for Alteration-6

Alteration-6: This condition, along with Alteration-7, was part of an effort to observe negative Poisson ratios on a larger scale than just a single unit cell. Three oxygen atoms were removed from two unit cells. Figure 1.10 shows the two cells next to each other. This was assumed to be the maximum allowable amount of vacancies. Unfortunately, the calculations were unable to converge and the Poisson's ratio for this structure could not be determined.

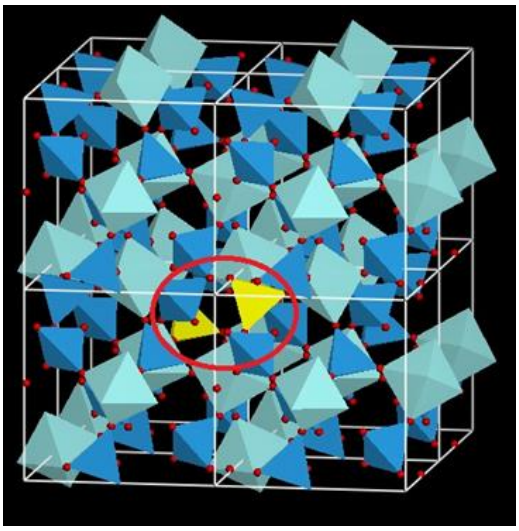

Figure 1.11: MS6 model of eight cells of ZrW_2O_8 with two WO_3 tetrahedrons circled for deletion; this is the structure used for Alteration-7

Alteration-7: Instead of simulating an oxygen vacancy in the cell, this condition simulated a metal vancancy. Eight of the unit cells were organized into one large supercell and two tungsten atoms were deleted. The deleted atoms are shown as tetrahedrons in Figure 1.11. Just like Alteration-6, the program failed to converge and no Poisson ratios were found.

After determining that deleting atoms from the cell wasn't having the desired effect on the Poisson ratios another set of tests was started that involved substituting transition metal cations in place of the regular cations to see if that resulted in auxetic behavior. Unfortunately, the results of those tests were even more unsuccessful. One of the proposed ideas to make the simulated compounds auxetic was to substitute smaller cations into the lattice in place of the metals. The rationalization was that smaller polyhedrons allowed for easier rotation of said polyhedrons and great movement in the unit cell which would, hopefully, lead to negative Poisson ratios.

Several different cations were tested at different positions in the lattices of zirconium tungstate. Titanium, vanadium and even sodium ions were placed in octahedral and tetrahedral locations in ZrW_2O_8. Unfortunately, most of the simulations failed to converge during their geometry optimization phase or their elastic constant calculation phase. All but two tests failed for ZrW_2O_8.

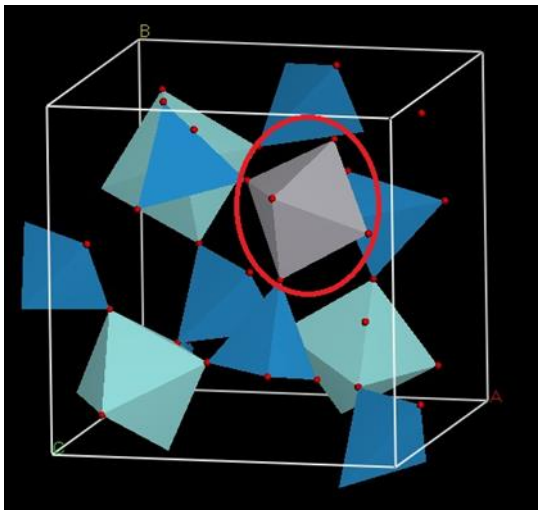

Figure 1.12: MS6 model of ZrW_2O_8 with a single Zr atom replaced with V^{3+}; this is the structure used in the Sub-OctV condition

Sub-OctV: Displayed in Figure 1.12, a V^{3+} cation was substituted in for one of the octahedral Zr cations. While the Poisson ratios, given in Table 1.1 are lower than the original's, they still aren't close to negative.

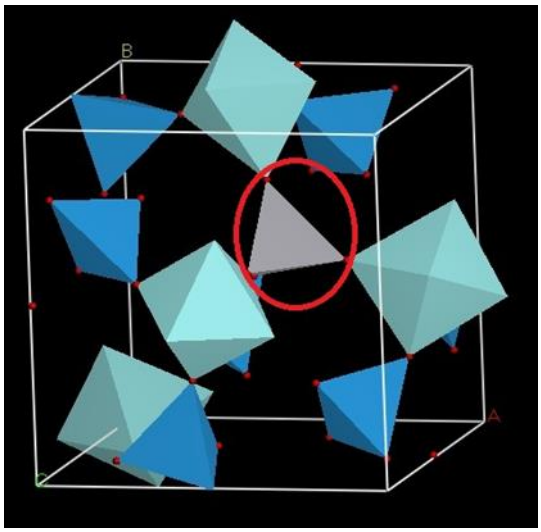

Figure 1.13: MS6 model of ZrW_2O_8 with a single W atom replaced with V^{3+} cation; this is the structure used for the Sub-TetV condition

Sub-TetV: This is just like before except a V^{3+} cation was substituted for a tetrahedral W cation (Figure 1.13). While this is much better than the previous substitution it also isn't close enough to being negative.

After several months of testing several simulations of the compound zirconium tungstate for auxetic properties, we nearly reached the conclusion that ZrW_2O_8 did not have them. Recently, the original model was re-run under the assumption that the anisotropic properties of auxetic materials meant that there was no symmetry inside the unit cell and so the cubic symmetry of the unit cell was removed. In Materials Studio 6, this is done by changing the structure of the cell from "Cubic" to P1 or "Triclinic". While there are no triclinic forms of ZrW_2O_8 that we are aware of, changing the symmetry in the program only changes the number of calculations performed instead of the actual cell structure.

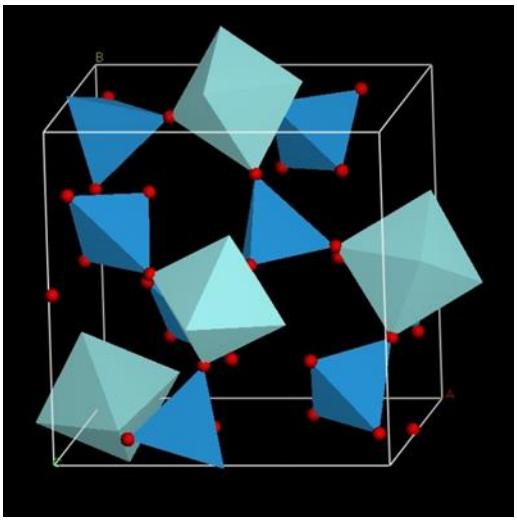

Figure 1.14: MS6 model of ZrW_2O_8

This conversion resulted in our first simulation of ZrW_2O_8 that possessed negative Poisson ratios. Admittedly, the magnitude of the ratios is not as great as in lanthanum niobate, which is mentioned later, but it still is great progress from the completely non-auxetic results generated by the previous simulations.

Table 1.1: Summary of Poisson Ratios for Zirconium Tungstate Models

	XY	YX	ZX	XZ	YZ	ZY
Original	0.3518	0.3518	0.3518	0.3518	0.3518	0.3518
Alteration-1	n/a	n/a	n/a	n/a	n/a	n/a
Alteration-2	0.5184	0.5184	0.5184	0.5184	0.5184	0.5184
Alteration-3	0.2478	0.2369	0.2403	0.3475	0.312	0.2257
Alteration-4	0.1625	0.2101	0.4375	0.3903	0.2806	0.2433
Alteration-5	0.3344	0.3344	0.2416	0.2712	0.2712	0.2416
Alteration-6	n/a	n/a	n/a	n/a	n/a	n/a
Alteration-7	n/a	n/a	n/a	n/a	n/a	n/a
Sub-OctV	0.2702	0.2671	0.2812	0.2780	0.2635	0.2696
Sub-TetV	0.1947	0.1923	0.1909	0.1894	0.1882	0.1920
ZrW_2O_8-P1	-0.0442	-0.0246	0.2122	0.8299	1.0812	0.4958

After the modeling stage of the research, ZrW_2O_8 was synthesized in the laboratory. Using the xerogel preparation method found in Noailles et al. [8], a yellow-white powder was formed (Figure 1.15). This powder was analyzed with a Siemens Diffraktometer D5000 x-ray diffractometer located in Room 322 of the McClure on the University of Idaho campus. The resulting data was then processed by the Diffrac*plus* Basic EVA 10.0 software program. The XRD pattern for the powder is shown in Figure 1.16.

Figure 1.15: Photo of powder formed via xerogel synthesis

Next, the patterns for two different crystal structures of ZrW_2O_8 were overlaid on the powder pattern. Figure 1.17 shows the cubic form of zirconium tungstate while Figure 1.18 displays the tetragonal form. Clearly neither of these patterns fit the data. Finally, the combined patterns of ZrO_2 and WO_3 are placed on the powder pattern (Figure 1.19). It fits almost perfectly.

This is most likely the result of an error during the synthesis. As part of the drying/firing process for the sol-gel technique, the intermediate needed to be heated to 1175^{o}C. However, in the temperature range from ~650-800^{o}C WO_3 can evaporate and separate from the rest of the mixture. During firing, the oven used to heat the intermediate didn't raise temperature fast enough and this resulted in the current ZrO_2-WO_3 powder.

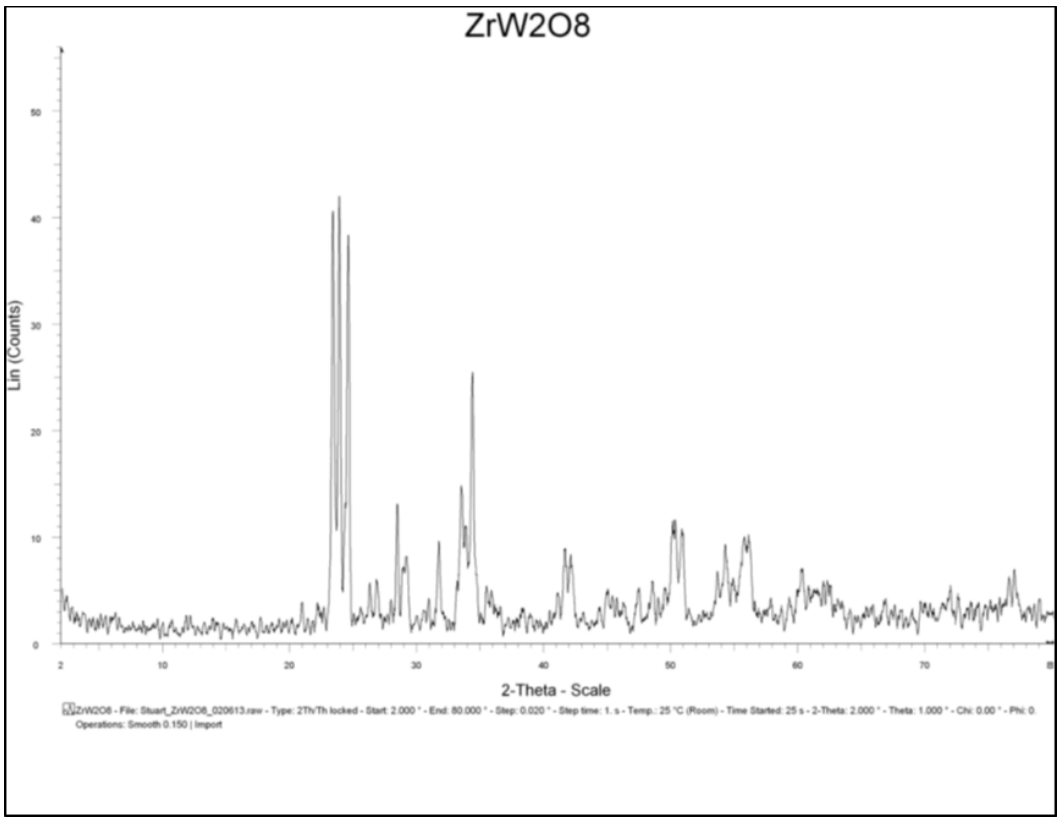

Figure 1.16: XRD pattern of the synthesized powder

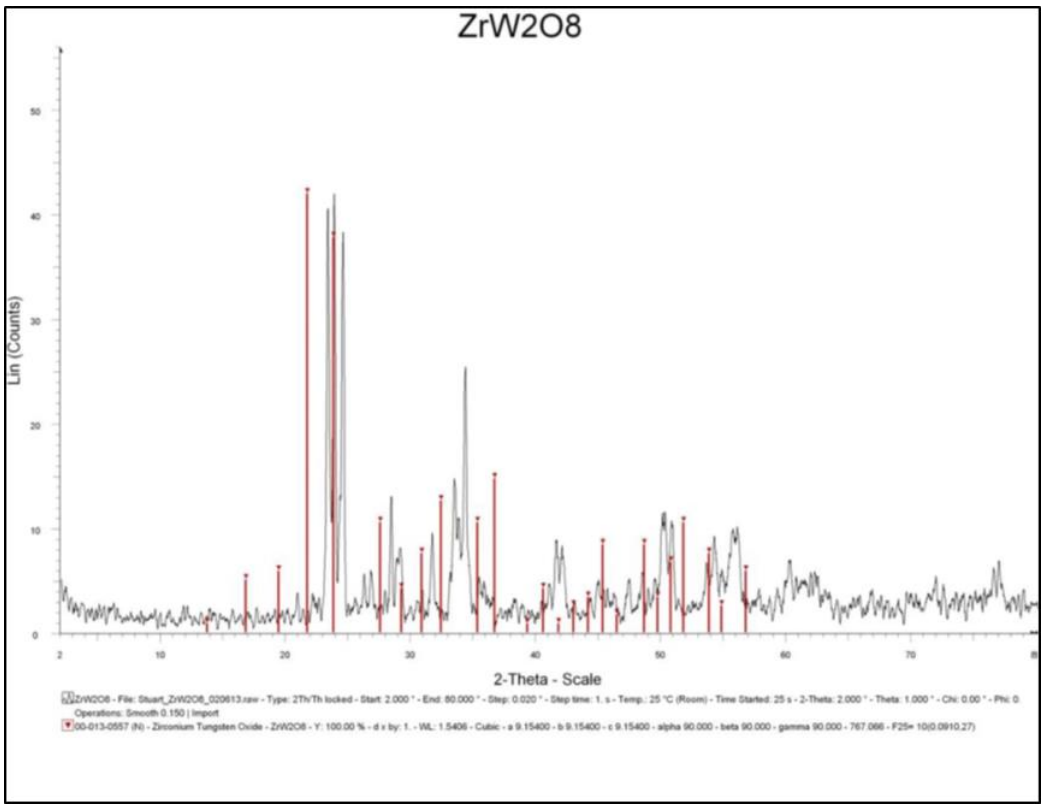

Figure 1.17: XRD pattern of synthesized powder with cubic ZrW_2O_8 pattern overlay

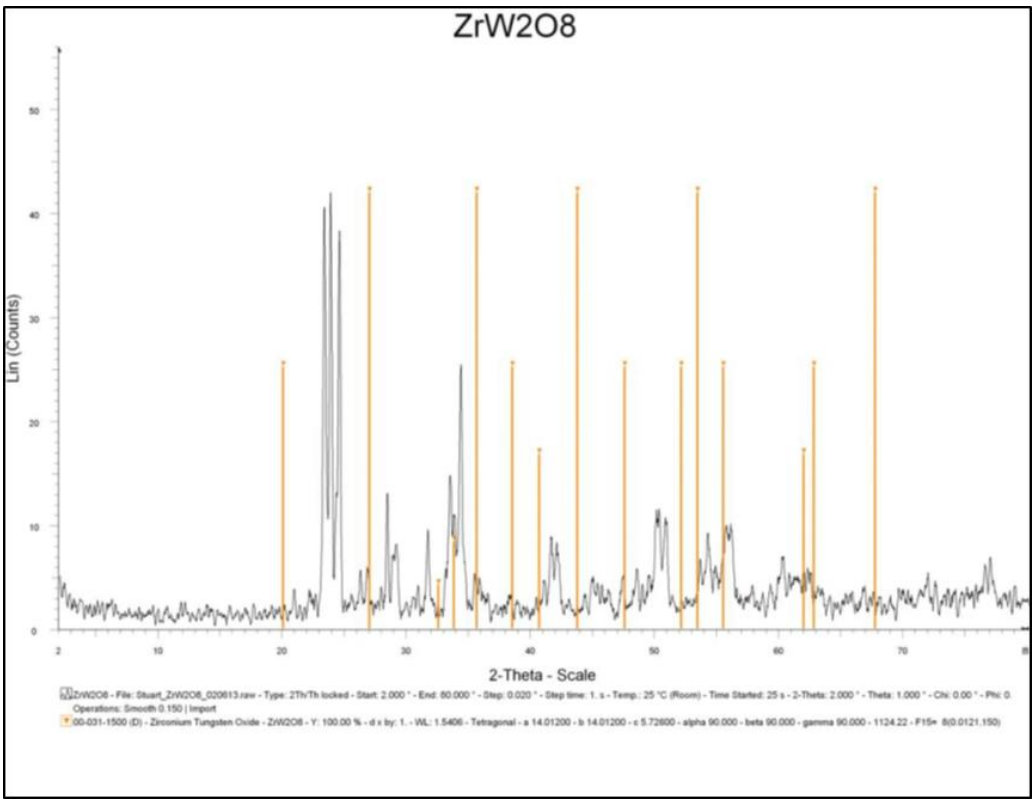

Figure 1.18: XRD pattern of synthesized powder with tetragonal ZrW_2O_8 pattern overlaying

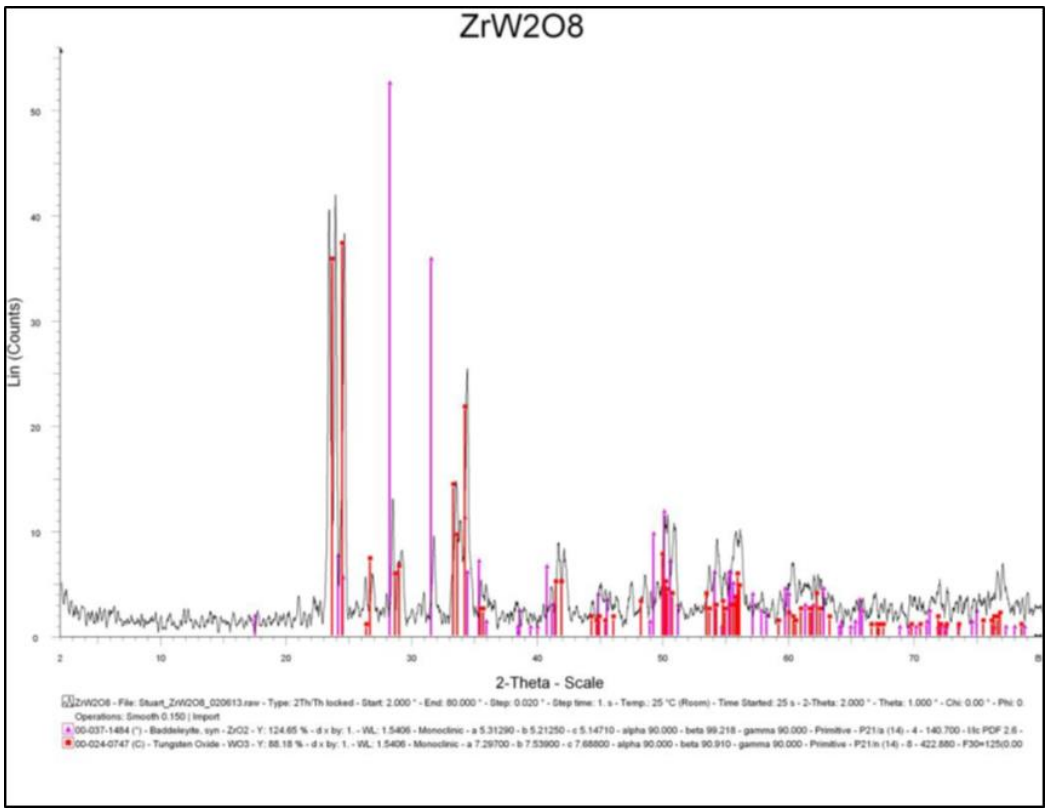

Figure 1.19: XRD pattern of synthesized powder with ZrO_2 and WO_3 patterns overlaying

3. Cobalt Ferrite

After several failures trying to find a negative Poisson's ratio for zirconium tungstate, additional research found a new ceramic material that potentially had auxetic properties. Valant et al. [9] claimed that they found pulse-laser deposited $CoFe_2O_4$ had a negative Poisson's ratio. This was due to hexagonal shapes formed by the bonds that caused the material to behave auxetically, at least in one direction. So, in pursuit of this new compound, several different structures were modeled in MS6, some based on the data in Valant et al.'s [9] article and some based on other data from different sources.

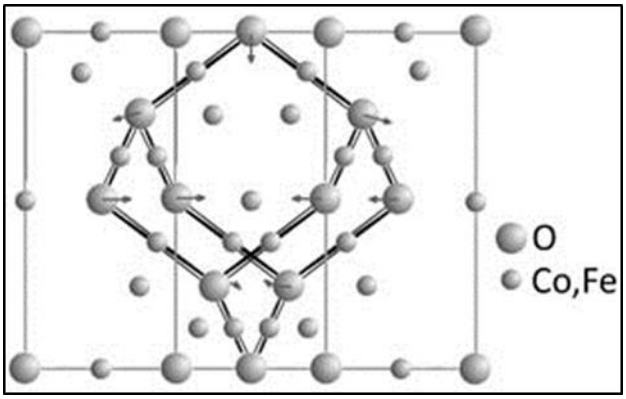

Figure 1.20: Diagram of CoFe2O4 from Valant et al. [9]

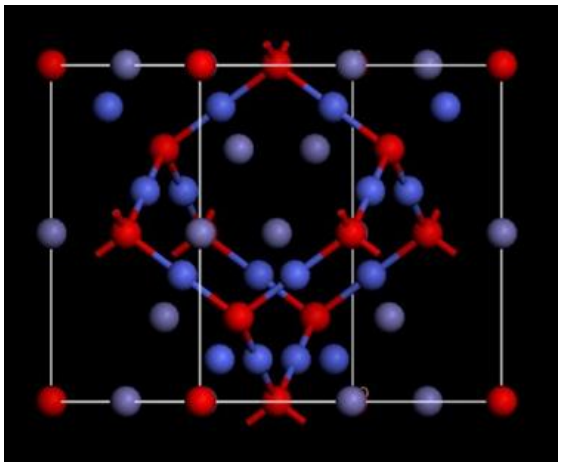

Figure 1.21: MS6 model of $CoFe_2O_4$ attempting to match the figure given in Figure 1.20

From Article: To get the actual model used in MS6, the coordinates for the atoms were determined from the diagram given in the article. Figure 1.20 shows the diagram given in the paper and Figure 1.21 shows the model derived from that diagram. The two structures are very similar with the red atoms being oxygen, the blue atoms being cobalt, and the purple atoms being iron. Unfortunately, MS6 was unable to find elastic constants for this system. Although, it should be mentioned that the diagram given in Valant et al.'s paper [9] can't possibly be the whole one. The chemical formula of the cell is supposed to be $CoFe_2O_4$, but there are clearly more metal atoms than oxygen atoms. It's possible that the hexagonal

structure is responsible for cobalt ferrite's auxetic behavior, but that isn't the correct diagram displaying it.

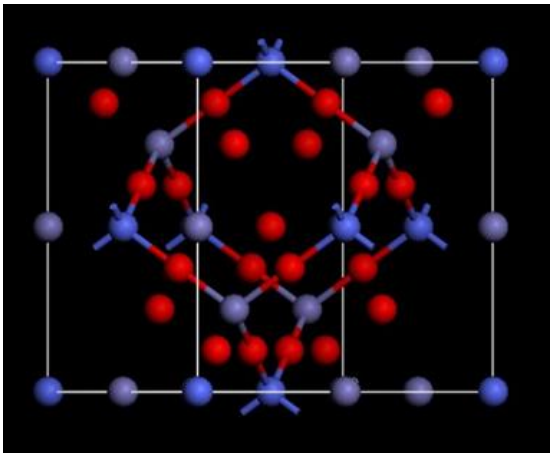

Figure 1.22: MS6 model of $CoFe_2O_4$ that tries to match the structure of Valant et al's article [9] but switches atoms to a more sensible configuration; this is used as the Art.-Swap structure

Art.-Swap: After failing to achieve a negative Poisson's ratio with the model derived from the article, some changes were made to the unit cell, much like in the zirconium tungstate section, to get auxetic behavior. First, many of the atoms were swapped around to try a match a more intuitive idea of the system should resemble. For example, the blue atoms representing cobalt were swapped with the red oxygen atoms. Figure 1.22 shows the full extent of the changes. This fixed the ratios of the atoms in the cell a little bit. However, this too failed to converge and MS6 could not determine its elastic constants.

Art.-Sym. Swap: The final change made to the original design was to force Fd-3m symmetry on the cell. Figure 1.23 shows the same hexagonal design if it were cut in half and repeated that way. This was made under the assumption that, hopefully, the calculation would be easier to make and the system would be able to converge. Unfortunately, this model failed as well.

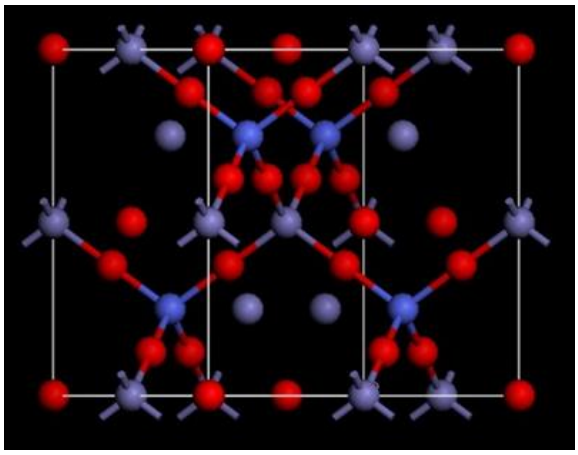

Figure 1.23: MS6 model of $CoFe_2O_4$ with Fd-3m symmetry; this is used as the Art.-Sym. Swap structure

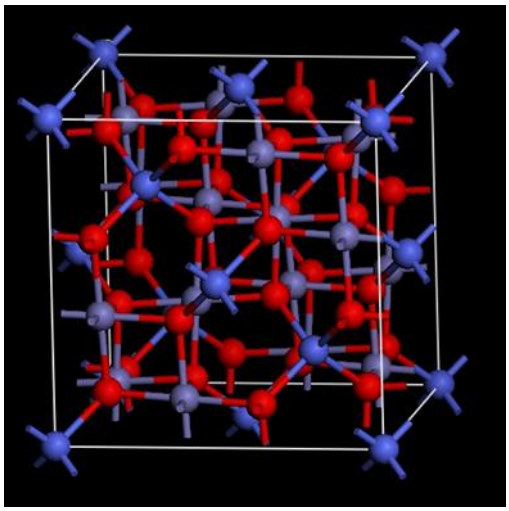

Figure 1.24: MS6 model of $CoFe_2O_4$ as a spinel structure; this is used as the Reg. Spinel structure

Reg. Spinel: After several more failures with Valant et al.'s model [9], it was determined that a different model needed to be devised. So cobalt ferrite was modeled as an average spinel. (Figure 1.24) The stoichiometry in this version actually worked out to match the chemical formula and it fit with structures mentioned in other literature sources [10, 11]. Finally, MS6 was able to find the elastic constants for this material. Unfortunately, the Poisson's ratio was not negative.

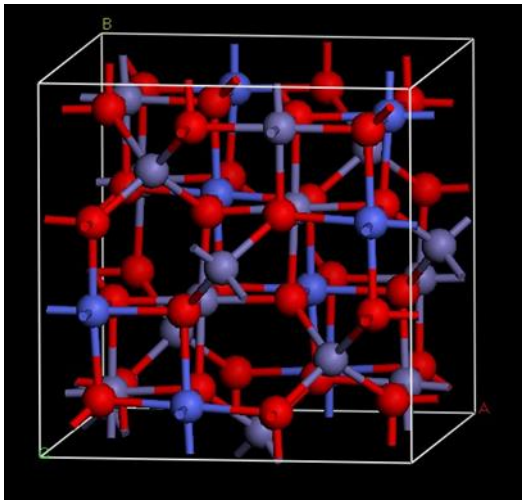

Figure 1.25: MS6 model of $CoFe_2O_4$ as an inverse spinel; this is used as the Inv. Spinel structure

Inv. Spinel: Additional research into cobalt ferrite revealed that it is, in fact, a completely inverse spinel. Swapping the cobalt atoms in tetrahedral positions with the iron atoms in octahedral positions gave the proper structure for cobalt ferrite. (Figure 1.25) This resulted in the lowest Poisson's ratio yet. While not negative, it may still lead to auxetic behavior under certain unknown conditions.

Like the zirconium tungstate, one of the proposed ideas to make the simulated compounds auxetic was to substitute smaller cations into the lattice in place of the metals. Titanium, vanadium and sodium ions were placed in octahedral and tetrahedral locations in the $CoFe_2O_4$ model. Unfortunately, all of the tests for $CoFe_2O_4$ failed even though they were done on the inverse spinel model that resulted in low Poisson's ratios.

Table 1.2: Summary of Poisson Ratios for Cobalt Ferrite Models

	XY	YX	ZX	XZ	YZ	ZY
$CoFe_2O_4$						
From Article	n/a	n/a	n/a	n/a	n/a	n/a
Art.-Swap	n/a	n/a	n/a	n/a	n/a	n/a
Art.-Sym. Swap	n/a	n/a	n/a	n/a	n/a	n/a

Reg. Spinel	0.2730	0.2730	0.2730	0.2730	0.2730	0.2730
Inv. Spinel	0.1249	0.1252	0.1487	0.1499	0.1229	0.1216

4. Lanthanum Niobate

4.1 $LaNbO_4$ Model

Continued research into auxetic ceramic materials revealed that the monoclinic form of lanthanum niobate ($LaNbO_4$) may have negative Poisson ratios, at least anisotropically. Rovati [12] reported on a number of monoclinic crystalline solids that, theoretically, have auxetic properties. One of the most auxetic ones was $LaNbO_4$ with a Poisson's ratio of -3.01. Using MS6 and data gathered from Tsunekawa [13], the unit cell displayed in Figure 1.26 was made easily. The atoms were added with position data from Huse et al [14]. The green tetrahedrons are NbO_4 and the single blue atoms are lanthanum. Some data on the actual structure of lanthanum niobate is given in Table 1.3 and Table 1.4.

Table 1.3: Crystal Data for m-$LaNbO_4$

	Tsunekawa [13]
a(Å)	5.2015(1)
b(Å)	11.5194(2)
c(Å)	5.5647(1)
α(°)	90
β(°)	94.100(1)
γ(°)	90

Table 1.4: Atomic Position Data for m-$LaNbO_4$

Atom	X	Y	Z
Lanthanum	0.7500	0.1230(2)	0.5000
Niobium	0.2500	0.1037(2)	0.0000
Oxygen (1)	0.4876(5)	0.2043(2)	0.1464(4)
Oxygen (2)	0.0544(4)	0.0337(2)	0.2383(4)

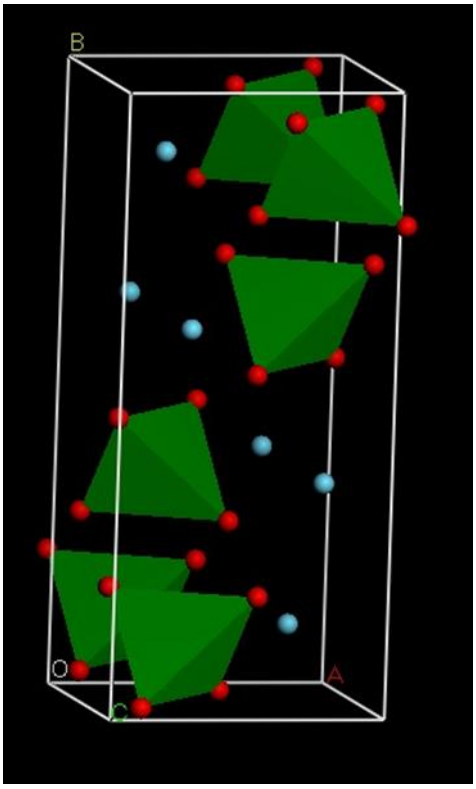

Figure 1.26: MS6 model of $LaNbO_4$ in polyhedral form generated with data from [13]; the green tetrahedrons are NbO_4; this is used as the structure in Monoclinic Cell and Anisotropic conditions

Monoclinic Cell - Using data gathered from Tsunekawa [13], the unit cell displayed in Figure 1.26 was quickly made. The atoms were added with position data from Huse et al. [14] The green tetrahedrons are NbO_4 and the single blue atoms are La. This simulation was performed under the constraint that the cell is monoclinic (I2/A) and isotropic. Perhaps this is one of the contributing factors to the positive Poisson's ratios MS6 determined (given in Table 1.5).

Anisotropic – Shifting the symmetry from monoclinic to triclinic (P1 cell) made significant improvement in the Poisson's ratio. It gives the closest-to-negative ratios yet. This agrees with the assumption that if auxetic properties exist in any the simulated compounds, it

will likely be in their P1 form. No physical changes were made to the cell, so it is exactly the same as in Figure 1.26.

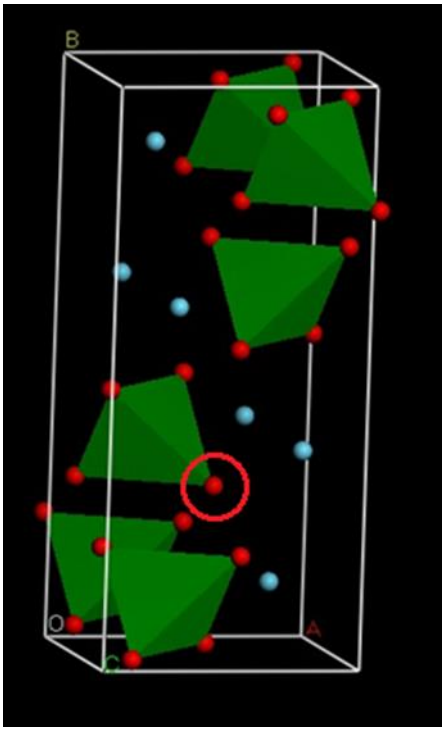

Figure 1.27: MS6 model of $LaNbO_4$ with oxygen atom circled for deletion; used as the structure for the Oxygen Vacancy condition

Oxygen Vacancy – Like the other compounds an oxygen vacancy was simulated to if it any effect on the Poisson's ratio. The deleted oxygen here is located at (X = 0.4876, Y = 0.2957, Z = 0.6464). It is also shown circled in red in Figure 1.27. The result was the best to date at that time.

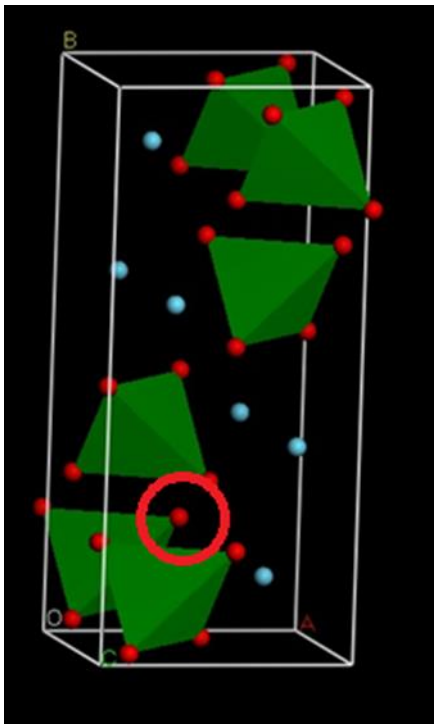

Figure 1.28: MS6 model of $LaNbO_4$ with oxygen circled for deletion; this is used as the structure for the Oxygen Vacancy II condition

Oxygen Vacancy II – This model is just like the previous one, however, a different oxygen atom is deleted from the system. (X = 0.4876, Y = 0.2043, Z = 0.1464) [Figure 1.28] After several months of searching this is the material that finally produced a negative Poisson's ratio. When looking at the Poisson's Ratio data in Table 1.5, it is important to remember that these are anisotropic values. They don't follow the standard $-1 < \nu < 0.5$ that most bulk materials display. This is also why only two of the numbers are negative rather than all six.

Once it was discovered that lanthanum niobate with oxygen vacancies had negative Poisson's ratios many tests similar to those performed on ZrW_2O_8 in earlier months were again used here. There were several instances of Materials Studio being unable to converge on

an answer, but in every case where it completed a model it result in at least a couple ratios having negative values.

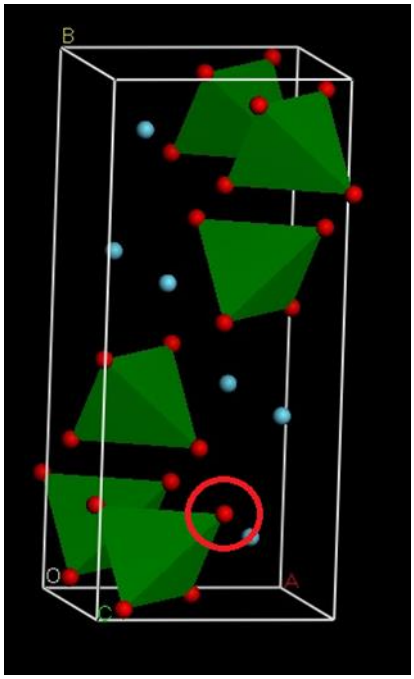

Figure 1.29: MS6 model of $LaNbO_4$ with oxygen circled for deletion

The newest set of simulations involves testing more than one cell at the same time. For example, two $LaNbO_4$ cells are merged into one supercell and the simulation is run as such. The particular cell was replicated in the A-direction, that is to say the supercell is 2A units long, 1B units tall, and 1 C units deep (The directions can be spotted in Figure 1.29 above). Additional tests were performed on 2B- and 2C-cells. A similar process was carried out on a four-cell model (2A/1B/2C) and an eight-cell model (2A/2B/2C). Note that all of these supercells are made of the cells containing the oxygen vacancy. All of the two-cell and four-cell models converged and produced negative ratios but several tries with the eight-cell model have all failed. The data for these tests are given in Table 1.5.

Table 1.5: Summary of Poisson's Ratios for Lanthanum Niobate

	XY	YX	ZX	XZ	YZ	ZY
Monoclinic	0.1533	0.1220	0.3100	0.4497	0.3069	0.2659
Anisotropic	0.1241	0.0903	0.3202	0.4777	0.3397	0.3129
O-Vacancy I	0.0650	0.0727	0.3127	0.3679	0.4732	0.3597
O-Vacancy II	-0.3347	-0.5243	0.6894	0.4999	0.6282	0.5531
LaNbO4_O-Vac_01	-0.3347	-0.5243	0.6894	0.4999	0.6282	0.5531
LaNbO4_O-Vac_02	-0.2141	-0.3188	0.6048	0.4664	0.5534	0.4819
LaNbO4_O-Vac_03	-0.1363	-0.2114	0.4538	0.3820	0.5463	0.4184
LaNbO4_O-Vac_NoGeOpt	1.5498	1.4785	-0.0353	-0.0128	-0.2647	-0.7647
LaNbO4_O-Vac_2A	-2.6136	-1.4460	-0.1274	-0.6858	3.4226	1.1489
LaNbO4_O-Vac_2B	-0.3643	-0.6916	1.1141	0.3741	0.4442	0.6967
LaNbO4_O-Vac_2C	-0.2335	-0.1713	0.1374	0.0940	-0.1562	-0.3112
LaNbO4_O-Vac_2A/2C	0.2654	1.0567	-0.8137	-0.5743	1.0391	0.3697

4.2: Synthesis

Since there is evidence that lanthanum niobate may actually have auxetic properties, the next step would be the synthesis of that material. There are several possible routes to choose from, many more than what is listed here.

1. Ball milling – Takagi et al. [15] – Equal atomic amounts of La_2O_3 and Nb_2O_5 powders are mixed by the conventional ball-milling method with ethyl alcohol and small ZrO_2 balls in a plastic pot for 24 hours. The mixture is then completely dried with a rotary evaporator at 60^{o}C for 2 hrs in vacuum and then dry ball-milled for 24 hrs. Finally, the dried powder is calcined at 1000^{o}C for 2 hrs.
2. Chemical synthsis – Jian and Wayman [16] – React citric acid ($C_6H_8O_7$) with niobium pentachloride ($NbCl_5$) and lanthanum chloride ($NbCl_3$) in isopropyl alcohol. Dry the

solution in an oven at 80^{o}C. The complex that forms is then calcined at 800^{o}C. The resulting powder is ball-milled for 48 hrs to get a very fine powder.

3. Spray pyrolysis – Mokkelbost et al. [17] – Pure lanthanum niobate powder was synthesized by spray pyrolysis using standardized aqueous solutions of a 0.2M La-EDTA complex and 0.16M Nb-malic acid complex. The solutions were atomized directly into a rotating furnace at 840-850^{o}C. The outlet temperature of the furnace was 450-500^{o}C. The as-prepared powders were dry ball milled for 15 min, followed by calcination at 800-1200^{o}C for 6 h in air. The calcined powders were ball milled in ethanol for 3-24 h, dried in a rotavapor, ground, and sieved at 500 μm.

4.3: Lanthanum Niobate Confirmation

The synthesis method we chose used the experimental procedures in Jian and Wayman [16]. These called for mixing niobium pentachloride ($NbCl_5$) and lanthanum chloride hydrate ($LaCl_3$+$7H_2O$) along with citric acid in an excess of isopropyl alcohol. After drying and calcining at the recommended temperatures, a white powder (Figure 1.30) was formed.

Figure 1.30: Photograph of synthesized lanthanum niobate powder

To prove that this was, indeed $LaNbO_4$ and not an impure mixture of intermediate products and complexes, both XRD and EDS test were performed on the powder. First, the EDS test showed several peaks identified as lanthanum and niobium. The entire spectrum is shown in Figure 1.31. There was also a strong peak for oxygen that helps to confirm the powder as a ceramic, at least. One possible caveat for this test is that, under x-ray radiation, lanthanum and some lanthanum compounds are phosphorescent. The extra photons given off by this effect can cause peak broadening in the spectrum. This effect was minimized, hopefully, by focusing on a smaller area of powder, to reduce the number of photons emitted.

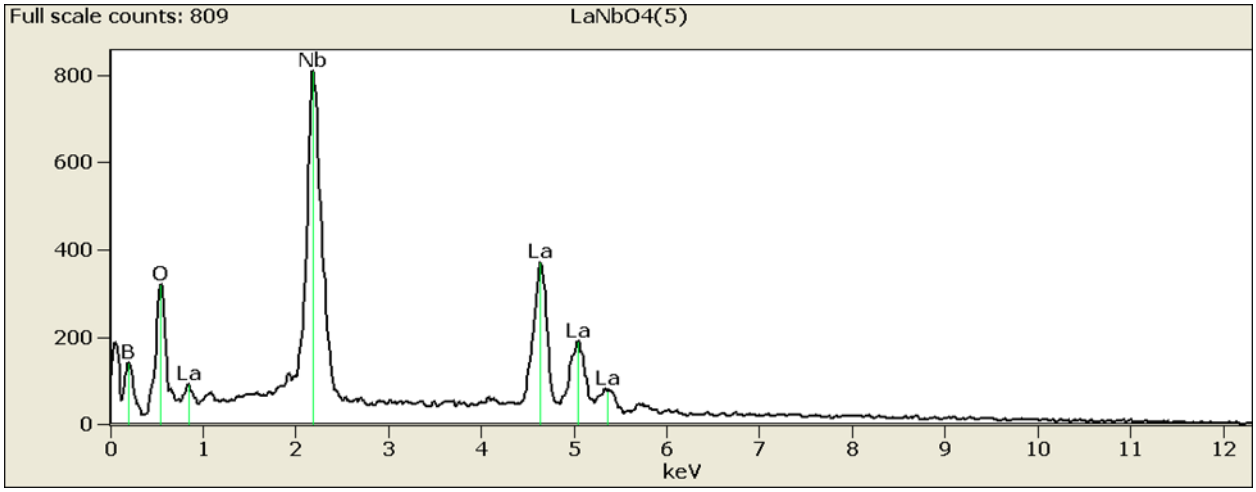

Figure 1.31: EDS spectrum of synthesized lanthanum niobate powder

The XRD was much more helpful in confirming the structure of the powder. Below, in Figure 1.32, two lanthanum niobate spectra are compared against the spectrum from the synthesized powder. The powder is the black peaks and the standards are the red and blue peaks. The peaks of the spectrum very nearly match those of the monoclinic $LaNbO_4$ standard spectra. The conclusion from these two tests strongly suggests that the synthesized powder is monoclinic lanthanum niobate.

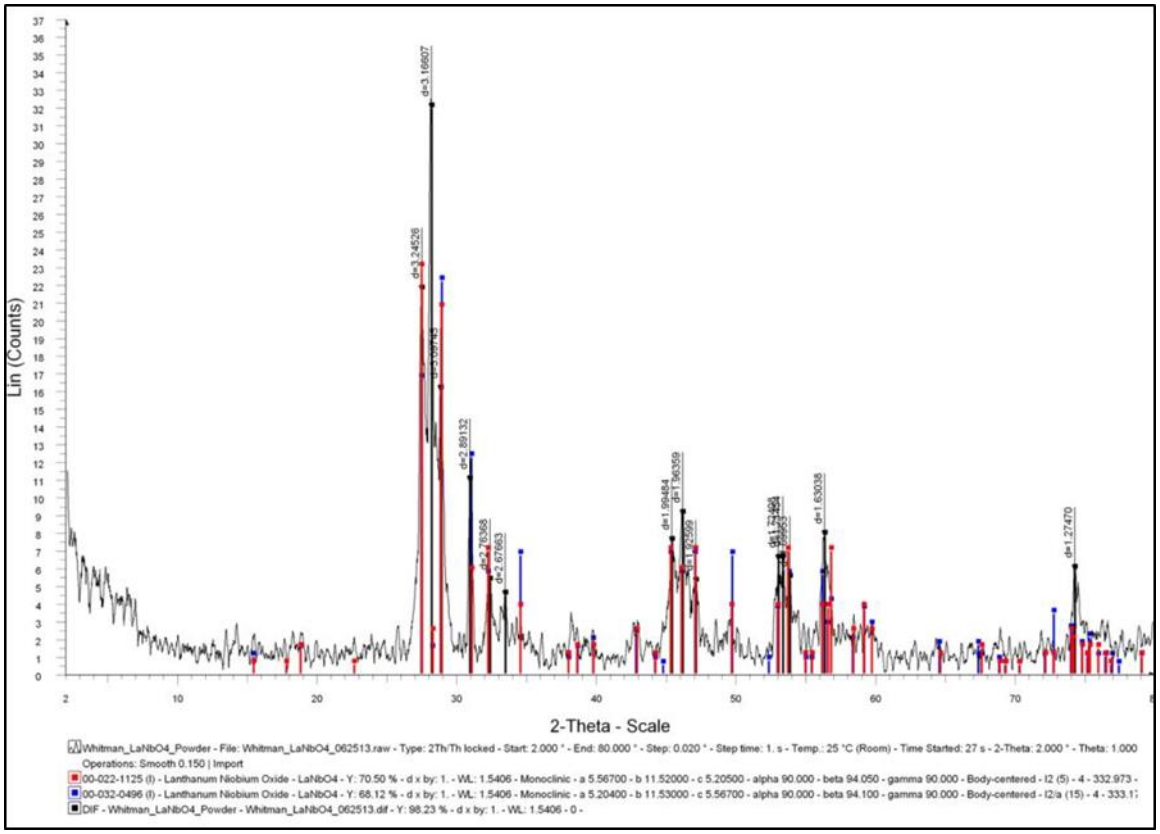

Figure 1.32: XRD spectrum of synthesized powder with $LaNbO_4$ spectra overlaid

4.4: Auxetic Property Testing

Since the synthesis of lanthanum niobate powder, we've been waiting to perform the next step which is the sintering and testing of a pellet of the material. Unfortunately, we have had no luck during the pressing process. In each case, we have been unable to create a single cohesive pellet that is longer than 1 mm. Figure 1.33 shows the best example of a pellet we created using carboxymethyl cellulose as a binder and 2.5% of the compressed components. Even using 10 tons of pressure, which was more than twice our original guess for necessary pressure, the pellet cracks and disintegrates into small platelet-like pieces below the solid pellet structure.

Figure 1.33: Incomplete pellet of $LaNbO_4$ after pressing process

There is some good news on this front though. As we make additional changes, we have been getting closer and closer to a single cohesive pellet. Figure 1.33 shows the best result so far, but we might still be able to improve it. Once we have a proper pellet, we can test it with our lab's thermal analyzer and finally have an answer about the potential for $LaNbO_4$ to have auxetic properties.

5. Bismuth and Bismuth Oxide

5.1: Bismuth Models

Many pure metals, bismuth included, have slightly auxetic properties in at least one direction. Usually these properties are anisotropic, though. Among the many odd properties of pure bismuth, it also has a monoclinic structure at room temperature. Bismuth oxide (Bi_2O_3) was chosen for simulation with MS6 under the hypothesis that a monoclinic metal with auxetic properties will have a monoclinic oxide compound with auxetic properties. Bi_2O_3 does exist as a monoclinic phase at room temperature.

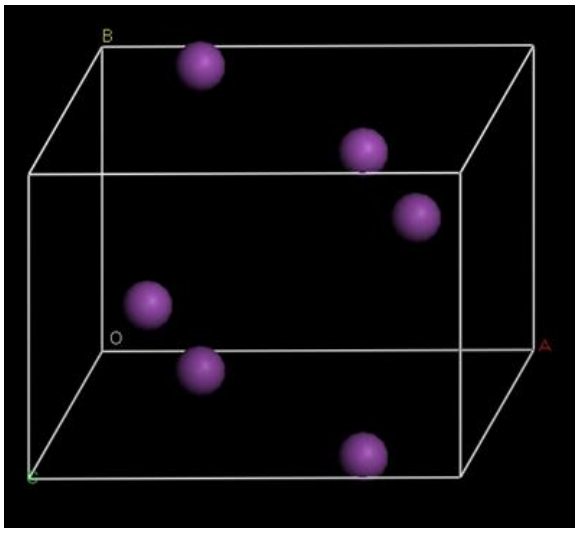

Figure 1.34: MS6 model of pure bismuth metal in its monoclinic form; this is used as the structure for Bi-metal

Bi-metal: The first test performed in this series was on the bismuth metal itself. Similar to the zirconium tungstate simulations, the basic structure was downloaded from the Crystallography Open Database. The monoclinic form (COD ID: 8100521) [18] shown in Figure 1.34 was the only one analyzed though several structures were available. The Poisson ratios determined by MS6 were negative in the YZ and ZY directions, showing slight auxeticity.

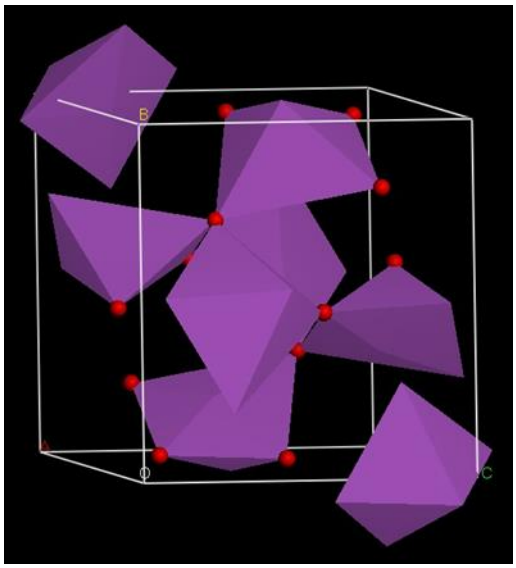

Figure 1.35: MS6 model of Bi_2O_3 in its monoclinic form; this is used as the Bi_2O_3 structure

Bi_2O_3: After confirming the anisotropic auxetic property of bismuth metal, bismuth trioxide was simulated. This, too, was downloaded from COD (ID: 9012546) [19]. The result is shown in Figure 1.35. Again, only the monoclinic structure was tested. Unfortunately, this compound did not demonstrate any negative Poisson's ratios.

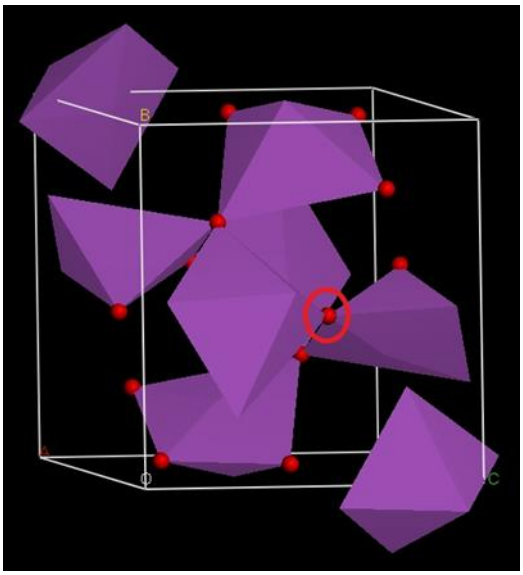

Figure 1.36: MS6 model of monoclinic Bi_2O_3 with an oxygen atom circled for deletion; this is used as the O-vacancy structure

O-vacancy: Just like the trials for zirconium tungstate and cobalt ferrite, an oxygen vacancy was added randomly (X: 0.2376; Y: 0.4455; Z: 0.6202 or the atom circled in red in Figure 1.36) to see if it somehow made the polyhedra more mobile. Just like all the other cases it did not change much and showed no auxetic properties.

After some review, we realized that we only simulated alpha-Bi_2O_3 as it is the standard form of Bi_2O_3 at room temperature and pressure. Eventually, other polymorphs of Bi_2O_3 were included in the investigation. The first model tested was the beta phase of Bi_2O_3. While this phase normally forms at temperatures above 300^oC, it might be useful in high-

temperature applications. After all that is the point of using ceramic auxetic materials instead of polymeric ones.

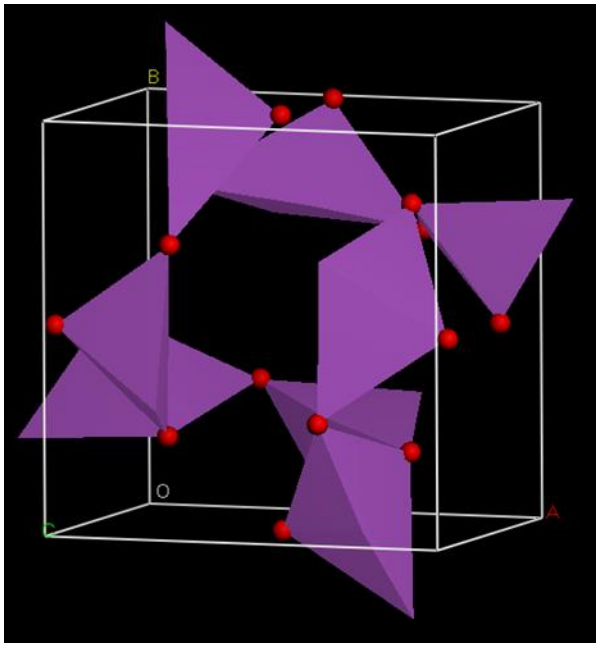

Figure 1.37: MS6 model of beta-Bi_2O_3 in polyhedral form

Using the data gathered from Blower and Greaves [20], the unit cell of beta-Bi_2O_3 was built and it is displayed in Figure 1.37. (If you're curious about the alpha phase, the data was gathered from [21]) Beta-Bi_2O_3 has a tetragonal structure and is a member of the space group P-42_1c. It has the lattice parameters: a = 7.741 Å, c = 5.634 Å. The unit cell consists of several bismuth-centered tetrahedrons which are connected at all vertices. In some orientations, there is a large square-shaped gap in the center of the cell. This, along with the rotating polyhedron theory, may contribute to its supposed auxetic behavior. This gap is shown in Figure 1.38. Data from different Poisson's ratio tests are given in Table 1.9 in no particular order with no particular focus on the structure. Now that we have another candidate to study, we are started additional modeling experiments similar to those we performed on the other compounds, i.e. oxygen vacancies. Also, we may start synthesizing this material as well.

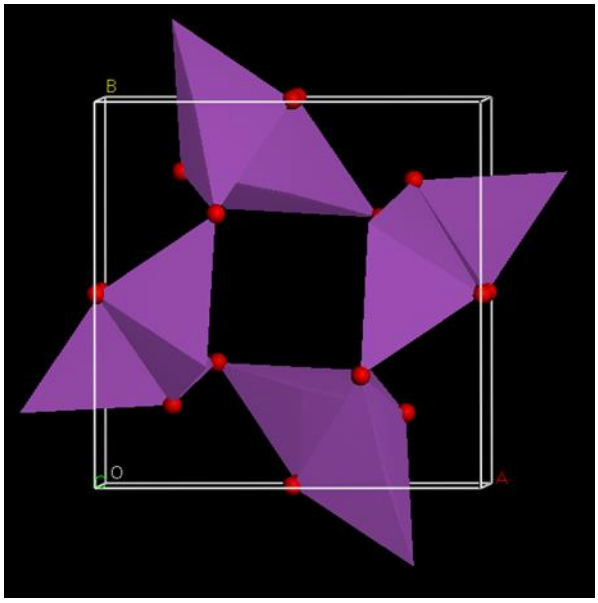

Figure 1.38: MS6 model of beta-Bi_2O_3 which has been oriented to emphasize the square tunnel shape made by the polyhedrons

Table 1.6: Summary of Poisson's Ratios for Bismuth and Bismuth Oxide

	XY	YX	ZX	XZ	YZ	ZY
Bi-metal	0.0936	0.0612	0.2690	1.0555	-0.1313	-0.0512
Bi_2O_3	0.4185	0.2941	0.3277	0.2888	0.1531	0.2472
O-vacancy	0.4009	0.3550	0.2452	0.2170	0.1821	0.2324
α-Bi_2O_3	0.3506	0.2742	0.2377	0.2439	0.2265	0.2822
β-Bi_2O_3-$P42_1c$	0.0412	0.0412	-0.0426	-0.0512	-0.0512	-0.0426
β-Bi_2O_3-P1	0.8157	-1.4845	2.2815	0.8228	-2.7680	4.2171

6. References

[1] Evans, K. E., and A. Alderson. "Auxetic Materials: Functional Materials and Structures from Lateral Thinking!" *Advanced Materials* 12.9 (2000): 617-628.

[2] Lakes, Roderic. "Foam Structures with a Negative Poisson's Ratio." *Science* 235.4792 (1987): 1038-1040. *JSTOR*. 16 Apr. 2014. <http://www.jstor.org/stable/10.2307/1698767?ref=search-gateway:0e74fc57bdf572d5eb83ea48c2f7610f>.

[3] Greaves, G. N., A. L. Greer, R. S. Lakes, and T. Rouxel. "Poisson's Ratio and Modern Materials." *Nature Materials* 10.11 (2011): 823-37.

[4] Grima, Joseph N., Ruben Gatt, Andrew Alderson, and Kenneth E. Evans. "On the Origin of Auxetic Behaviour in the Silicate Alpha-cristobalite." *Journal of Materials Chemistry* 15 (2005): 4003-4005.

[5] Tan, X., W. Jo, T. Granzow, J. Frederick, E. Aulbach, and J. Rödel. "Auxetic Behavior under Electrical Loads in an Induced Ferroelectric Phase." *Applied Physics Letters* 94.4 (2009): 042909.

[6] Miller, W., C. W. Smith, D. S. Mackenzie, and K. E. Evans. "Negative Thermal Expansion: A Review." *Journal of Materials Science* 44.20 (2009): 5441-451.

[7] "Crystallography Open Database." *CIF Information Card: 2002948*. N.p., n.d. 28 Feb. 2013. <http://www.crystallography.net/information_card.php?cif=2002948>.

[8] Noailles, L., B. Dunn, D. Larson, J. Starkovich, and H. Peng. "Preparation of ZrW2O8 Xerogel and Aerogels by Sol-gel Chemistry." *Key Engineering Materials* 264-268 (2004): 363-66.

[9] Valant, Matjaz, Anna-Karin Axelsson, Frederic Aguesse, and Neil M. Alford. "Molecular Auxetic Behavior of Epitaxial Co-Ferrite Spinel Thin Film." *Advanced Functional Materials* 20.4 (2010): 644-47. *Wiley Online Library*. John Wiley & Sons, Inc., 19 Jan. 2010. 28 Feb. 2013. <http://onlinelibrary.wiley.com/doi/10.1002/adfm.200901762/full>.

[10] "Spinel." *WolfWikis RSS*. North Carolina State University, 9 May 2007. 28 Feb. 2013. <http://wikis.lib.ncsu.edu/index.php/Spinel>.

[11] Prince, E. "Neutron Diffraction Observation of Heat Treatment in Cobalt Ferrite." *Physical Review* 102.3 (1956): 674-76. *Physical Review Online Archive*. American Physical Society. 28 Feb. 2013. <http://prola.aps.org/abstract/PR/v102/i3/p674_1>.

[12] Rovati, Marco. "Directions of Auxeticity for Monoclinic Crystals." *Scripta Materialia* 51.11 (2004): 1087-091. *ScienceDirect.com*. Elsevier. 30 Mar. 2013. <http://www.sciencedirect.com/science/article/pii/S1359646204004580>.

[13] Tsunekawa, S., T. Kamiyama, K. Sasaki, H. Asano, and T. Fukuda. "Precise Structure Analysis by Neutron Diffraction for RNbO4 and Distortion of NbO4 Tetrahedra." *Acta Crystallographica Section A* 49 (1993): 595-600. International Union of Crystallography. 30 Mar. 2013. <http://scripts.iucr.org/cgi-bin/paper?S0108767392013035>.

[14] Huse, M., A. W.B. Skilbred, M. Karlsson, S. G. Eriksson, T. Norby, R. Haugsrud, and C. S. Knee. "Neutron Diffraction Study of the Monoclinic to Tetragonal Structural Transition in LaNbO4 and Its Relation to Proton Mobility." *Journal of Solid State Chemistry* 187 (2012): 27-34. *ScienceDirect.com*. Elsevier. 30 Mar. 2013. <http://www.sciencedirect.com/science/article/pii/S0022459611006955#>.

[15] Takagi, T., Y. H. Choa, T. Sekino, and K. Niihara. "Fabrication and Mechanical Properties of LaNbO4 and LaNbO4/Al2O3 Composites." *Key Engineering Materials* 161-163 (1999): 181-184.

[16] Jian, L., and C. M. Wayman. "Compressive Behavior and Domain-related Shape Memory Effect in LaNbO4 Ceramics." *Materials Letters* 26.1-2 (1996): 1-7.

[17] Mokkelbost, T., Ø. Anderson, R. A. Strom, K. Wiik, T. Grande, and M. A. Einarsrud. "High-Temperature Proton-Conducting LaNbO4-Based Materials: Powder Synthesis by Spray Pyrolysis." *Journal of the American Ceramic Society* 90 (2007): 3395-400.

[18] "Crystallography Open Database." *CIF Information Card: 8100521N*.p., n.d. 28 Feb. 2013. <http://www.crystallography.net/information_card.php?cif=8100521>.

[19] "Crystallography Open Database." *CIF Information Card: 9012546* N.p., n.d. 28 Feb. 2013. <http://www.crystallography.net/information_card.php?cif=9012546>.

[20] Blower, S.K., Greaves, C. "The Structure of β-Bi_2O_3 from Powder Neutron Diffraction Data." *Acta Cryst.* C44 (1988): 587-589. <http://journals.iucr.org/c/issues/1988/04/00/bw0485/bw0485.pdf>.

[21] Malmros, Gunnar. "The Crystal Structure of α-Bi_2O_3." *Acta Chem. Scand.* 24 (1970): 384-396. < http://actachemscand.org/doi/10.3891/acta.chem.scand.24-0384>.

CHAPTER 2

Electrochemical Storage in Zr-W Mixed Oxide Nanostructured Arrays

S. R. Whitman[a], K. S. Raja[a]

[a] Department of Chemical and Materials Engineering, University of Idaho, Moscow, Idaho 83843, USA

This article will be published in the 58th volume of the ECS Transactions journal, which covers the events of the Electrochemical Society's 224th meeting in San Francisco, 2013.

Abstract

ZrO_2-WO_3 mixed-oxide nanostructures are created by anodizing a Zr-20 wt% W metal alloy at different potentials followed by annealing at various temperatures. The nanostructures are analyzed via SEM/TEM, X-ray diffraction, and XPS. Phases of h-WO_3 and t-ZrW_2O_8 are found in both the as-anodized form and the annealed form. Also several electrochemical tests including cyclic voltammetry, EIS, and Mott-Schottky analysis are performed in electrolytes of different pHs. The maximum capacitance was determined to be ~45 mF/cm^2. The defect concentration in the material was calculated by using the slopes of the Mott-Schottky curves. Finally, the mixed-oxide nanostructures were tested in a two-electrode apparatus which cycled the potential of the system between 0 V and 1 V. The charge and discharge times of the tests increased as cycling continued but the rate of increment changed with pH, annealing temperature, and, to a lesser degree, nanostructure.

1. Introduction

Transition metal-oxide nanotube arrays find application in many types of devices including those used for energy conversion and energy storage. Also, the combination of two oxide nano-structures, such as NiO+TiO_2 and TiO_2+V_2O_5, show better electrochemical energy

storage [1,2,3]. This is because the faster charge/discharge kinetics lead to higher power density.

Normally the preparation of these two-oxide combinations is a two-step process, but mixed-oxide nanotubes have been synthesized in a single step by the anodization of binary alloys [4]. Often, these 'alloy' oxide nanotubes result in interesting electronic and electrochemical behavior [1,2,3,5]. Part of this is due to an inherent doping effect that occurs when transition metal ions substitute into each other's lattices and the forces of charge neutrality cause them to gain or lose electrons. Mixed-oxide nanotubes can also show enhanced properties. In this experiment, Zr-W mixed-oxide materials are investigated and ZrO_2-WO_3 based materials are considered strong and efficient solid-acid catalysts [5]. Also, there is the potential for the formation of a zirconium tungstate, ZrW_2O_8, phase to form. This phase may exhibit negative thermal expansion [6] based on a rotating polyhedra mechanism which, in turn, may enhance the storage capacity and stability of the material.

Combining an oxide with high ionic resistance with an oxide that has a high dielectric constant (such as ZrO_2 and Al_2O_3) has been found to result in high capacitance for electronic application [7]. This idea, which is normally applied to solid-state capacitors, has been extended to electrochemical capacitors in this experiment.

2. Experimental

2.1: Mixed-Oxide Preparation

A flat plate of 2-mm thick, Zr-20 wt% W metal alloy was cut into 1 x 1.5 cm coupons. Approximately 1 cm^2 of the coupon was exposed to 200 mL of an ethylene glycol electrolyte containing 3.8 vol% water and 0.25 M NH_4F. The metal alloy was connected to the positive terminal of a controlled DC power, while a 7.5 cm^2 titanium flag was connected to the

negative terminal. A constant potential of either 40 V or 60 V was applied to the system to anodize the metal alloy.

After anodization, several of the newly-formed oxides were annealed in a tube furnace with a constantly flowing, commercial-purity nitrogen stream. The furnace temperature was controlled at a rate of 5^{o}C/min up to the target temperature, at which point, it was held constant for two hours. The different target temperatures were: 350^{o}C, 450^{o}C, 550^{o}C, and 650^{o}C.

2.2: Surface Morphology

The samples' surface morphology was characterized using electron microscopy (FESEM: LEO SUPRA 35VP, TEM: JEOL 2010). Structural characterization of the nanoporous anodic oxide layer was performed by grazing-angle XRD on a PANalytical X'Pert Pro MRD diffractometer equipped with a Copper x-ray tube and parallel-beam optics. The incident angle was fixed at 0.9°. X-ray photo electron spectroscopy (PHI Quantum 2000) was employed to evaluate the surface valence states and electron density of states at the surface of the samples. Mono-chromated Al-Kα (1488.6 eV) radiation was used as the source with an acceptance angle of ±23° and take-off angle of 45°. Charge correction was carried out by considering the C 1s peak at 284.8 eV.

2.3: Electrochemical Characterization

Several electrochemical characterization tests were run on the mixed-oxide samples using a three-electrode apparatus. The mixed-oxide was the working electrode. A platinum flag was used as the counter electrode. A Ag/AgCl electrode filled with saturated KCl ($V_{SHE} \approx$ 0.23 V) was used as the reference electrode. Every set of tests was run in either 1M H_2SO_4 or

1M LiCl. First, cyclic voltammetry tests were performed for a potential range that changed with the pH of the electrolyte. For the sulfuric acid, the range was -0.5 to +0.9 $V_{Ag/AgCl}$. For the lithium chloride, the range was -0.8 to +0.6 $V_{Ag/AgCl}$. Also, three different scan rates of 10 mV/s, 100 mV/s, and 1000 mV/s were used to measure the process. The next characterization method was electrochemical impedance spectroscopy. Using a constant potential of 0.2 V, EIS measurements were taken over a range of frequencies from 100000 Hz to 0.01 Hz. From the resulting Bode plot, a frequency was chosen to perform a Mott-Schottky analysis. The potential range for this test was the same as that for the cyclic voltammetry, which was different for each electrolyte. Also, as part of the test procedure, it made 50 mV steps every two seconds.

After the characterization tests, a two-electrode apparatus, using two similarly-prepared mixed-oxide samples as the electrodes, was used to simulate the material in a real electrochemical capacitor. The system was charged with a constant current up to 1 V, then the current was reversed and it was discharged until the potential reached 0 V. This was repeated for 100 cycles.

3. Results and Discussion

3.1: Oxide Structure and Composition

From the SEM and TEM micrographs, two distinct nanostructures were discovered for the two different anodization potentials. Figures 2.1(a) shows a nanotube array for those sample anodized at 40 V. Figure 2.1(b) shows a nanoporous structure for the samples anodized at 60 V.

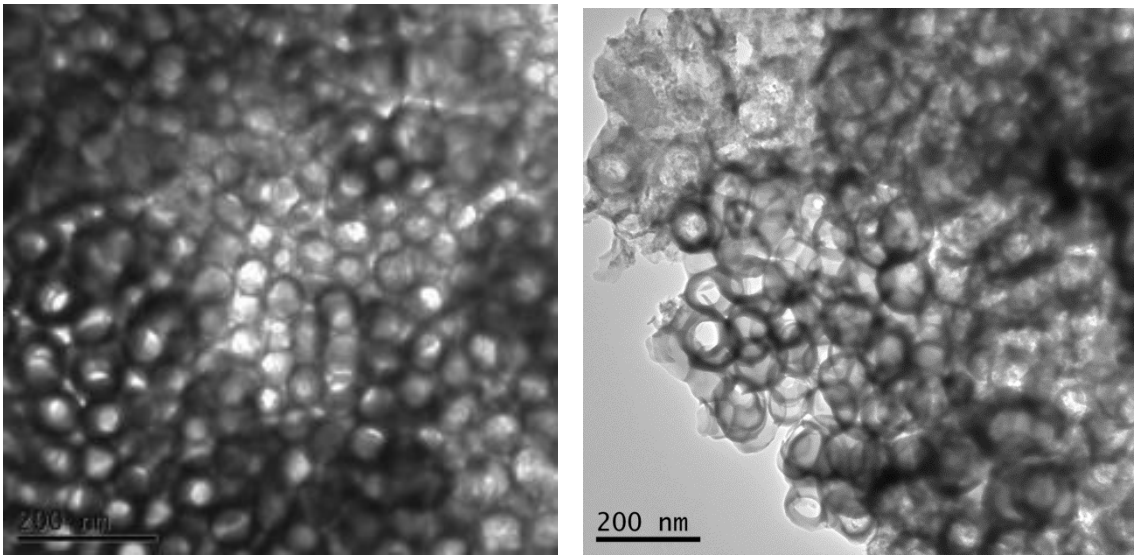

Figure 2.1: TEM images of ZrO_2-WO_3 mixed oxide nanostructure. (a) the samples anodized at 40V created nanotubes, (b) the samples anodized at 60V created nanopores.

The data from the glancing-angle XRD analysis (Figure 2.2) provides some insight on the phase changes of the material during annealing. By integrating the intensities of the major peaks of the graph, a rough estimate of the volume fraction of the phases in the material was made. It becomes clear that there is a reduction in the hexagonal WO_3 after annealing. There are also significant increases in the orthorhombic ZrO_2 and tetragonal ZrW_2O_8 phases. The relevance of the decrease in WO_3 will be noted later when the CV data is discussed, but it is important to mention the tunnel-like structure that forms when h-WO_3 is present [8]. It allows for greater intercalation of ions into the material and potentially increases the capacitance.

Figures 2.3(a)-(d) contain the results of the X-ray Photoelectron Spectroscopy analysis. In all the graphs there is a clear decrease in the binding energy after annealing. This is most likely due to an increase in the covalency of the bonding in the system that can be attributed to the increase in ZrW_2O_8 phase in the annealed state. Barr [9] proposed that when a complex mixed oxide forms by the mixing of two oxides, the cation of the predominantly

ionic oxide becomes even more ionic and the cation of the covalent oxide should experience an increase in its covalency. In the mixed oxide of ZrW_2O_8, Zr is the more ionic cation and W has a predominantly covalent character. The shift in the binding energy of W $4d_{5/2}$ after annealing could be associated with the conversion of some of the h-WO_3 phase into ZrW_2O_8 phase as observed from the XRD result.

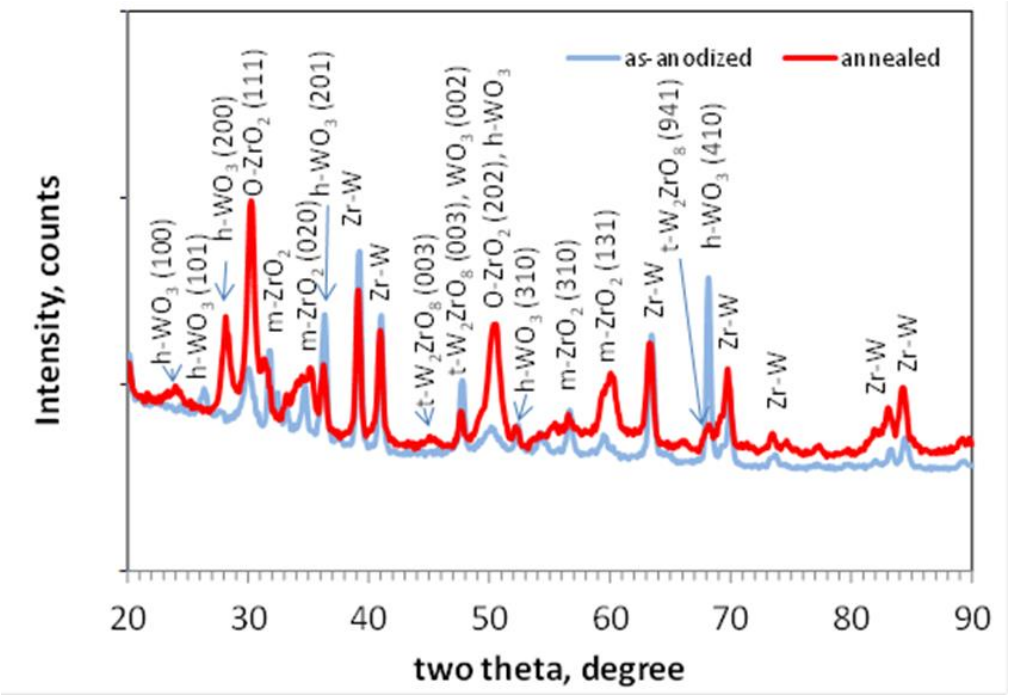

Figure 2.2: XRD spectrum of ZrO_2-WO_3 mixed oxide in a sample only anodized at 40V and a sample anodized at 450^oC.

The positive shift in the binding energy of the Zr-3d spectra of the annealed sample, shown in Fig 2.3(b), also supports the formation of a mixed oxide. The spin-orbit splitting of W-4f of the as-anodized sample (Fig. 2.3(c)) occurred at 36.2 and 38.2 eV as W-$4f_{7/2}$ and W-$4f_{5/2}$ peaks respectively. This corresponds to a W^{6+} oxidation state [10]. A shoulder was observed at the low energy end of the W-$4f_{7/2}$ spectrum of the as-anodized sample which

could be attributed to the presence of a lower valence state of the W cations, such as W^{5+} or W^{4+}. These lower valence cations are required for charge neutrality when a large concentration of oxygen vacancies form during the anodization. In Figure 2.3(d), the broad shoulder on the high-energy side of the O^{2-} peak in the as-anodized curve may be additional evidence of oxygen vacancies, chemisorbed oxygen, and/or hydroxyl ions [11, 12].

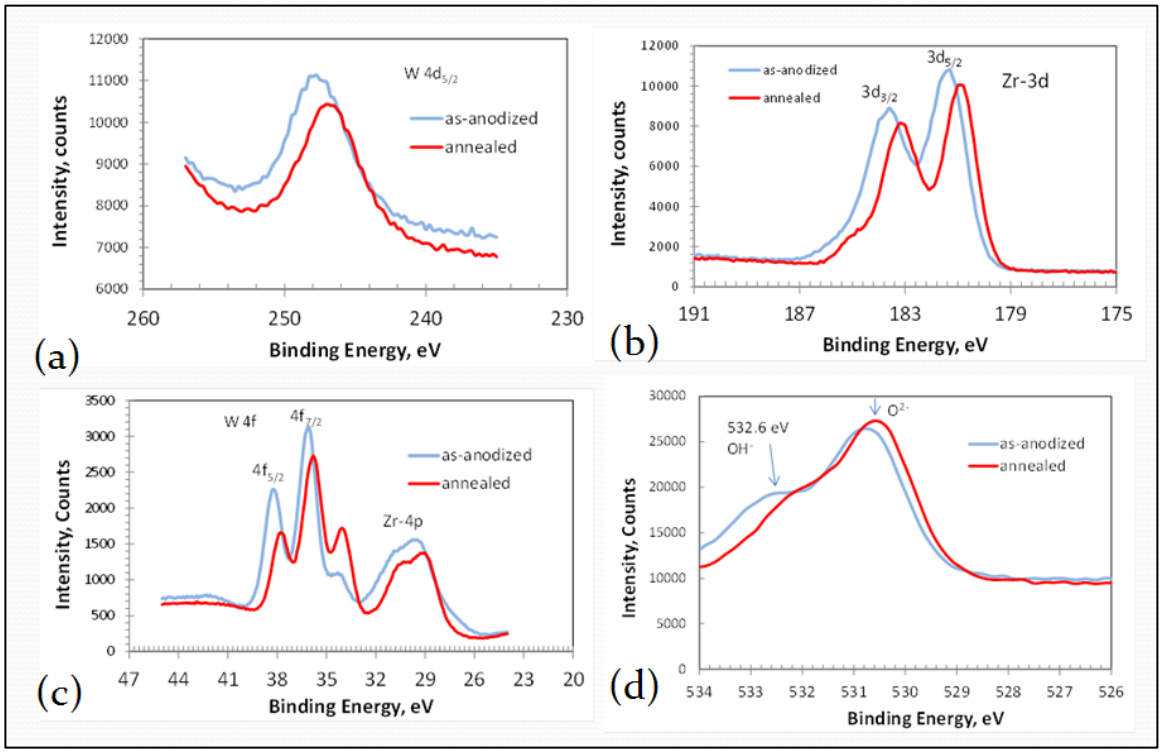

Figure 2.3: XPS spectra for ZrO_2-WO_3 mixed oxide in a sample only anodized at 40V and a sample anodized at 450^{o}C. (a) binding energy for W-4$d_{5/2}$, (b) binding energy for Zr-3d, (c) binding energy for W-4f and Zr-4p, (d) binding energy for oxygen in the structure

3.2: Electrochemical Characterization

Figure 2.4 is a cyclic voltammogram that is representative of several annealing conditions of mixed-oxide nanotubes (anodized at 40V) and tested with a scan rate of 100 mV/s in a 1M H_2SO_4 solution. The results displayed here are a fairly common trend noticed during the testing cycle.

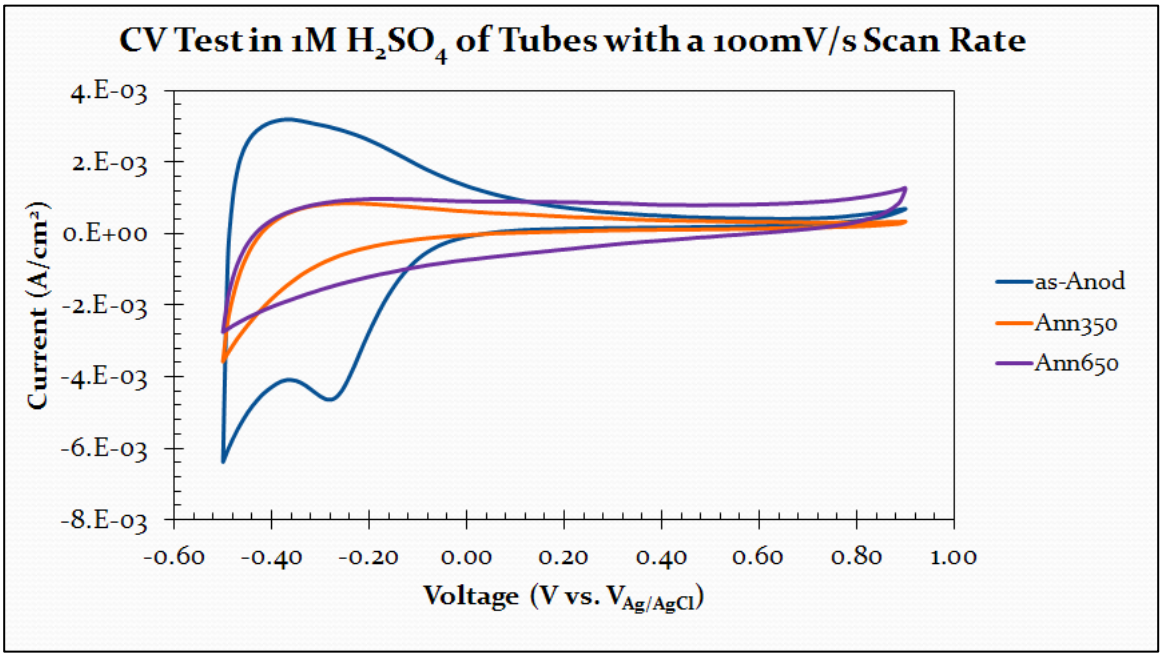

Figure 2.4: Cyclic voltammogram representative of the as-anodized condition, the annealed-at-350°C condition, and the annealed-at-650°C condition of mixed-oxide nanotubes (anodized at 40V) and tested with a scan rate of 100 mV/s in a 1M H_2SO_4 solution

The area inside the CV curve is directly related to the capacitance of the material, so the as-anodized form had the highest capacitance, the samples annealed at 650°C had the second highest with the samples annealed at 350°C having even less. The curves for the samples annealed at 450°C and 550°C were removed from the graph for clarity, but they generally fell between the 350°C and 650°C curves. The extreme increase in current density

for the as-anodized nanotubes can be attributed to reversible Faradaic tungsten reactions that occur according to the following reaction equations [13]:

$$2\ WO_3 + 2\ H^+ + 2e^- \leftrightarrow 2\ W_2O_5 + H_2O;\ E_o = -0.23\ V_{Ag/AgCl} \quad (1)$$

$$W_2O_5 + 2\ H^+ + 2e^- \leftrightarrow 2\ WO_2 + H_2O;\ E_o = -0.225\ V_{Ag/AgCl} \quad (2)$$

The reduction of h-WO_3 in the annealed form of the nanotubes, as mentioned in the XRD section, may be the reason that the presence of the reaction isn't as strong in the CV curves of the annealed samples. For those potentials above 0.0 $V_{Ag/AgCl}$, the main contributor to the capacitance is likely the electric double layer (EDL), as well as space layer charging due to charge defects in the material. It should be noted that the sample annealed at 650°C had a much higher capacitance in that regard.

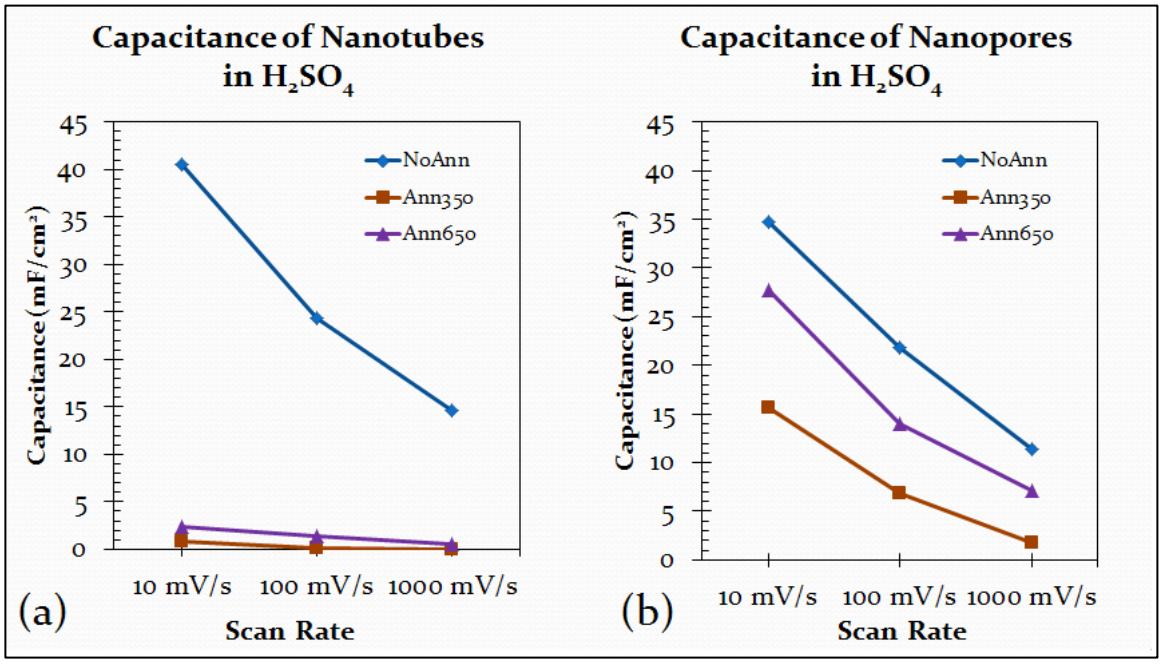

Figure 2.5: Capacitance values for mixed oxide samples in 1M H_2SO_4 with varying scan rates. (a) nanotube structure, (b) nanopore structure

From the CV curves, the capacitance value was calculated for each test. These values were ordered by scan rate and Figures 2.5(a) and 2.5(b) were created. Not much of note occurred during the EIS tests, but they were used to determine the frequencies used to run Mott-Schottky tests. Figures 2.6(a) and (b) show the data for the two different nano-structures in H_2SO_4 and at different annealing conditions. The annealed data fits with the left Y-axis and the as-anodized data fits with the right Y-axis. Even though the magnitude of the curve is different, the slopes are pretty similar within that order of magnitude.

Also, they all demonstrate n-type semiconductivity. Oxygen vacancies in the material, like those indicated from Figure 3(d), are probably the biggest contributor to this behavior.

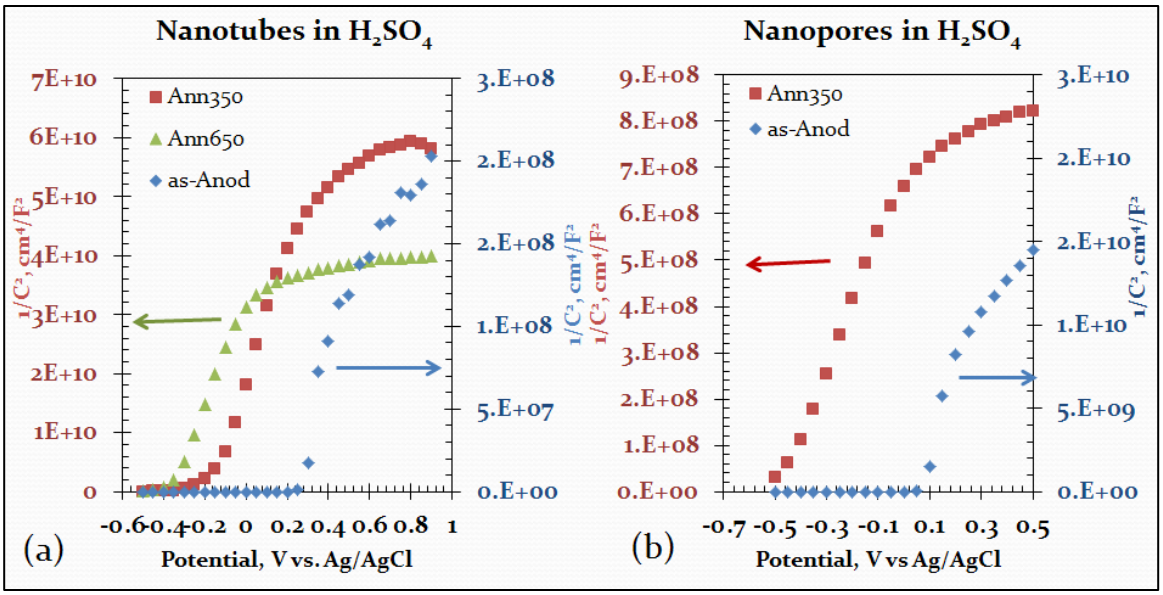

Figure 2.6: Mott-Schottky data for the two different nanostructures (and their annealed conditions) in 1M H_2SO_4. (a) nanotubes, (b) nanopores

From these linear slopes, however, the charge defect density was calculated for the different mixed-oxide structures and some of that data is presented in Table 2.1. Clearly, at the early stages of the annealing process the number of charge carriers, such as oxygen

vacancies, is reduced, but at the higher annealing temperatures surface ions begin to diffuse, raising the defect density. This rise in charge carriers may explain why the samples annealed at 650^{o}C showed, on average, higher capacitance than those samples annealed at 350^{o}C.

Table 2.1 – Defect Concentrations

Condition	**N_D of Nanotubes (cm^{-3})**	**N_D of Nanopores (cm^{-3})**
As-Anodized	9×10^{21}	8.3×10^{21}
Annealed at 350^{o}C	4.5×10^{19}	7.4×10^{21}
Annealed at 650^{o}C	6.1×10^{19}	$>10^{22}$

The final tests run on the samples were the two-electrode galvanostatic-capacitor simulating tests. In most cases the mixed-oxide demonstrated charge and discharge times of <10 seconds for constant currents between 1μA-100μA. They also seemed to exhibit a process where their charge and discharge times increased with the number of cycles, improving its capacitance. The degree of improvement changed based on the conditions of the experiment. For example, Figures 2.7(a) and (b) shows selected cycles from one of the charge/discharge tests. The nanostructure and annealing temperature were the same for both tests. Only the electrolyte (and the charge current, but that didn't seem to affect any of the other experiments) was different. The samples in the low pH solution showed a greater degree of improvement than those in the near-neutral pH. From other tests, it was determined that low pH and low annealing temperature had a significant effect on the time-lengthening process, but the actual nanostructure of the mixed-oxide didn't really affect it at all.

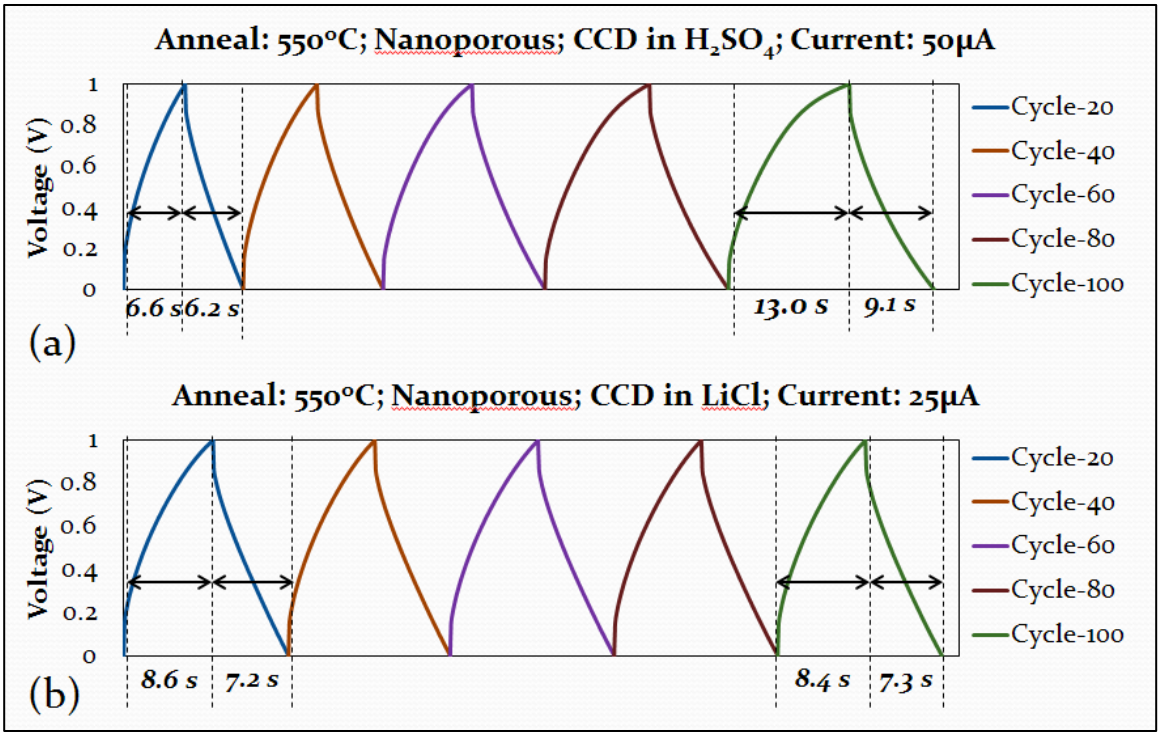

Figure 2.7: Selected cycles from two-electrode tests comparing the "aging" process for two electrolytes of different pHs. The charge and discharge times are included as an indicator of the difference in aging for the electrolytes

4. Conclusion

The anodization of Zr-20 wt% W metal alloy results in a nanotubular structure at 40 V and a nanoporous strucuture at 60 V. Both ZrO_2-WO_3 mixed-oxide nanotubes and nanopores show good capacitance. On average, however, nanopores show greater capacitance than nanotubes, and they both show a greater capacitance at a more neutral pH. While the pseudocapacitance is a major contributor to the overall capacitance, especially in the as-anodized form of the mixed-oxide, the charge carrier density also plays an important role in the capacitance of the annealed mixed oxide structures. The nanostructure arrays undergo a process where the capacitance of the material improves when they are subjected to many

charge/discharge cycles. The degree of this improvement process is heavily affected by the pH of the solution and the temperature at which the sample was annealed. It is less affected by the actual nanostructure of the material.

5. Acknowledgments

The financial support of the Defense Advanced Research Projects Agency (DARPA) through Grant # YFA N66001-12-1-4252 is gratefully acknowledged.

6. References

[1] M. Salari, S. H. Aboutalebi, K. Konstantinov, and H. K. Liu, *Phys. Chem. Chem. Phys.* **13**, 5038 (2011).

[2] Y. Yang, D. Kim, M. Yang, and P. Schmuki, *Chem. Comm.* **47**, 7746 (2011).

[3] J. H. Kim, K. Zhu, Y. Yan, C. L. Perkins, and A. J. Frank, *Nano Lett.* **10**, 4099 (2010).

[4] F. Muratore, A. Baron-Wiechec, T. Hashimoto, A. Gholinia, H. Habazaki, P. Skeldon, and G. E. Thompson, *Electrochem. Solid State Lett.* **15**, C8 (2012).

[5] D. Kowalski, Y. Aoki, and H. Habazaki, *Angew. Chem. Int. Ed.* **48**, 7582 (2009).

[6] Miller, W., C. W. Smith, D. S. Mackenzie, and K. E. Evans, *J. Mat. Sci.* 44(20), 5441 (2009).

[7] H. Habazaki, S. Koyama, Y. Aoki, N. Sakaguchi, and S. Nagata, *ACS Appl. Mater. Interfaces* **3**, 2665 (2011).

[8] I. M. Szilágyi, B. Fórizs, O. Rosseler, A. Szegedi, P. Németh, P. Király, G. Tárkányi, B. Vajna, K. Varga-Josepovits, K. László, A. L. Tóth, P. Baranyai, and M. Leskelä, *J. Catal.* **294**, 119 (2012).

[9] T. L. Barr, *J. Vac. Sci. Technol. A* **9**, 1793 (1991).

[10] W. Grünert, E. S. Shpiro, R. Feldhaus, K. Anders, G. V. Antoshin, and K. M. Minachev, *J. Catal.* **107**, 522 (1987).

[11] D.-Y. Cho, S.-J. Oha, Y. J. Chang, T. W. Noh, R. Jung, and J.-C. Lee, *Appl. Phys. Lett.* **88**, 193502 (2006).

[12] L. Xu, Z. Wu, W. Zhang, Y. Jin, Q. Yuan, Y. Ma, and W. Huang, *J. Phys. Chem. C* **116**, 22921 (2012).

[13] E. Deltombe, N. de Zoubov, and M. Pourbaix, Section 10.3: Tungsten, in: *Atlas of Electrochemical Equilibria in Aqueous Solutions*, p. 280 (1974).

CHAPTER 3

Formation and Electrochemical Characterization of Anodic ZrO_2–WO_3 Mixed Oxide Nanotubular Arrays

Stuart R. Whitman, Krishnan S. Raja*

Chemical and Materials Engineering, University of Idaho, 875 Perimeter Drive, MS# 3024, Moscow, ID 83844-3024, USA

This article is published in the Applied Surface Science scientific journal in the year 2014, volume 303, from pages 406 to 413.

Abstract

ZrO_2–WO_3 mixed oxide nanotubes were synthesized by a simple electrochemical anodization route. Theoxide nanotubes contained a mixture of metastable hexagonal WO_3 and monoclinic (and orthorhombic)ZrO_2 phases, as well as a mixed-oxide ZrW_2O_8 phase that showed a metastable tetragonal symmetry. Evaluation of photo-activity of the materials showed generation of photo-potentials of −85 mV and −230 mV in the as-anodized and annealed conditions. Because of the mismatch in the band edge positions of theWO_3 and ZrO_2 phases and the resultant relaxation of photo-generated charge carriers, no significant photo-current density could be observed. The arrays of oxide nanotubes are considered for electrochemical capacitor application because of their morphology-assisted fast charge/discharge kinetics and large surface area. Presence of a large concentration of charge defects (on the order of $10^{21}cm^{-3}$) and the reported high proton conductivity of the ZrO_2–WO_3 mixed oxide rendered high capacitance, which decreased with an increase in the scan rate of cyclic voltammetry. The highest measured capacitance was 40.03 mF/cm^2 at a scan rate of 10 mV/s and the lowest was 1.93 mF/cm^2 at 1 V/s in 1 M sulfuric acid solution.

1. Introduction

Ordered arrays of oxide nanotubes have been synthesized by electrochemical anodization of pure transition metals such as Ti, Zr, Ta, Hf, Nb, W, and Fe. These oxide nanotubes find applications as electrode materials for solar energy conversions, energy storage devices, improvised chemical sensors, photo-catalysts for removal of toxic chemicals, and biomaterials. Ordered arrays of ZrO_2 nano-tubes were obtained by the anodization of Zr substrate in fluoride containing aqueous or organic solvents at 20–50 V [1,2]. The as-anodized ZrO_2 nanotubes showed a cubic structure [1] when the oxide layer was intact with the substrate. On the other hand, Fanget al. [2] reported an amorphous anodic ZrO_2 nanotubular layer in the as-anodized condition when the layer was removed from the substrate and transformed into the amorphous structure of a mixture of tetragonal + monoclinic phases when thermally annealed at 400◦C and then into a complete monoclinic structure at 900◦C. Formation of well-defined and ordered nanotubular morphology of WO_3 has not been reported by anodization of a tungsten substrate. A nanoporous, thin anodic WO_3 layer has been synthesized by the anodization of tungsten in acidified fluoride solution at 40 V [3]. Recently, formation of several micrometers thick nanochannels of WO_3 has been reported by anodization in 0.2 M NH_4NO_3 dissolved in ethylene glycol [4]. The as-anodized WO_3 was reported as amorphous and transformed to a predominantly monoclinic structure upon annealing at 450◦C.

Anodization of alloyed transition metals gives mixed oxide nanotubes. These mixed oxide nanotubes show enhanced properties. For example, Kowalski et al. [5] reported high proton conductivity in anodic, ZrO_2/WO_3 nanofilms at temperatures below 100◦C. ZrO_2–WO_3 based materials are considered efficient and strong solid-acid catalysts for the

isomerization of alkanes which leads to production of high quality gasoline. Furthermore, binary ZrO_2–WO_3 results in ZrW_2O_8 phase, which is considered to have negative thermal expansion coefficient. Recently Muratore et al.[6] reported growth of porous anodic oxide film on a Zr–36 wt%W alloy substrate and showed the distribution of tungsten ions in the oxide layer using Rutherford backscattering spectroscopy. The top portion of the oxide nanotubes contained, essentially, ZrO_2 and the bottom half of the nanotubes contained the slowly migrating W^{6+} ions proportional to the substrate composition. Since neither annealing nor XRD characterization was reported, the phase content of the mixed oxide nanotubes was not known. Since metastable or high temperature phases could be retained at room temperature by incorporation of aliovalent ions and tailoring the nanoscale manufacturing process, Zr–20 wt% W alloy substrate was anodized in different conditions, in this presentation, to investigate the possibility of forming oxide nanotubes that contain phases like ZrW_2O_8 and hexagonal WO_3 distributed in the ZrO_2.

There is also the potential for ZrO_2 to stabilize the highly-dielectric WO_3 for improved structural stability [7,8]. Hexagonal WO_3 has an open-tunnel-like structure that shows potential for enhanced intercalation of ions. Stabilization of the hexagonal WO_3 structure was attributed to incorporation of cations, such as NH_4^+, and K^+, in the hexagonal channels [9,10]. The contribution of Zr^{4+},W^{6+}, NH^{4+}, and F^- ions in stabilizing various phases in the anodic oxide nanotubes of Zr–W alloy and their effect on charge intercalation were investigated in this study.

ZrO_2 has been considered as a photocatalyst whose energy band gap varies between 3.1 and 5 eV depending on the crystal-lite size, morphology, and the processing history [11,12]. Mixed oxides containing ZrO_2, such as $ZrTiO_4$ [13] and ZrW_2O_8 [14] also have been

investigated as photo-catalyst by examining the photo-decolorization of methyl orange. Tungsten trioxide has been used as a stand-alone photo-anode for splitting water [15,16] as well as tandem cells involving TiO_2 for better light harvesting efficiency [17]. When supported by another metal oxide such as silica or titania, WO_3 showed interesting catalytic properties [18]. Martin et al. observed no significant increase in the photo-activity of ZrO_2 and Nb_2O_5 when loaded with WO_3 for photo-oxidation of 4-nitrophenol [19]. The photo-electrochemical activity of ZrO_2–WO_3 mixed oxide has not been reported widely.

Nanotubular arrays of TiO_2, mixed V_2O_5–TiO_2, and NiO–TiO_2 have been investigated as potential electrochemical capacitor or supercapacitor materials [20–22]. The ordered-oxide nanotubular arrays facilitate faster kinetics of charge/discharge processes that result in high power density. The transition metal substrate on which the oxide nanotubes are formed acts as a current collector. Therefore, an electrode manufacturing step, involving coating with a slurry of active material + conductive additives which is followed in the conventional process, could be avoided. For TiO_2 nanotubes, a capacitance of up to 911 $\mu F/cm^2$ has been reported that was two orders of magnitude higher than the conventional capacitors operated, based on the electric double-layer capacitance. An ordered network of mesoporous WO_3 was prepared [23] by a silica-templated process and used as a supercapacitor with a capacitance of 366 μF/cm2. Habazaki et al. [24] showed enhanced capacitance of anodic ZrO_2 film by stabilizing the high permittivity, tetragonal phase in a highly resistive amorphous phase. WO_3 has been reported to show very high dispersion of large dielectric constant as a function of frequency. Therefore, it is envisaged that very high charge storage capacity could be observed in the ZrO_2 oxide nanotubes by incorporating WO_3.

2. Experimental

2.1: Material and Oxide Nanotube Formation

The starting substrate material for anodization was in the form of 2 mm-thick hot rolled, annealed plate (100 mm × 100 mm) having a composition of 80 wt% Zr and 20 wt% W (obtained from American Elements, Los Angeles, CA, USA). Several 1.5 cm × 1.0 cm size coupons were wire cut from the plate stock and metallurgically wet-polished down to 1500 grit surface finish. The polished surface was cleaned with water, distilled water, and dried in a nitrogen stream before anodization. One centimeter square of the polished and cleaned surface was exposed to the anodization solution and other surfaces were masked by acrylic epoxy paint. The anodization solutions contained varying concentration of NH_4F (0.1–0.3 mole/l), and water (3–15 vol%) dissolved in ethylene glycol. The anodization experiments were carried out at different constant potentials in the range of 20–60 V. A two-electrode configuration was employed for anodization with the Zr–W alloy sample connected to a positive pole of a 60 V, 20 A regulated DC power supply (Sorensen) and a flag-shaped 7.5 cm^2 Pt electrode to the negative pole. The volume of the electrolyte was 200 ml and no stirring occurred. After anodization, the anodized surface was cleaned with methanol. After removing the masking paint with acetone, the sample was washed with acetone for 15–30 s, and dried in a nitrogen stream. Annealing of the samples was carried out in a flowing nitrogen atmosphere using a tube furnace at 450◦C for 2 h. The heating and cooling rate was controlled at 5◦C/min.

2.2: Characterization

The samples' surface morphology was characterized using electron microscopy (FESEM: LEO SUPRA 35VP, TEM: JEOL 2010). Structural characterization of the

nanoporous anodic oxide layer was performed by grazing-angle XRD on a PANalytical X'PertPro MRD diffractometer equipped with a copper X-ray tube and parallel-beam optics. The incident angle was fixed at 0.9◦. X-ray photo-electron spectroscopy (PHI Quantum 2000) was employed to evaluate the surface valence states and electron density of states at the surface of the samples. Mono-chromated Al-Kα (1488.6 eV) radiation was used as the source with an acceptance angle of ±23◦ and take-off angle of 45◦. Charge correction was carried out by considering the C 1s peak at 284.8 eV.

2.3: Photo-electrochemical Testing

Photo-electrochemical characterization was carried out using a three-electrode configuration with a 7.5 cm^2 platinum flag counter electrode, and a home-made AgCl coated silver wire immersed in saturated KCl + AgCl solution contained in a Luggin probe that acted as a reference electrode (calibrated as 199 mV vs. standard hydrogen electrode). The electrolyte was 0.1 M KCl with a pH of 3.45 by addition of diluted HCl. The samples were illuminated using a solar simulator (SOLAR Light, Glenside, PA, USA, Model: 16S-300) with a 300 W xenon lamp, and an air mass global 1.5 filter that gave 1-sun intensity (100 mW/cm^2) at appropriate settings.

2.4: Electrochemical Capacitance

Electrochemical capacitance measurements were carried out using a three-electrode configuration with a 7.5 cm^2 platinum flag counter electrode, and a home-made AgCl-coated silver wire immersed in saturated KCl + AgCl solution contained in a Luggin probe that acted as a reference electrode (calibrated as 199 mV vs. standard hydrogen electrode). The samples were electrically connected with a potentiostat (Gamry Instruments, model: Reference 600) by exposing 1 cm^2 of the active surface. The samples were polarized in 1 M H_2SO_4 solution

and also in 1 M $TEABF_4$ in acetonitrile. Cyclic voltammetry, electrochemical impedance spectroscopy (EIS), and Mott–Schottky analysis studies were carried out with and without illuminated conditions. Cyclic voltammetry was carried out at three different scan rates of: 10, 100, and 1000 mV/s. EIS measurements were taken under a potentiostatic condition of 0.2 V by superimposing an AC signal of 10 mV and scanning with a frequency from 0.1 MHz down to 0.1 Hz. Mott–Schottky type measurements were carried out at a frequency (f) of 318 Hz by scanning the potential of the sample from −0.5 V to 0.9 V at 50 mV steps for every 2 s for H_2SO_4 and from −2.0 V to 2.0 V at the same rate for $TEABF_4$. The capacitance (C) of the space charge layer was calculated from the imaginary impedance (Z") using the relation $C = -1/(2\pi fZ")$. All potentials were applied with reference to a Ag/AgCl reference electrode. Additional electrochemical capacitance tests were performed with a two-electrode setup. The apparatus used two identically-prepared, annealed samples as electrodes in the system to model a capacitor in practical applications. Approximately 1 cm^2 of the anodized portion of each sample was submerged in 1 M H_2SO_4 solution and one sample was selected to be the working electrode and the other was the counter/reference electrode. This set-up was subjected to cyclic charging and discharging tests. By supplying a constant current of 10 μA, the system charged until the potential reached 1 V, at which point it would begin to discharge by supplying the same current in the opposite direction. Once the potential reached 0 V, the cycle restarted. This was repeated 100 times to check for any rapid degradation in the material.

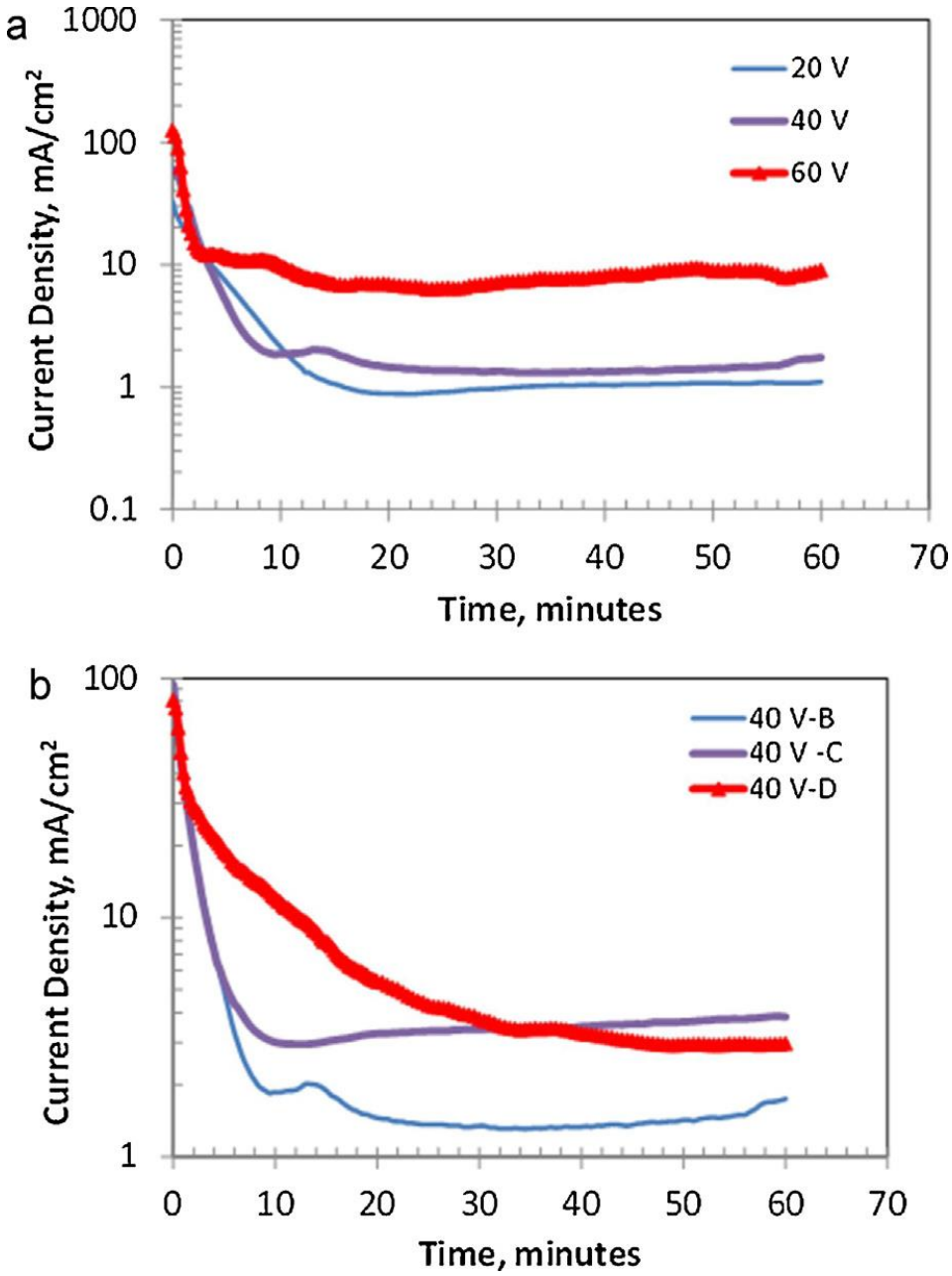

Figure 3.1: Current transients during anodization of Zr–20wt% W alloy in fluoride containing ethylene glycol (EG) at different anodization conditions. (a) Anodization in 0.2 M NH_4 + 5 vol% H_2O in EG at different potentials; and (b) anodized at 40 V in three different EG based electrolytes (B: 0.2 M F−+ 5 vol% H_2O, C: 0.25 M F^-+ 10 vol% H_2O, D: 0.3 M F^-+ 15 vol% H_2O).

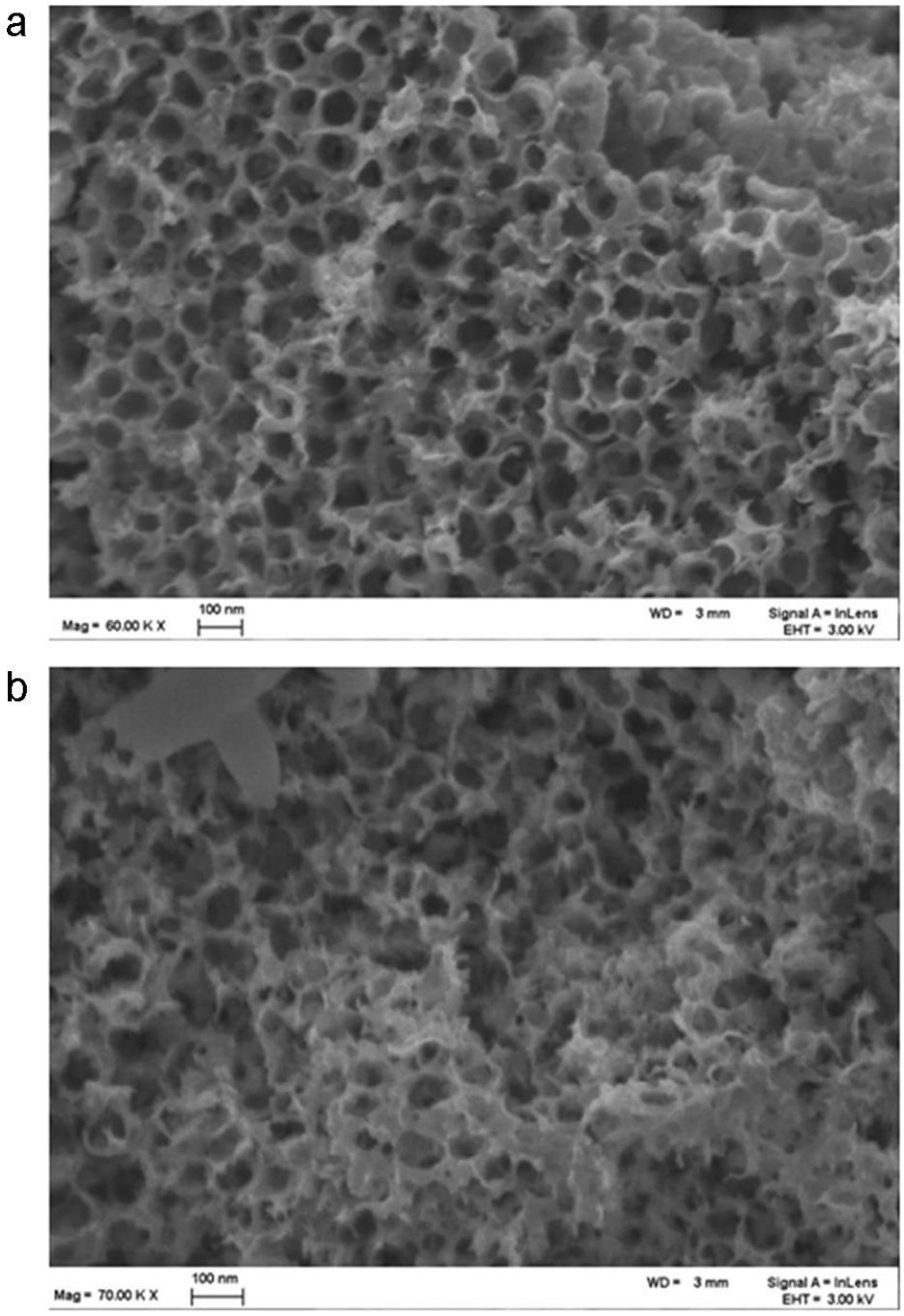

Figure 3.2: FESEM images of oxide layers formed on the Zr–W alloy substrate after anodization at 40 V for 1 h in different EG electrolytes containing, (a) 0.15 M NH_4F + 3 vol% H_2O; (b) 0.25 M NH_4F + 10 vol% H_2O

3. Results and Discussion

3.1 Nanotube Formation and FESEM

Current transients were recorded during the anodization of the Zr–W alloy in different electrolytes. While other alloy compositions are possible, producing defect-free coupons becomes increasingly difficult as the fraction of tungsten increases. These types of alloys are made by powder sintering and increasing the tungsten content led to poor densification. For example, a 50:50 alloy was tested prior to this experiment, which inherently contained a large porosity. Anodization of the porous substrate did not result in a uniform nanoporous oxide layer and its characterization was difficult. Therefore, this investigation focused on a single alloy com-position (80 wt% Zr–20 wt% W) that yielded reproducible, uniform, nanoporous oxide layer upon anodization in different conditions. The Zr–W binary phase diagram indicated that the microstructure of the Zr–20 wt% W alloy will show a maximum of 11.1% ZrW_2 phase distributed in the Zr–W solid solution at 2008 K. The ZrW_2 secondary phase content and distribution will vary at room temperature depending on the cooling rate from high temperature and heat treatment cycles during the manufacturing process.

Fig. 3.1(a) shows the current transients of the anodization in ethylene glycol containing 0.2 M NH_4F + 5 vol% water at 20, 40, and 60 V. The current transients showed three stages of a decrease–increase–decrease trend similar to that reported during the anodization of Ti and other transient elements [25,26]. The three stages of current transients could be clearly discerned in the case of anodization at 40 V. The anodization current exponentially decayed for the first 8.5 min from 61 mA/cm^2 to 1.84 mA/cm^2. An increasing trend was observed from 8.5 min to 13 min until the current density reached a value of 2.02 mA/cm^2 after which the current density decreased and reached a steady state value of 1.4

mA/cm^2. The steady state current density increased with an increase in the anodization potential. Observations under the electron microscope indicated that the sample anodized at 40 V showed ordered arrays of oxide nanotubes. The sample anodized at 60 V showed a large nanoporous oxide layer. A mixed morphology of nanoporous and nanotubular structures was observed on the sample anodized at 20 V. Therefore, further anodization experiments were carried out at 40 V in other electrolytes. Fig. 3.1(b) shows the current transients of anodization experiments carried out at 40 V in different electrolytes. The water of the electrolyte was increased with an associated increase in the fluoride content. The decrease–increase–decrease behavior was observed in the electrolytes containing 0.2 M NH_4F + 5 vol% water (denoted as B) and 0.25 M NH_4F + 10 vol% water (denoted as C). The electrolyte containing 15 vol% water and 0.3 M fluoride showed only a current decay behavior. The nanotubular oxide morphology was prevalent only when the current transient trend showed an initial current decay followed by an increase in the current density and then a decrease before reaching a steady-state current density value. The current transient as observed in 40 V-D of Fig. 3.1(b) did not result in the nanotubular oxide morphology. Fig. 3.2 shows the FESEM images of the top surface morphology of the oxide layer formed during anodization of Zr–W alloy at 40 V in two different electrolytes such as: (a) 0.15 M NH_4F + 3 vol% H_2O; (b) 0.25 M NH_4F + 10 vol% H_2O. These electrolytes did not result in the nanotubular oxide morphology at 40 V anodization but showed formation of nanoporous oxide layer. Further observation of Fig. 3.2(a) might show that a nanotubular layer exists under the nanoporous layer, but since electrolyte B produced the best looking results, that is the electrolyte chosen for this experiment. It is possible that nanotubular oxide structure formations may exist at

other anodization potentials in these electrolytes, but no attempts were made in this investigation.

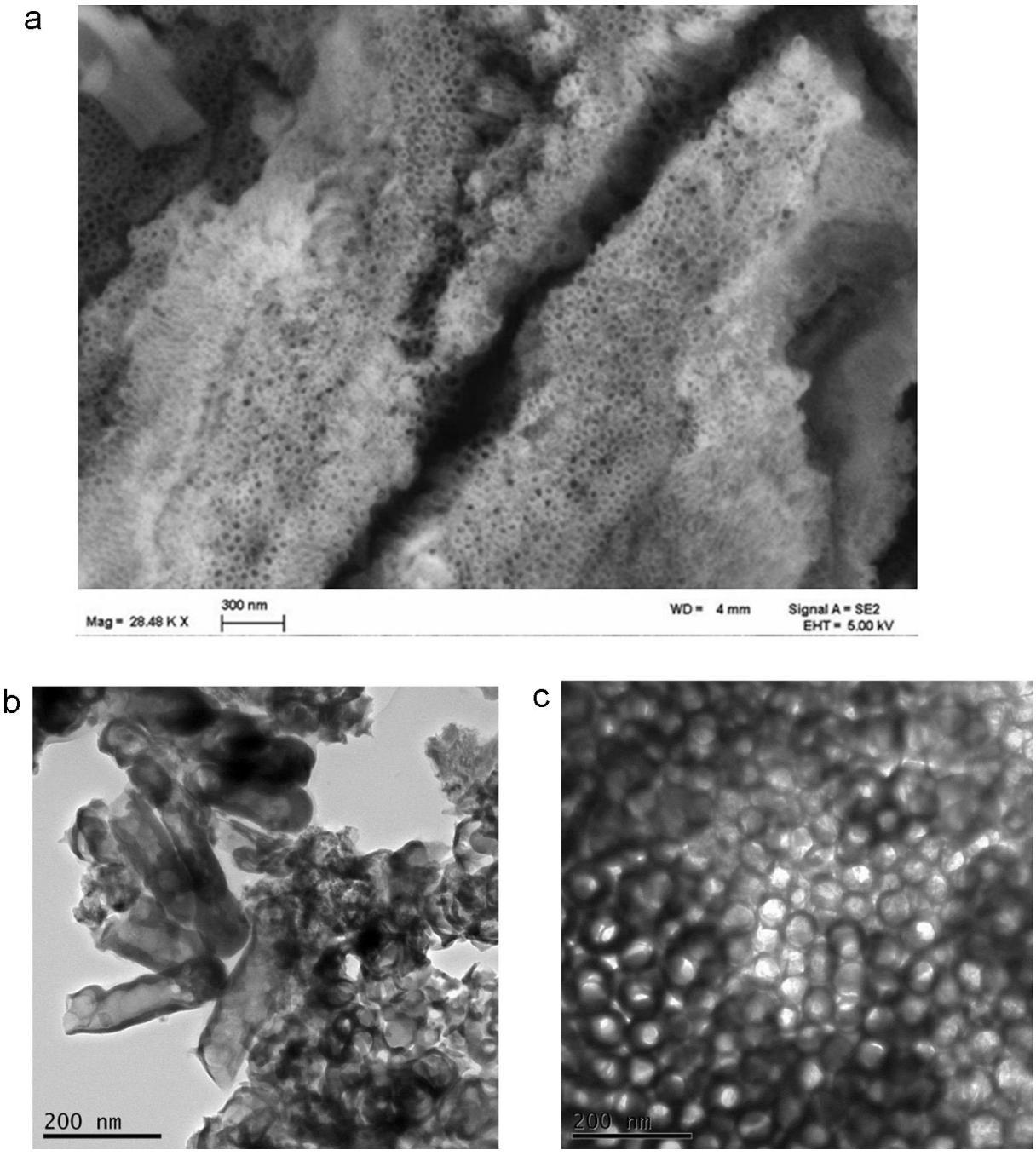

Figure 3.3: Electron microscopic images of oxide layers formed on the Zr–W alloy substrate after anodization at 40 V for 1 h in EG electrolyte containing 0.2 M NH_4F + 5 vol% H2O. (a) FESEM image of the top surface of the anodic oxide layer revealing nanotubular morphology;

(b) TEM image of the side view of the nanotubes; and (c) planar view of the nanotubes under TEM.

Fig. 3.3(a) shows the FESEM image of the oxide nanotubes formed on the Zr–W alloy after anodization at 40 V for 1 h in ethylene glycol containing 0.2 M NH_4F + 5 vol% water. Fig. 3.3(b) shows a TEM image of some of the disordered nanotubes in their length direction. The morphology of the nanotubes in the planar direction is given in Fig. 3.3(c). The inner diameter of the oxide nanotubes was in the range of 40–63 nm and the wall thickness varied from 10 to 14 nm. Unfortunately, due to the degree of disorder in the tubes, the cohesiveness of the oxide layer to the alloy substrate, and the inability to get a proper cross-sectional image of the layer, the thickness of the oxide layer and length of nanotubes are unknown. In order to correlate the current transient during the anodization with the evolution of oxide morphology, the anodization was interrupted at various time intervals and the surface of the anodic oxide was observed under the scanning electron microscope. The results are presented as Fig. 3.4(a)–(f). During the initial current decay (just after 10 s of anodization at 40 V), an oxide layer containing uniformly distributed pit like nano-pores formed. Initially the pores were less than 10 nm in size which increased with the anodization time. There was no apparent increase in the pore density with the time. Therefore, the nucleation of nanopores could be considered as an instantaneous process. The nanopores widened as the anodization progressed. After 300 s of anodization, the entire surface of the sample was covered with a well-developed nanoporous oxide layer. The nanoporous surface layer started transforming into a nanotubular oxide layer after 600 s of anodization. Anodization for 1800 s showed a fully developed, ordered array of nanotubular oxide that was more than 300 nm in length. In the 1800-s sample, there is clear evidence of small sections of nanotubes peeling from the surface. This

can also be seen in Figs. 3.3(a) and 3.4(e). Upon further investigation, we determined that this cracking/peeling was purely superficial and had no effect on the electrochemical tests that were performed on these samples. Since the peeling was more noticeable in the 1800-s sample than in any of the 1-h samples, it seems likely that further anodization covers up any bare spots on the Zr–W alloy surface.

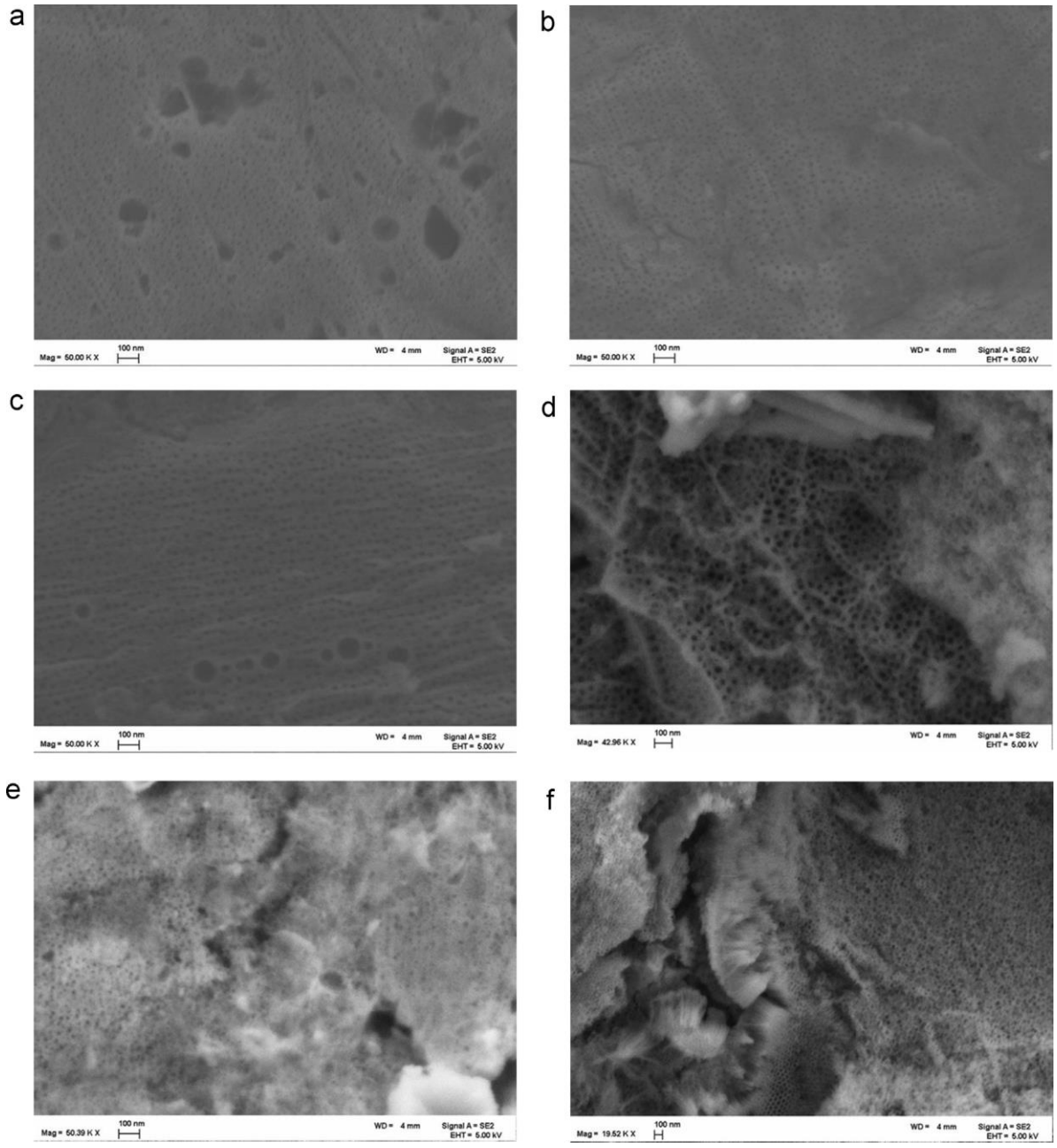

Figure 3.4: Electron microscopic image of oxide layers formed on the Zr–W alloy substrate after anodization at 40 V in EG electrolyte containing 0.2 M NH_4F + 5 vol% H_2O (a) for 10 s, (b) for 30 s, (c) for 60 s, (d) for 300 s, (e) for 600 s, (f) for 1800 s.

3.2: XRD Characterization

The glancing angle XRD pattern in Fig. 3.5 shows the presence of several oxide phases in the sample that was annealed at 450◦C for 2 h. Some of the notable phases are the hexagonal WO_3, tetragonal ZrW_2O_8, and monoclinic and orthorhombic ZrO_2 phases. There are also several peaks in the as-anodized data labeled as "Zr–W". These are the signals from the metal substrate and are irrelevant to the current investigation. The anodic oxides of pure metals of Zr and W were reported as amorphous in the as-anodized condition [27,28]. The amorphous anodic oxides were transformed to crystalline phases only after thermal annealing. The transformation to monoclinic structure upon annealing has also been reported for both WO_3 and ZrO_2 anodic oxides. In this investigation, the anodic oxide of Zr–W alloy contained WO_3 in the form of a hexagonal phase. It is well documented that the hexagonal tungsten trioxide (h-WO3) is a metastable phase. The monoclinic phase of WO_3 is considered to be stable at room temperature. In the mono-clinic phase, W–O bonding has an octahedral coordination and the corners of the WO_6 octahedra are connected in a chessboard-like arrangement [10]. In the case of hexagonal WO_3, the WO_6 octahedra are arranged in a circular ring shape that creates a hexagonal tunnel within each ring [9]. Incorporation of cations like Na^+ orNH^{4+} in the hexagonal tunnels has been considered to stabilize the hexagonal phase. Possible lattice distortions induced by oxygen vacancies are also considered to play a role in stabilizing the hexagonal phase [10]. In this investigation, both the presence of NH^{4+} cations through addition of ammonium fluoride in the anodization solution and the formation of a

high concentration of oxygen vacancies during the anodization at high electrochemical potential could have helped stabilize the hexagonal WO_3 phase in the oxide nanotubes.

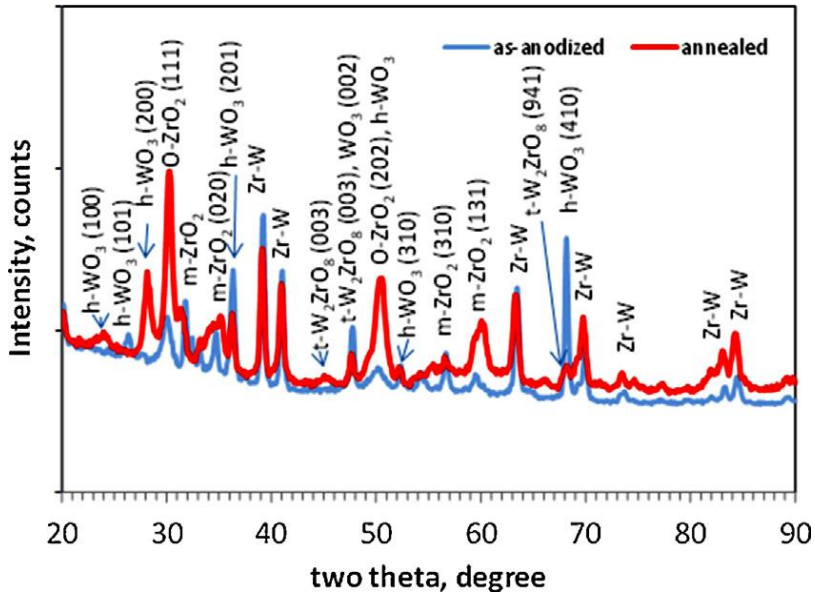

Figure 3.5: Glancing angle X-ray diffraction patterns of oxide layers formed on the Zr–W alloy substrate after anodization at 40 V for 1 h in EG electrolyte containing 0.2 M NH_4F + 5 vol% H_2O in thermal annealed (450◦C for 2 h) condition.

3.3: Binding Energy Analysis

Fig. 3.6(a) shows the high resolution X-ray photoelectron spectrum of W $4d_{5/2}$ for the as-anodized and annealed, anodic Zr–W oxide samples. The binding energy peak of W $4d_{5/2}$ occurred at 248.25 and 247.25 eV for the as-anodized and annealed conditions, respectively. The binding energy of the anodized sample was similar to the literature reported value for the W $4d_{5/2}$ peak from WO_3 sample [29]. The lower binding energy of the W $4d_{5/2}$ from the annealed sample could be associated with the increase in its covalency due to formation of the mixed oxide (ZrW_2O_8) during the annealing process. Barr [30] proposed that when a complex mixed oxide forms by the mixing of two oxides, the cation of the pre-dominantly ionic oxide becomes even more ionic and the cation of the covalent oxide should experience an increase

in its covalency. The changes in the charge borne by the cations in the mixed oxide as compared to the individual binary oxides can be elucidated by considering the binding energy shifts. By the ab-initio modeling and XPS measurements, Guittet et al. [31] showed that the Zr $3d_{5/2}$ peak of $ZrSiO_4$ shifted to a higher binding energy than that of ZrO_2 and the Si-2p peak of $ZrSiO_4$ shifted to a lower binding energy than that of SiO_2. In the mixed oxide of ZrW_2O_8, Zr is the more ionic cation and W has a predominantly covalent character.

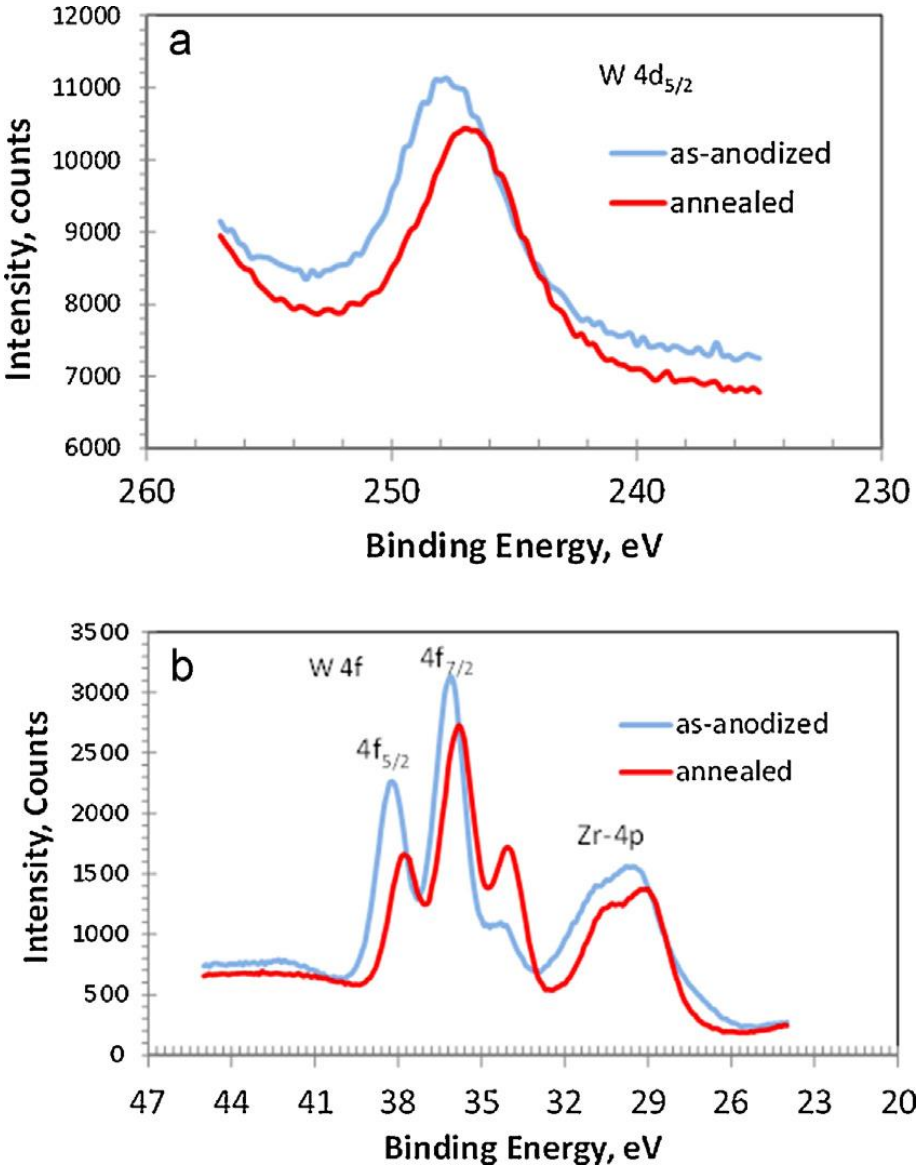

Figure 3.6: High resolution X-ray photo-electron spectra of anodic oxide of Zr–W alloy prepared by anodization in EG electrolyte containing 0.2 M NH_4F + 5 vol% H_2O at 40 V for 1 h. (a) W-4d spectrum; (b) W-4f and Zr-4p spectrum.

The shift in the binding energy of W $4d_{5/2}$ after annealing could be associated with the conversion of some of the h-WO_3 phase into ZrW_2O_8 phase as observed from the XRD result. During this process, it is expected that the binding energy of the Zr cation should increase as the ionic cation would become more ionic upon incorporation into the mixed oxide. The positive shift in the binding energy of the Zr-3d spectra of the annealed sample, shown in Fig. 3.7(a), supports the formation of a mixed oxide. However, there was no significant shift in the binding energy of Zr-4p peaks between the as-anodized and annealed conditions as seen in Fig. 3.6(b). The spin–orbit splitting of W-4f of the as-anodized sample occurred at 36.2 and 38.2 eV as W-$4f_{7/2}$ and W-$4f_{5/2}$ peaks respectively. This corresponds to a W^{6+} oxidation state [32]. A shoulder was observed at the low energy end of the W-$4f_{7/2}$ spectrum of the as-anodized sample which could be attributed to the presence of a lower valence state of the W cations, such as W^{5+} or W^{4+}. These lower valence cations are required for charge neutrality when a large concentration of oxygen vacancies forms during the anodization. The shoulder at 34.5 eV was larger for the annealed sample than that of as-anodized sample, which indicated higher concentration of W^{5+}. The intensity of W-4f peaks associated with W^{6+} decreased after annealing. This observation could be attributed to creation of a possible reducing atmosphere during the annealing process by the removal of the NH_4^+ ions that incorporated during anodization in the NH_4F containing electrolyte. This reducing atmosphere resulted in conversion of some of the W^{6+} ions to W^{5+}. Similar observation has been reported by other investigators [33]. The spin-orbital interaction of Zr-3d resulted in splitting of $3d_{5/2}$ and $3d_{3/2}$

by 2.3 eV and the peaks were at 181.0 and 183.3 eV, respectively, for the as-anodized sample as seen in Fig. 3.7(a). The binding energy increased by 0.5 eV for the annealing condition as the ionic contribution increased for the Zr^{4+} in the mixed oxide phase. The peaks at 530.7 and 530.9 eV are associated with the O^{2-} sub-lattice. The as-anodized sample showed a broader shoulder at the higher binding energy side of the O-1s spectrum than the annealed sample.

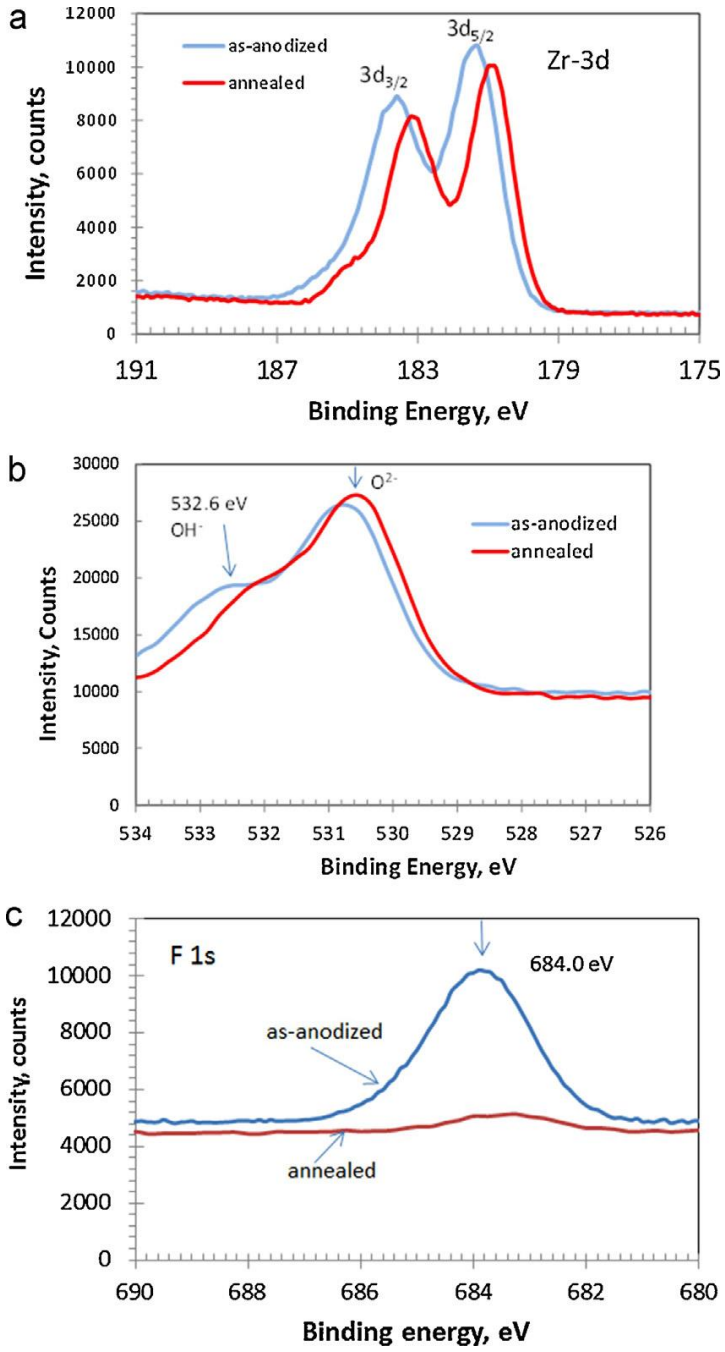

Figure 3.7: High resolution X-ray photo-electron spectra of anodic oxide of Zr–W alloy prepared by anodization in EG electrolyte containing 0.2 M NH_4F + 5 vol% H_2O at40 V for 1 h. (a) Zr-3d spectrum; (b) O-1s spectrum; and (c) F-1s spectrum.

The intensity counts recorded at binding energies greater than 531.9 eV could be attributed to the presence of oxygen deficient regions and chemisorbed oxygen or hydroxyl ions [34,35]. The comparison of O 1s spectra between the as-anodized and annealed samples indicates that the concentration of oxygen vacancies could be higher in the as-anodized sample. This observation could be further corroborated with electrochemical impedance measurements presented in the following section. However, it should be noted that the annealed samples showed larger W-4f shoulder peak at 34.5 eV associated with the W^{5+} ions, but smaller shoulder width for the O 1s associated with oxygen vacancies. Considering the charge neutrality consideration, the shoulder associated with the oxygen vacancy for the annealed sample should be larger than that of as-anodized. It could be observed that the binding energy of O 1s of the annealed sample was shifted to lower values than that of as-anodized. The O 1s peak centered at 530.5 eV could be attributed to the strong W-O bond after annealing and the shoulder observed at 531.3 eV could be attributed to the O^{2-} ions in the oxygen deficient regions [36]. The difference in the O 1s spectra of as-anodized and annealed samples could be attributed to the decrease in the h-WO_3 phase content upon annealing. Fig. 3.7(c) shows the F-1s spectrum of the as-anodized and annealed samples indicating the oxide nanotubes contained fluoride species which were removed during the annealing process. In addition to fluoride species, carbonaceous species also were incorporated from the electrolyte during the anodization. After annealing the concentration of the fluoride was decreased by an order of magnitude as estimated from the XPS data as shown

in Fig. 3.7(c). Similar results were reported by other researchers for the anodization of pure Zr [27] and Zr–W alloy [6].

3.4: Photo-electrochemical Behavior

The photo-electrochemical properties of the Zr–W anodic oxide samples (anodized at 40 V for 1 h in EG electrolyte containing 0.2 M NH_4F + 5 vol% H_2O with and without thermal annealing at 450◦C for 2 h) were evaluated by illuminating the sample under a simulated solar light at 1 sun intensity through an AM 1.5 filter. The electrolyte was 0.1 M KCl with a pH of 3.45 by addition of diluted HCl. Fig. 3.8(a) shows the potentials of as-anodized and annealed samples with and without illumination. There was no significant photo-activity under these test conditions. The Zr–W anodic oxide showed an n-type semiconductivity and the electrochemical potential of the sample shifted to a more negative direction upon illumination. However, the potential shift upon illumination and the interruption of light was very slow indicating that the relaxation kinetics of the photo-generated charge carriers was almost similar to the charge transport kinetics. Therefore, the potential measurements were carried out separately under dark and continuously illuminated conditions. The open circuit potential of the as-anodized sample was about −375 $mV_{Ag/AgCl}$ without illumination. After 1 h of illumination, the open circuit potential was −460 mV, indicating a photo-potential of about −85 mV. The annealed sample showed a positive open circuit potential of around 170 mV without illumination and shifted to −60 mV when illuminated which makes the maximum photo-potential developed −230 mV. Fig. 3.8(b) shows the I–V characteristics of the annealed sample. The maximum photo-current was only about 0.1 mA/cm^2 recorded at 1 $V_{Ag/AgCl}$. This potential is greater than the standard potential

for oxygen evolution in the pH: 3.45 solution. No significant photo-current was recorded for the as-anodized sample.

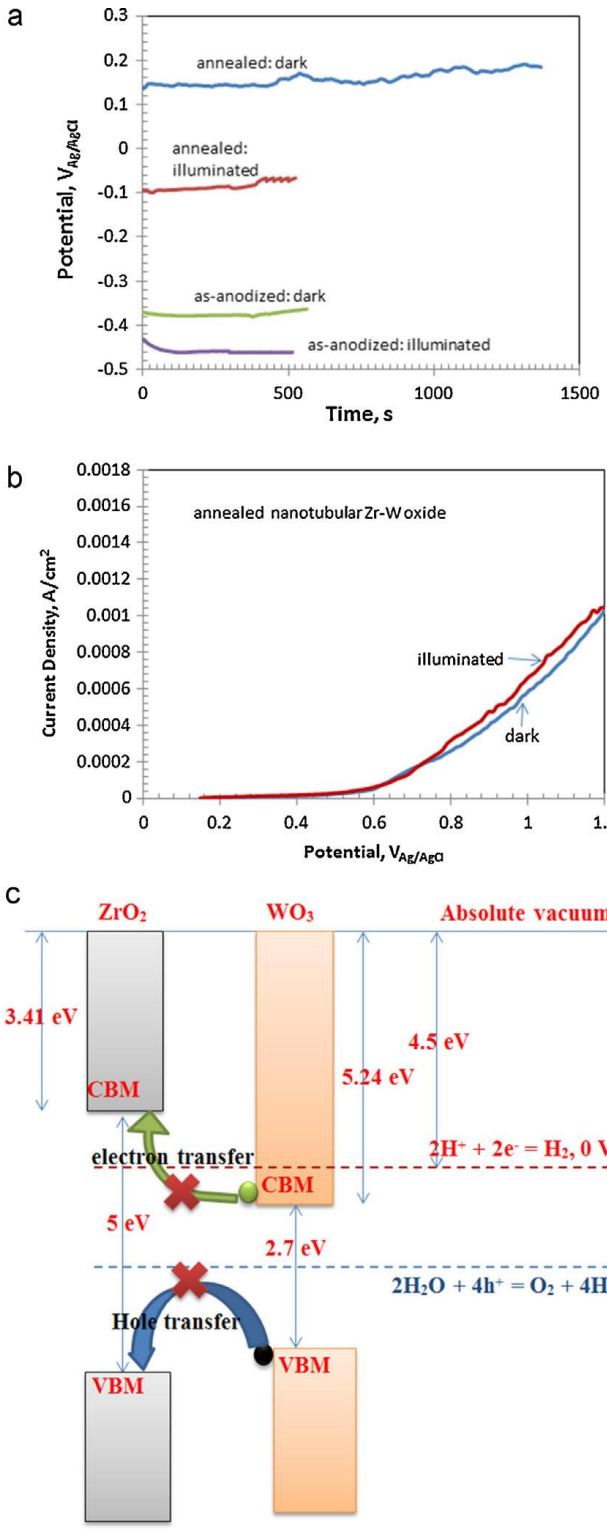

Figure 3.8: Photo-electrochemical results of anodic oxide of Zr–W alloy in as-anodized (40 V, 1 h) and annealed (450◦C for 2 h) conditions with and without illumination in pH 3.45 electrolyte. (a) Open circuit potentials, and (b) I–V characteristics of the annealed sample, (c) schematic illustration of the band edge energy levels of the ZrO_2 and WO_3 with reference to absolute vacuum level. CBM: conduction band minimum, VBM: valence band maximum. The data are from [35].

Even though high photo-current density has been reported for WO_3 materials tested in the form of nanoporous layers [3] and thin films [37], ZrO_2 has been considered an insulator (band gap∼5.0 eV). Considering the energy levels of band edge positions of ZrO_2 and WO_3 based on the data given by Xu and Schoonen [38] it can be shown that the electron or hole transfer from WO_3 to ZrO_2 would be energetically unfavorable. Fig. 3.8(c) schematically illustrates the relative band edge positions of ZrO_2 and WO_3. Since the conduction band minimum (CBM) of the ZrO_2 lies above the CBM of the WO_3 by 1.83 eV, the electrons generated by energetic photons in the WO_3 cannot be transported through ZrO_2. The band gap of hexagonal WO_3 was reported to be 0.17 eV larger than that of monoclinic WO_3 [6]. In case of the nanostructured h-WO3, the reported band gap was 3.05 eV [39]. The increase in the band gap of the h-WO_3 would not affect the band edge positions significantly, especially the conduction band minimum level. Since the wave-lengths of the solar spectrum at sea level are longer than 250 nm, no energetic photons are available to generate electron–hole pairs in the ZrO_2. Therefore, in order to extract any photo-current, either an electric field should be present to drive the charge carriers, surpassing the contact potential gradient between the WO_3–ZrO_2, or a continuous network of WO_3 phases should be present. The absence of significant photo-current in the as-anodized sample indicated that such a continuous high

conductivity network was not present and the photo-generated charge carriers within the WO_3 phase were relaxed at the ZrO_2–WO_3 interface.

The relatively higher photo-potential observed in the annealed sample could be attributed to the presence of a mixed oxide ZrW_2O_8 phase. The band gap of the cubic-ZrW_2O_8 was reported to be 2.84 eV [40]. However, the XRD result showed the presence of a metastable tetragonal-ZrW_2O_8. It is envisaged that the band gap of the tetragonal phase would be marginally smaller than that of highly symmetric cubic phase. Since the bond length of Zr–O and W–O would increase with the lack of symmetry, the interaction between the molecular orbitals would decrease and result in a lower energy gap between the bonding and antibonding orbitals. For example, Ouyang et al. [40] reported a reduction in band gap (E_g) of 0.67 eV for the less symmetric orthorhombic phase of ZrW_2O_8 as compared to the cubic phase. The anodic Zr–W oxide nanotubes in the annealed condition contained a mixture of h-WO_3 (E_g~ 2.7–3.05 eV), and t-ZrW_2O_8 (E_g~ 3.5–4.0 eV) in a matrix of m-ZrO_2 (E_g~ 5.0 eV). Even though both h-WO_3 and ZrW_2O_8 were active UV-light harvesters of the solar spectrum, due to the mismatch in the band edge positions between the three phases, a high photo-current was not observed.

3.5: Electrochemical Characterization

Fig. 3.9(a) shows a representative cyclic voltammogram of the ordered arrays of Zr–W oxide nanotubes in the annealed condition (450◦C, 2 h) at different scan rates. The anodization was carried out in EG-B solution at 40 V for 1 h. As discussed in the previous section, the nanotubes had inner diameters in the range of 40–63 nm with wall thicknesses of 10–14 nm and lengths around 600 nm. The cyclic voltammetry results for the annealed samples tested in 1 M H_2SO_4 are given in Fig. 3.9(a). For the sample tested in the organic

electrolyte, Fig. 3.9(b) shows the CV curves for the sample that was tested in the 1 M $TEABF_4$ acetonitrile solution. The electrochemical capacitance behavior of Zr–W anodic oxide nanotubes can be described by three processes: (1) electrochemical double-layer (EDL), (2) pseudo capacitance (PC), and (3) space layer charging capacitance (SL). The EDL capacitance is based on the physical separation of electronic charges in the oxide nanotubes and the H^+/SO_4^{2-} ions adsorbed on the oxide nanotubes from the 1 M H_2SO_4 electrolyte during the potential sweeps. The pseudocapacitance can be attributed to the Faradaic reactions (1) and (2) given below due to chemisorption of H^+ and redox reactions of W^{6+}/W^{5+} and W^{5+}/W^{4+} [41].

$$WO_3 + 2H^+ + 2e^- \leftrightarrow 2\ W_2O_5 + H_2O;\ E_0 = -0.23\ V_{Ag/AgCl} \quad (1)$$

$$W_2O_5 + 2H^+ + 2e^- \leftrightarrow 2WO_2 + H_2O;\ E_0 = -0.225\ V_{Ag/AgCl} \quad (2)$$

The space charge layer capacitance is caused by semiconductor-like processes below the immediate surface of the oxide layer. Oxygen vacancies in the material act like holes in a silicon semi-conductor. When a potential bias is applied electrons will fill some of these holes creating a depletion layer that widens or thins based on the amplitude and direction of the bias. Because there is an insulating layer sandwiched between two more conductive layers, capacitance forms.

It should be noted that the Zr^{4+} did not undergo any redox reaction between −0.5 and 0.9 $V_{Ag/AgCl}$. Therefore, the ZrO_2 surface in the oxide nanotubes participated only in the electrochemical double layer capacitance. The isoelectric point of nanosized ZrO_2 could be around pH: 6 [42]. Therefore, a significant double layer capacitance is expected due to the surface potential of the ZrO_2 in the 1 M H_2SO_4 solution. The total current density of the cyclic voltammogram has contributions from the electrochemical double layer capacitance (non-

Faradaic process), the redox reaction due to adsorbed protons (Faradaic process), and space layer charging. However, it should be noted that the non-Faradaic current density has a linear dependence on the Faradaic current density [43]. In the absence of a redox reaction, an ideal EDL capacitor will show a rectangular I–V plot. The radius of the roundness of the corners of the I–V plot will increase with the increase in the charge transfer resistance present in series with the EDL capacitor.

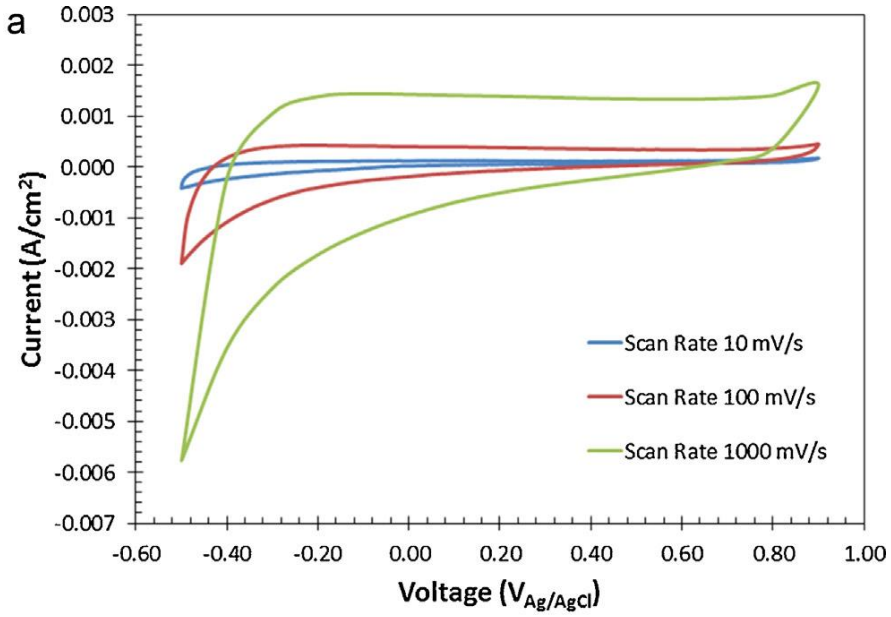

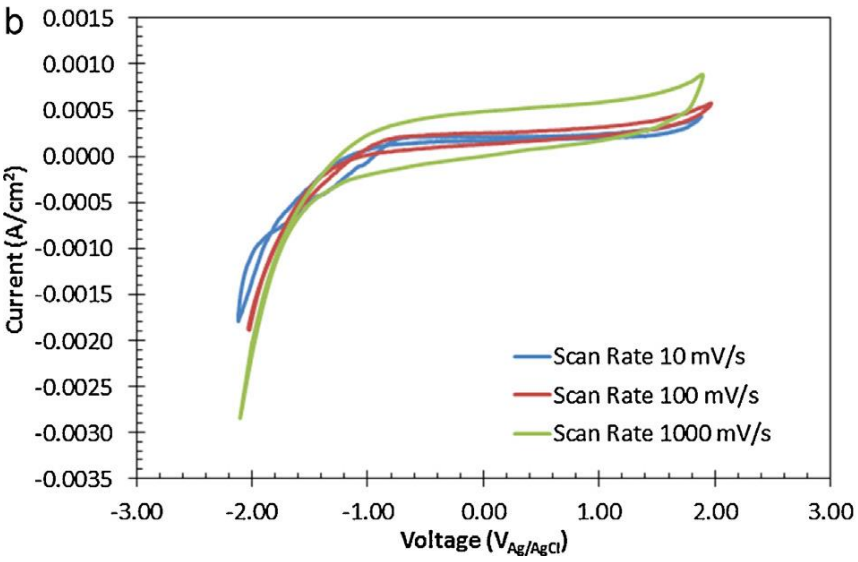

Figure 3.9: Representative cyclic voltammetry (CV) results of annealed Zr–W oxide nanotubes (anodized for 1 h) tested in (a) 1 M H_2SO_4 solution at three different scan rates 10, 100, and 1000 mV/s; (b) 1 M TEABF4in acetonitrile solution at three different scan rates 10, 100, and 1000 mV/s.

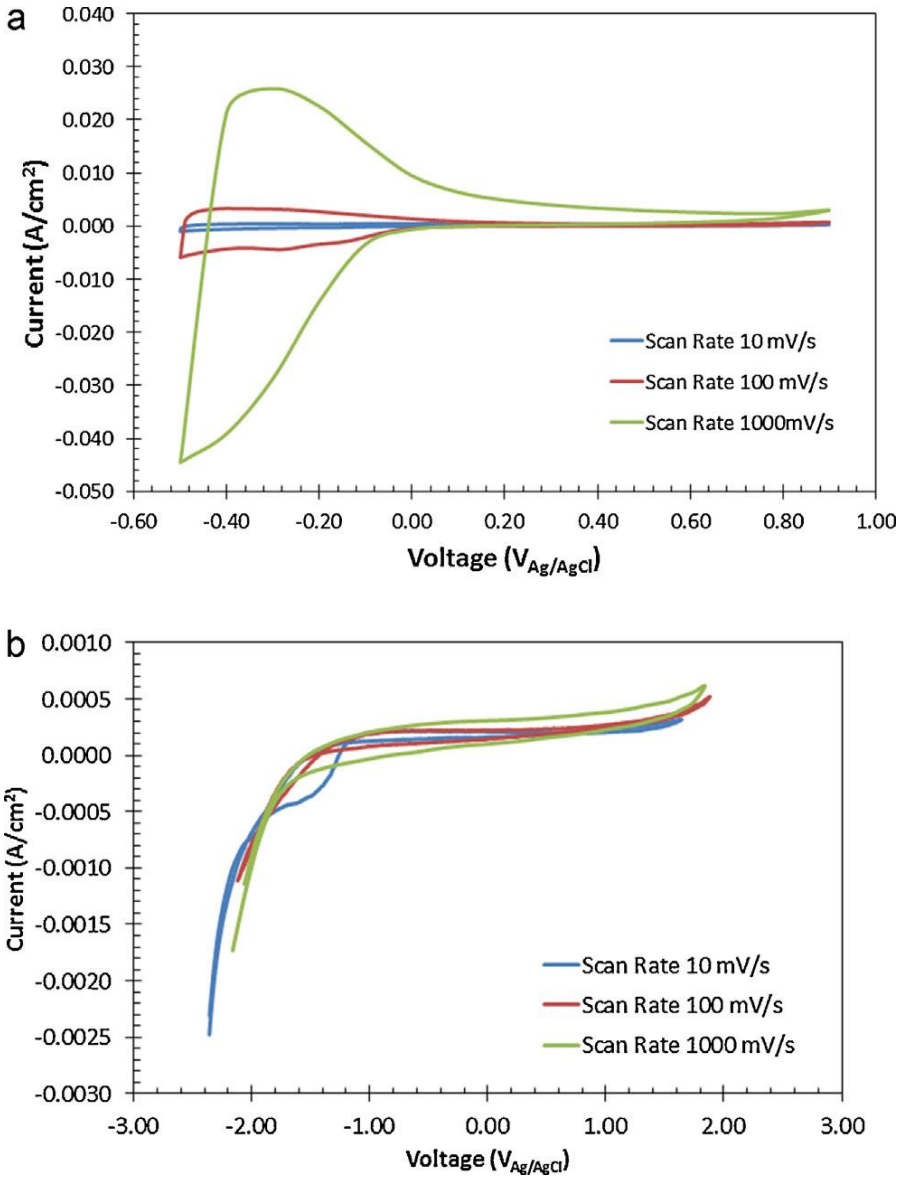

Figure 3.10: Representative cyclic voltammetry (CV) results of as-anodized Zr–W oxide nanotubes (anodized for 1 h) tested in (a) 1 M H_2SO_4 solution at three different scan rates 10,

100, and 1000 mV/s; (b) 1 M $TEABF_4$ in acetonitrile solution at three different scan rates 10, 100, and 1000 mV/s.

The CV plots of the as-anodized samples (Fig. 3.10(a)) show a semi-rectangular plot between 0.2 V and 0.7 V in H_2SO_4 and between −1.0 V and 1.5 V in $TEABF_4$ at slow scan rates that could be attributed to EDL capacitance behavior, where the capacitor was charged and discharged at a constant rate. Peak current behavior was observed at the negative potential region which can be attributed to the on-set of Faradaic reactions. By comparing Figs. 3.9(a) and 10(a), it is clear that the Faradaic reactions are more predominately present in the as-anodized tubes than in the annealed tubes. However, in Figs. 3.9(b) and 3.10(b), the Faradaic reactions seem to be absent above 10 mV/s scan rates. Even at a low scan rate, the current densities for the organic electrolyte are much smaller than their aqueous counterpart. This is reflected in their capacitance values, which are calculated later.

The high current density in the negative potential range of Fig. 3.10(a) is indicative of the tungsten redox reactions that were given in Eqs. (1) and (2). During this process, H^+ atoms are chemisorbed onto the WO_3 phase present on surface of the nanotubes. Along with electrons provided by the system, the W^{6+} is reduced to W^{5+} or even W^{4+}. Because of the reversible nature of these reactions, when the potential is increased to a positive value, the tungsten is oxidized back to W^{6+}. When the scan rate was increased, the current density varied with the potentials. To ensure that the large CV curve in the negative potential range is not due to some crack in the film that may cause a strong reaction in the base metal, a piece of un-anodized, un-annealed Zr–20W metal was placed in the 1 M H_2SO_4 solution and subjected to the same test as the nanotubes. Fig. 3.11 compares the different CV curves of the bare metal and the as-anodized tubes for a scan rate of 100 mV/s. The large portion of the as-anodized

tubes' CV curve is clearly not due to reactions with the base metal alloy. Also, the sample tested inthe organic electrolyte had such small current densities compared to those tested in the aqueous electrolyte that it appears as a nearly straight line across the graph.

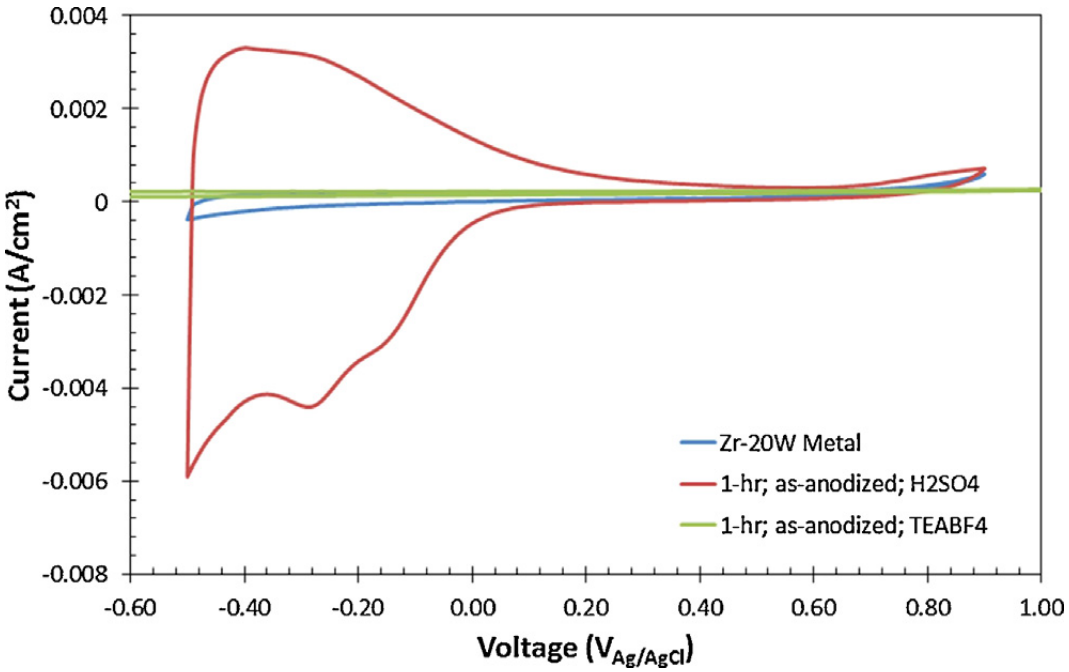

Figure 3.11: Comparison of the results of a cyclic voltammetry (CV) test on the un-anodized Zr–20 W metal with the 1-h as-anodized material at a scan rate of 100 mV/s.

As an additional part of the capacitance tests, the annealed nanotubes were subjected to several cycles of charging and discharging to determine if there was any immediate degradation of material. These tests were performed in a potential that only tested the EDL capacitance and not the pseudocapacitance. From the 100 cycles of the charge/discharge test (CCD), five are displayed in Fig. 3.12. There is very little change between the first and last cycle, and even less between the 60th and 100th cycles. Knowing that there is a constant supplied current of 10 μA, the capacitances for each cycle can be calculated. The change in capacitance between the 60th cycle and the 100th cycle was less than 2%.

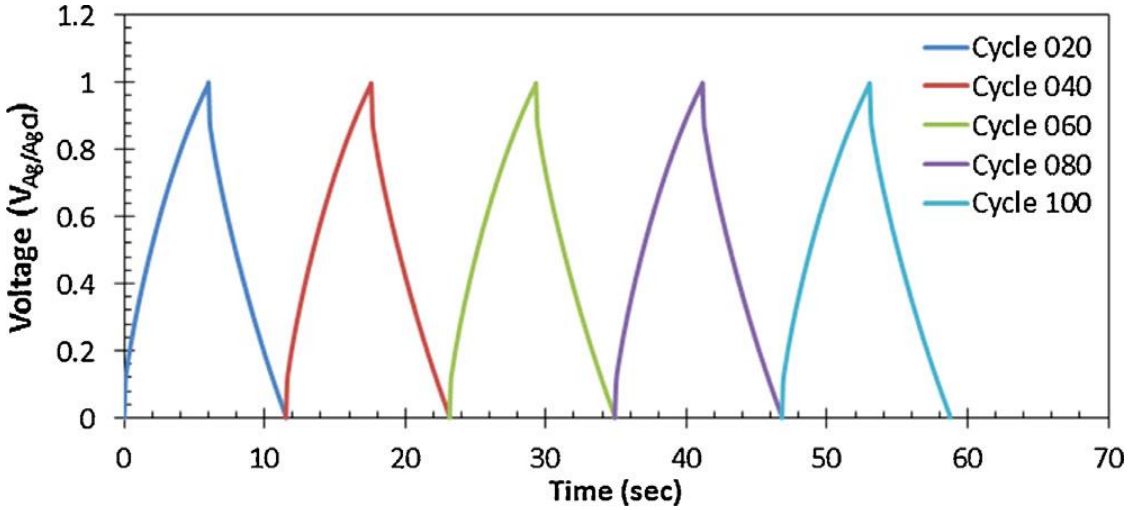

Figure 3.12: Representative cyclic charge–discharge (CCD) results of annealed Zr–W (anodized for 1 h) tested in 1 M H_2SO_4 solution between 0 V and 1.0 V with 10 µA/cm^2 current. The apparatus was constructed as a two-electrode system with the annealed Zr–W as both electrodes. Five different cycles from the 100-cycle test are displayed.

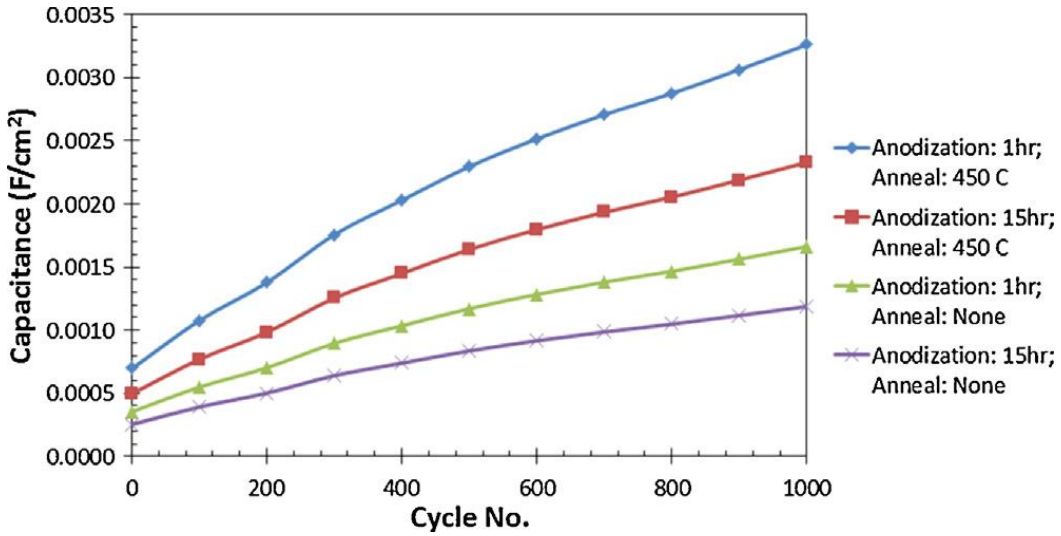

Figure 3.13: Comparison of the change in capacitance of the Zr–W mixed oxide during 1000 cycles of CV testing in 1 M H_2SO_4. Both the annealed and as-anodized samples are shown here.

A secondary test of the mixed oxide layer's ability to withstand cycling was performed by subjecting the samples to 1000 cycles of CV testing at the 1000 mV/s scan rate in the 1 M

H_2SO_4 electrolyte. The organic electrolyte was not used due the poor performance as mentioned above. Fig. 3.13 shows the change in capacitance of the material for every 100th cycle. Interestingly enough, the material showed improved capacitance during and after the tests. Examining with an SEM microscope confirms that this is most likely due to the removal of loosely-adhered "debris-like" re-precipitated hydroxide layer from the surface of the nanoporous oxide layer that would otherwise inhibit transportation of H^+ into the nanostructure of the oxide layer. To get a better idea of how this affected the overall capacitance, we repeated the cyclic charge discharge test on an annealed sample that was cycled 1000 times. Immediately, we noticed that the material could be charged with much higher currents. Fig. 3.14 shows five cycles from this test. It should be noted that the current used here was 1.5 mA, more than 100 times the previous current, and the potential range is a little larger. It is possible to use higher currents to charge and discharge the system, but they result in even greater IR-drops. Still, we believe this improvement in capacitance merits further investigation.

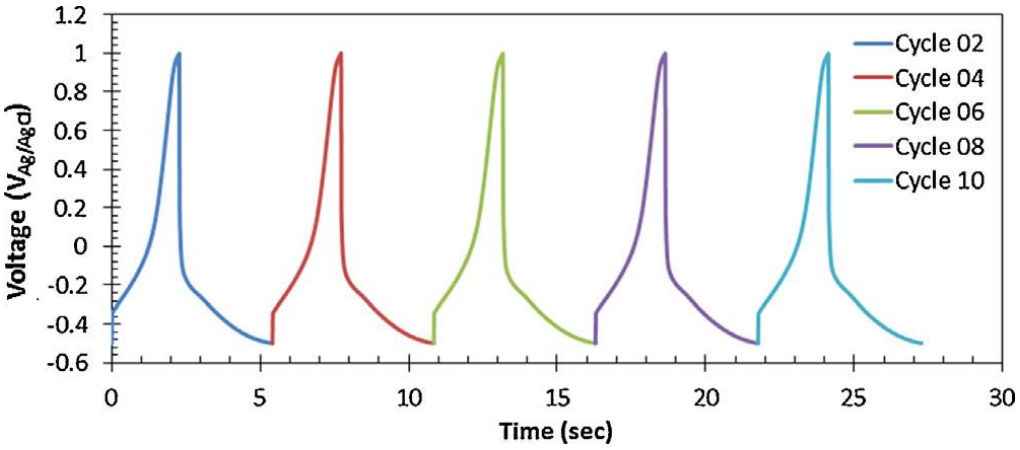

Figure 3.14: Representative cyclic charge–discharge (CCD) results of annealed Zr–W (anodized for 1 h) tested in 1 M H_2SO_4 solution between −0.5 V and 1.0 V with 1.5 mA/cm^2 current. The apparatus was constructed as a three-electrode system with the annealed Zr–W as

the working electrode, platinum as the counter electrode, and Ag/AgCl as the reference electrode. Five cycles of the 10-cycle test are displayed.

The samples were anodized at 40 V in EG-B solution for 1 h and15 h and tested in as-anodized and annealed (450◦C for 2 h) conditions. The sample anodized for 15 h showed oxide nanotubes of almost similar diameter to that in the 1 h-anodized. We were unable to determine the specific surface area of each sample, so instead we attempted to determine the approximate weight of the oxide layer. Anodized coupons were weighed and then the oxide layer was removed via polishing with great care so as not to remove any of the alloy substrate. Then the coupons were weighed again and the difference was determined to be weight of the layer. For the 1-h anodized sample this was about 0.46 mg/cm^2 of substrate, and for the 15-h anodized sample this was about 1.7 mg/cm^2 of substrate.

Fig. 3.15(a) shows the results of CV testing on each of these samples in 1 M H_2SO_4 at a 100 mV/s scan rate. The as-anodized samples demonstrated greater capacitance than the annealed sample. This is most likely caused by the tungsten Faradaic reactions occurring in the as-anodized sample. The 15-h anodized samples showed lower capacitance than the 1-h anodized samples. Additionally, the capacitance decreased with an increase in the scan rate. Even though the 15-h anodized sample had five times longer nanotubes than the 1-h anodized sample, there was still a decrease in the capacitance for a given scan rate. Fig. 3.15(b) shows the same test in1 M $TEABF_4$. Unfortunately, the capacitance is much weaker than that of the samples test in 1 M H_2SO_4. There does not appear to be any Faradaic reactions present in the system.

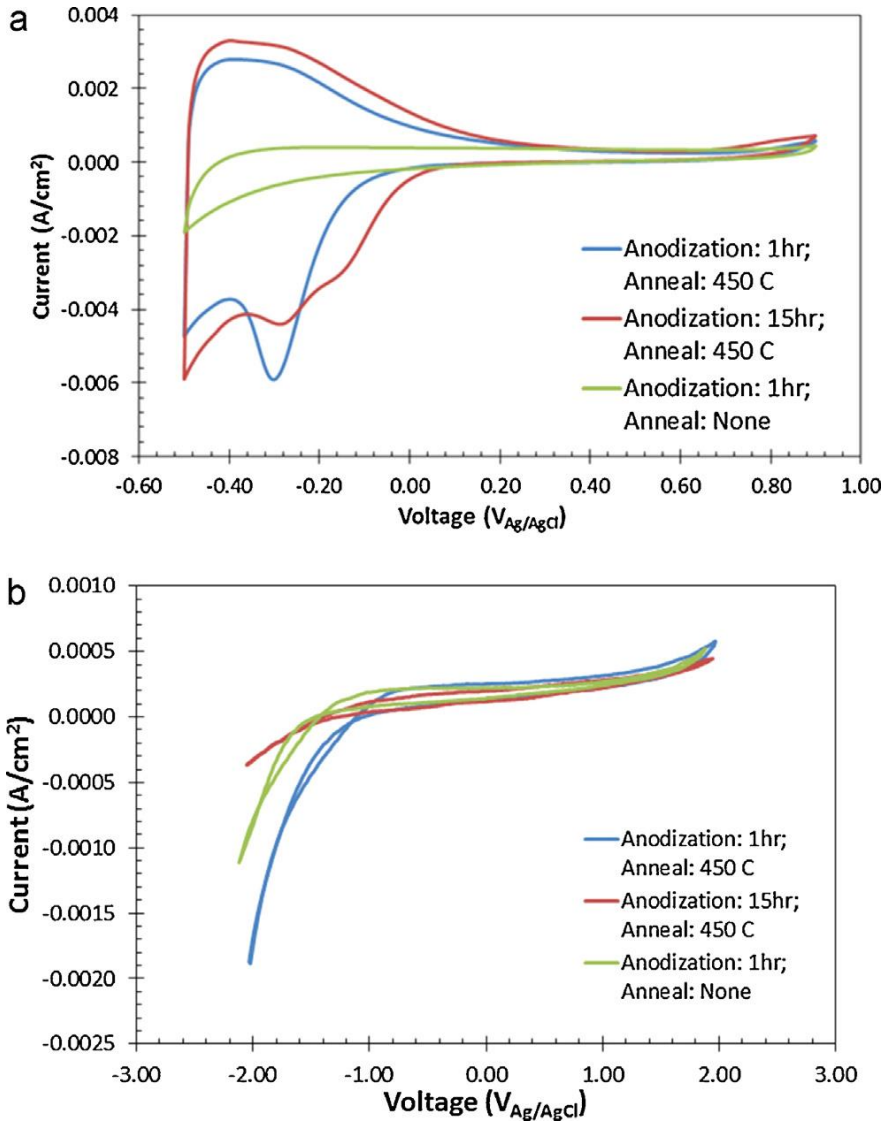

Figure 3.15: Comparison of the results of cyclic voltammetry (CV) test on the as-anodized Zr–W oxide nanotubes (anodized for 1-h and 15-h) and also on the annealed Zr–W oxide nanotubes (anodized for 1-h) tested in (a) 1 M H_2SO_4 and (b) 1 M $TEABF_4$ in acetonitrile solution with a scan rate of 100 mV/s.

The CV plots of the annealed samples (anodized for 1 h) contain contributions from the EDL, space charge layer, and pseudo capacitance. Since the CV was carried out at a constant potential sweep rate, the X-axis of the cyclic voltammogram could be considered as a time scale and the integration of the current over the time divided by the potential range

would give the capacitance, $C = \int_0^{t_1} Idt/\Delta E$. The maximum capacitance recorded for the 1-h anodized sample was 40.03 mF/cm^2 at a scan rate of 10 mV/s and the capacitance of the 15-h anodized sample was about 33.4 mF/cm^2 for the same scan rate. Dividing these values by the weight of the layer per square centimeter, this gives capacitances of ~88 F/g and ~19 F/g, respectively. The minimum recorded capacitance was 1.93 mF/cm^2 (about 4.2 F/g) for the 1-h anodized sample in the annealed condition at 1000 mV/s. This capacitance was comparable to that reported for the ordered, mesoporous WO_3 material [23]. In the case of TiO_2 nanotubes, Salari et al. [20] reported a capacitance of 181 μF/cm^2 at 100 mV/s. For those samples tested in 1 M $TEABF_4$, the highest recorded capacitance was 8.27 mF/cm^2 for the 1-h as-anodized sample at a scan rate of 10 mV/s. The lowest record capacitance was 0.17 mF/cm^2 for the same 1-h as-anodized sample, but at a scan rate of 1000 mV/s. This gives capacitances of ~18 F/g and ~0.4 F/g, respectively. Other measured capacitances are displayed in Table 3.1.

Table 3.1 – Electrochemical capacitance data for Zr-W oxide nanotubes.

Type	Electrolyte	Scan Rate (mV/s)	Capacitance (mF/cm^2)
As-anodized (anodized at 40 V for 1-hr)	1.0 M H_2SO_4	10	40.51
		100	24.39
		1000	14.67
As-anodized (Anodized at 40 V for 15 h)	1.0 M H_2SO_4	10	33.10
		100	19.99
		1000	10.09
Annealed, (anodized at 40 V for 1 h and annealed at 450 C for 2 h in nitrogen)	1.0 M H_2SO_4	10	10.65
		100	5.42
		1000	1.94
As-anodized (anodized at 40 V for 1-hr)	1.0 M $TEABF_4$	10	8.27
		100	0.64
		1000	0.17
As-anodized (Anodized at 40 V for 15 h)	1.0 M $TEABF_4$	10	5.53
		100	1.92
		1000	0.60
Annealed, (anodized at 40 V for 1 h and annealed at 450 C for 2 h in nitrogen)	1.0 M $TEABF_4$	10	8.24
		100	0.90
		1000	0.36

The electrochemical capacitance of Zr–W oxide nanotubes could be attributed to the distribution of highly dielectric h-WO_3 and ZrW_2O_8 phases in the ZrO_2 matrix, presence of a high concentration of oxygen vacancies, and high proton conductivity of the mixed ZrO_2–WO_3 oxide reported in the literature [5]. In order to understand the contribution of charge transport behavior by oxide nanotubes on the capacitance, electrochemical impedance spectroscopic measurements were carried out. Fig. 3.16(a) shows the Bode plots (modulus of impedance as a function of frequency of the AC signal in log–log scale) of the Zr–W oxide nanotubular samples indifferent anodized conditions. The as-anodized samples showed lower impedance than the annealed samples at high frequencies and at low frequencies. At the intermediate frequencies (between 0.2 and 200 Hz), the annealed samples showed lower impedance than the as-anodized samples. The reason for such behavior is not understood at this time and is the subject for further investigation. Fig. 3.16(b) shows the Nyquist plots of the as-anodized and annealed samples. The as-anodized samples showed lower impedance than their annealing counterparts.

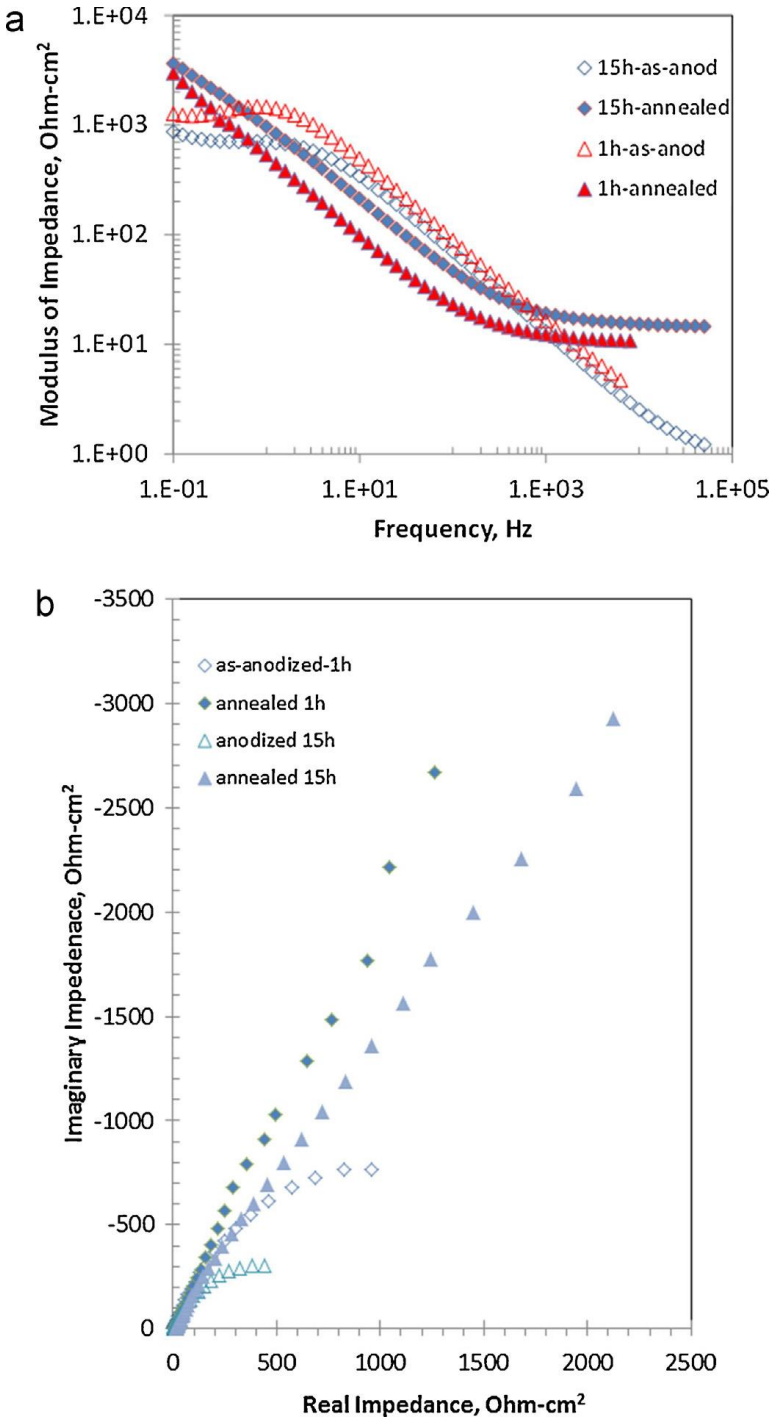

Figure 3.16: Electrochemical impedance of the anodic oxides of Zr–W as a function of frequency tested at an applied dc potential of 0.2 V vs. Ag/AgCl in 1 M H_2SO_4. The samples were in the as-anodized and annealed conditions. (a) Bode plots and (b) Nyquist plots.

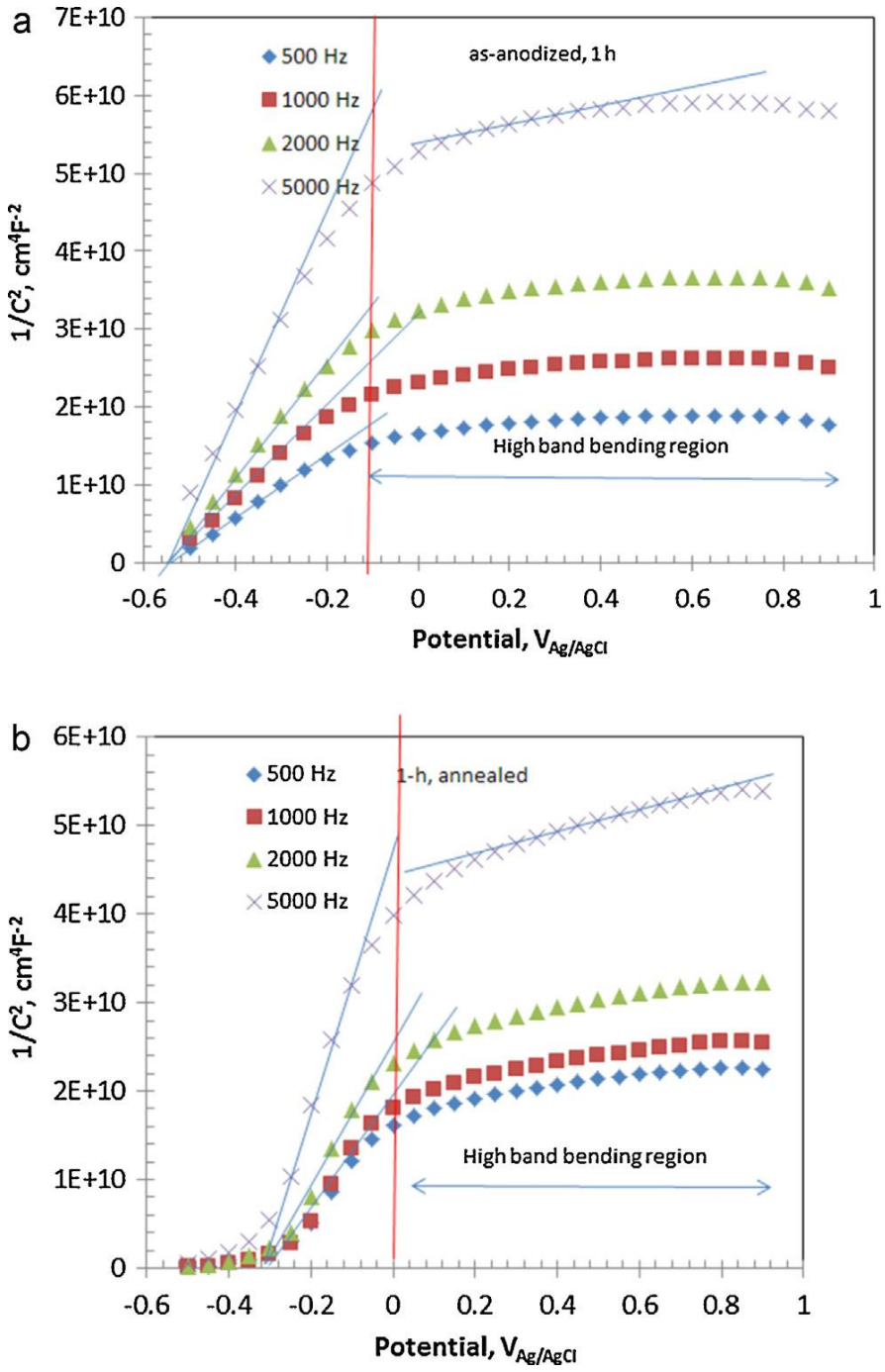

Figure 3.17: Mott–Schottky plots of the anodic oxide of Zr–W in the 1-h (a) as-anodized condition, and (b) annealed condition at several different frequencies. The electrolyte was 1 M H_2SO_4.

Fig. 3.17(a) and (b) shows the Mott–Schottky plots of the samples anodized for 1 h in as-anodized and annealed conditions. The Mott–Schottky relation assumes uniform distribution of the charge carriers in the material of investigation. However, such an assumption may not be valid when multiple phases are present in the Zr–W oxide nanotubes. Therefore, Mott–Schottky measurements were carried out at multiple frequencies from 500 to 5000 Hz. The charge carrier densities of the samples were calculated from the slopes of the Mott–Schottky plots, assuming a lumped dielectric constant of 36. (The dielectric constant of amorphous ZrO_2 is about 22.2 [44], and the dielectric constant of amorphous WO_3 is 90 [45]. Based on their composition by mass in the material, we assumed the lumped dielectric constant of 36.) The positive slope of the Mott–Schottky plot indicated the material to be an n-type semi-conductor. Therefore, the charge carriers could be due to oxygen vacancies. The plots showed two different linear regions. The region at lower potentials, labeled as low band bending region, showed steeper slopes and hence lower charge carrier densities. The region at higher anodic potentials, labeled as high band bending region, showed shallower slopes and therefore higher charge carrier densities. Table 3.2 summarizes the charge carrier densities measured at different frequencies. The samples in the as-anodized conditions showed higher charge carrier densities than the annealed samples. The charge carrier density was observed to increase with the anodization time indicating that more defects were created in the oxide layer by exposing them to the electric field for longer time. Thermal annealing at 450◦C for 2 h was observed to anneal some of the defects as the charge carrier density decreased after annealing. It should be noted that the XPS results indicated increased W^{5+} peaks upon annealing. However, the Mott–Schottky results indicated decreased charge carrier density. Therefore, it can be argued that the distribution of W^{5+} ions occurred only at the surface level and not

across the space charge layer thickness. This observation is supported by the fact that the charge carrier density varied as a function of frequency. The deep lying donor levels are ionized at lower frequencies. Therefore, increase in the frequency decreased the charge carrier density. Furthermore, the dielectric constant, surface roughness, and defect migration are affected by the frequency [46]. The charge carrier density at the low band bending region was lower than that of high band bending case. Similar results were reported for the anodized niobium oxide by La Mantia et al. [46]. The flat band potential was almost similar for all the frequencies in the low band bending region, which was−0.54 $V_{Ag/AgCl}$ for the as-anodized sample and −0.32 $V_{Ag/AgCl}$ for the annealed sample. The positive shift in the flat band potential could be attributed to the higher concentration of W^{5+} ions at the surface and associated positively charged oxygen vacancies at the surface of the annealed samples than that of as-anodized samples. However, the concentration profile of ions inside the space charge layer was different from that of surface. The decrease in the defect density upon annealing could be attributed to the increased impedance of the annealed sample at low frequencies. The lower capacitance of the annealed samples than that of as-anodized samples could be attributed to the lower defect concentration. The individual contributions of the h-WO_3 and ZrW_2O_8 phases in the enhanced charge storage property are being investigated and will be reported in another communication.

TABLE 3.2 – Summary of charge carrier densities measured at different frequencies.

Condition	Charge carrier density in the low band bending region, (cm^{-3})				Charge carrier density in the High band bending region, (cm^{-3})			
	500 Hz	1000 Hz	2000 Hz	5000 Hz	500 Hz	1000 Hz	2000 Hz	5000 Hz
Anodized for 1 h, as-anodized	9.5×10^{19}	7×10^{19}	5.5×10^{19}	3.5×10^{19}	1.4×10^{21}	1.1×10^{21}	8.8×10^{20}	5.8×10^{20}
Anodized for 1 h, and annealed at 450 ^{o}C for 2 h	6.1×10^{19}	5.2×10^{19}	4.5×10^{19}	3.2×10^{19}	7.3×10^{20}	5.8×10^{20}	5.2×10^{20}	3.3×10^{20}
Anodized for 15 h, as-anodized	1.4×10^{20}	1.3×10^{20}	1.2×10^{20}	1.18×10^{20}	2.7×10^{21}	1.2×10^{21}	9.3×10^{20}	6.3×10^{20}
Anodized for 15 h, and annealed at 450 ^{o}C for 2 h	7.2×10^{19}	6.0×10^{19}	5.2×10^{19}	3.7×10^{19}	8.1×10^{20}	6.7×10^{20}	5.8×10^{20}	4.2×10^{20}

4. Conclusions

Zr–20 wt% W alloy substrate was electrochemically anodized in fluoride-containing ethylene glycol solutions to form ordered arrays of oxide nanotubes containing ZrO_2 and WO_3. Anodization at 40 V in ethylene glycol containing 0.2 M NH_4F + 5 vol% water was observed to be an optimal condition for the growth of oxide nanotubes. Thermal annealing of the oxide nanotubes at 450◦C for 2 h in nitrogen atmosphere resulted in the formation of a mixed-oxide phase, ZrW_2O_8. The results of XRD and XPS supported the presence of these phases.

No significant photo-activity of the Zr–W oxide nanotubes could be observed because of the mismatch in the band edge positions of the ZrO_2, WO_3, and ZrW_2O_8 phases. However, the oxide nanotubes showed enhanced capacitance in 1 M H_2SO_4. The highest measured capacitance was 40.03 mF/cm^2 at a scan rate of 10 mV/s for the sample which was anodized at 40 V for 1 h. The lowest capacitance was 1.93 mF/cm^2 at a scan rate of 1 V/s for the sample annealed at 450◦C for 2 h (anodized for 1 h). The enhanced capacitance could be attributed to high concentrations of oxygen vacancies present in the material and to the high proton conductivity reported for the ZrO_2–WO_3 mixed oxide.

5. Acknowledgements

The authors acknowledge the financial support of the Defense Advanced Research Projects Agency (DARPA) through the grant YFA N66001-12-1-4252. The support of Dr. William Casebeer (program manager), and Dr. Judah M Goldwasser (mentor) is gratefully acknowledged.

6. References

[1] H. Tsuchiya, J.M. Macak, A. Ghicov, L. Taveira, P. Schmuki, Self-organized porous TiO2 and ZrO2 produced by anodization, Corros. Sci. 47 (2005) 3324–3335.

[2] D. Fang, K. Huang, Z. Luo, Y. Wang, S. Liua, Q. Zhang, Freestanding ZrO2 nanotube membranes made by anodic oxidation and effect of heat treatment on their morphology and crystalline structure, J. Mater. Chem. 21 (2011) 4989–4994.

[3] S. Berger, H. Tsuchiya, A. Ghicov, P. Schmuki, High photocurrent conversion efficiency in self-organized porous WO3, Appl. Phys. Lett. 88 (2006) 203119.

[4] W. Wei, S. Shaw, K. Lee, P. Schmuki, Rapid anodic formation of high aspect ratio WO3 layers with self-ordered nanochannel geometry and use in photocatalysis, Chem. Eur. J. 18 (2012) 14622–14626.

[5] D. Kowalski, Y. Aoki, H. Habazaki, High proton conductivity in anodic ZrO2/WO3 nanofilms, Angew. Chem. Int. Ed. 48 (2009) 7582–7585.

[6] F. Muratore, A. Baron-Wiechec, T. Hashimoto, A. Gholinia, H. Habazaki, P. Skeldon, G.E. Thompson, Porous anodic film growth on a Zr–W alloy: corrosion, passivation, and anodic films, Electrochem. Solid State Lett. 15 (2012) C8–C11.

[7] S. Abermann, C. Henkel, O. Bethge, G. Pozzovivo, P. Klang, E. Bertagnolli, Stabilization of a very high-k crystalline ZrO2 phase by post deposition annealing of atomic layer deposited ZrO2/La2O3 dielectrics on germanium, Appl. Surf. Sci.256 (2010) 5031–5034.

[8] J.S. da Cruz, M.A. Fraga, S. Braun, L.G. Appel, Thermal spreading of WO3 onto zirconia support, Appl. Surf. Sci. 253 (2007) 3160–3167.

[9] I.M. Szilágyi, B. Fórizs, O. Rosseler, A. Szegedi, P. Németh, P. Király, G. Tárkányi,B. Vajna, K. Varga-Josepovits, K. László, A.L. Tóth, P. Baranyai, M. Leskelä, WO3 photocatalysts influence of structure and composition, J. Catal. 294 (2012)119–127.

[10] I.M. Szilágyi, J. Madarász, G. Pokol, P. Király, G. Tárkányi, S. Saukko, J. Mizsei,A.L. Tóth, A. Szabó, K. Varga-Josepovits, Stability and controlled composition of hexagonal WO3, Chem. Mater. 20 (2008) 4116–4125.

[11] K.M. Ganguly, S. Sarkar, S.N. Bhattacharyya, Zirconium dioxide a new photo-sensitizer under UV irradiation, Chem. Commun. 8 (1993) 682.

[12] C. Wu, X. Zhao, Y. Ren, Y. Yue, W. Hua, Y. Cao, Y. Tang, Z. Gao, Gas-phase photo-oxidations of organic compounds over different forms of zirconia, J. Mol. Catal. A: Chem. 229 (2005) 233–239.

[13] S. Liu, Z. Xiu, J. Pan, X. Cui, W. Yu, J. Yu, Preparation and photocatalytic activities of ZrTiO4 nanocrystals, J. Alloys Compd. 437 (2007) L1–L3.

[14] L. Jiang, Q. Wang, C. Li, J. Yuan, W. Shangguan, ZrW2O8 photocatalyst and its visible-light sensitization via sulfur anion doping for water splitting, Int. J. Hydrogen Energy 35 (2010) 7043–7050.

[15] C. Santato, M. Odziemkowski, M. Ulmann, J. Augustynski, Crystallographically oriented mesoporous WO3 films: synthesis, characterization, and applications, J. Am. Chem. Soc. 123 (2001) 10639–10649.

[16] C. Santato, M. Ulmann, J. Augustynski, Photoelectrochemical properties of nanostructured tungsten trioxide films, J. Phys. Chem. B 105 (2001) 936–940.

[17] S.K. Deb, Opportunities and challenges in science and technology of WO3 for electrochromic and related applications, Sol. Energy Mater. Sol. Cells 92 (2008) 245–258.

[18] D.C. Vermarie, P.C. van Berge, The preparation of WO3/TiO2 and WO3/Al2O3 and characterization by temperature-programmed reduction, J. Catal. 116 (1989) 309.

[19] C. Martin, I. Martin, V. Rives, G. Solana, V. Loddo, L. Palmisano, A. Sclafani, Physicochemical characterization of WO3/ZrO2 and WO3/Nb2O5 catalysts and their photoactivity for 4-nitrophenol photooxidation in aqueous dispersion, J. Mater.Sci. 32 (1997) 6039–6047.

[20] M. Salari, S.H. Aboutalebi, K. Konstantinov, H.K. Liu, A Highly ordered titania nanotube array as a supercapacitor electrode, Phys. Chem. Chem. Phys. 13 (2011) 5038–5041.

[21] Y. Yang, D. Kim, M. Yang, Schmuki, Vertically aligned mixed V2O5–TiO2 nanotube arrays for supercapacitor applications, Chem. Commun. 47 (2011) 7746–7748.

[22] J.H. Kim, K. Zhu, Y. Yan, C.L. Perkins, A.J. Frank, Microstructure and pseudocapacitive properties of electrodes constructed of oriented NiO–TiO2 nanotube arrays, Nano Lett. 10 (2010) 4099–4104.

[23] S. Yoon, E. Kang, J.K. Kim, C.W. Lee, J. Lee, Development of high-performance supercapacitor electrodes using novel ordered mesoporous tungsten oxide materials with high electrical conductivity, Chem. Commun. 47 (2011)1021–1023.

[24] H. Habazaki, S. Koyama, Y. Aoki, N. Sakaguchi, S. Nagata, Enhanced capacitance of composite anodic ZrO2 films comprising high permittivity oxide nanocrystals and highly resistive amorphous oxide matrix, ACS Appl. Mater. Interfaces 3 (2011) 2665–2670.

[25] K.S. Raja, M. Misra, K. Paramguru, Formation of self-ordered nano-tubular structure of anodic oxide layer on titanium, Electrochim. Acta 51 (2005) 154–165.

[26] R. Rangaraju, K.S. Raja, A. Panday, M. Misra, An investigation on room temperature synthesis of vertically oriented arrays of iron oxide nanotubes by anodization of iron, Electrochim. Acta 55 (2010) 785–793.

[27] F. Muratore, A. Baron-Wieche´c, A. Gholinia, T. Hashimoto, P. Skeldon, G.E. Thompson, Comparison of nanotube formation on zirconium in fluoride/glycerol electrolytes at different anodizing potentials, Electrochim. Acta 58 (2011) 389–398.

[28] W. Li, J. Li, X. Wanga, S. Luoa, J. Xiaoa, Q. Chen, Visible light photoelectrochemical responsiveness of self-organized nanoporous WO3 films, Electrochim. Acta 56 (2010) 620–625.

[29] G.E. McGuire, G.K. Schweitzer, T.A. Carlson, Core electron binding energies in some group IIIA, VB, and VIB compounds, Inorg. Chem. 12 (1973) 2450–2453.

[30] T.L. Barr, Recent advances in X-ray photoelectron spectroscopy studies of oxides, J. Vac. Sci. Technol. A 9 (1991) 1793.

[31] M.J. Guittet, J.P. Crocombette, M. Gautier-Soyer, Bonding and XPS chemical shifts in ZrSiO4 versus SiO2 and ZrO2: charge transfer and electrostatic effects, Phys. Rev. B 63 (2001) 125117.

[32] W. Grünert, E.S. Shpiro, R. Feldhaus, K. Anders, G.V. Antoshin, K.M. Minachev, Reduction behavior and metathesis activity of WO3/Al2O3 catalysts: I. An XPS investigation of WO3/Al2O3 catalysts, J. Catal. 107 (1987) 522.

[33] M.A. Cortes-Jacome, C. Angeles-Chavez, X. Bokhimi, J.A. Toledo-Antonio, Generation of WO3–ZrO2 catalysts from solid solutions of tungsten in zirconia, J. Solid State Chem. 179 (2006) 2663–2673.

[34] D.-Y. Cho, S.-J. Oha, Y.J. Chang, T.W. Noh, R. Jung, J.-C. Lee, Role of oxygen vacancy in HfO2/SiO2/Si(1 0 0) interfaces, Appl. Phys. Lett. 88 (2006) 193502.

[35] L. Xu, Z. Wu, W. Zhang, Y. Jin, Q. Yuan, Y. Ma, W. Huang, Oxygen vacancy-induced novel low-temperature water splitting reactions on FeO(1 1 1) monolayer-thick film, J. Phys. Chem. C 116 (2012) 22921–22929.

[36] J. Li, J. Zhu, X. Liu, Synthesis, characterization and enhanced gas sensing performance of WO3 nanotube bundles, New J. Chem. 37 (2013) 4241–4249.

[37] J.K. Kim, K. Shin, S.M. Cho, T.W. Lee, J.H. Park, Synthesis of transparent meso-porous tungsten trioxide films with enhanced photoelectrochemical response: application to unassisted solar water splitting, Energy Environ. Sci. 4 (2011) 1465.

[38] Y. Xu, M.A.A. Schoonen, The absolute energy positions of conduction and valence bands of selected semiconducting minerals, Am. Mineral. 85 (2000) 543–556.

[39] H.J. Yuan, Y.Q. Chen, F. Yu, Y.H. Peng, X.W. He, D. Zhao, D.S. Tang, Hydrothermal synthesis and chromic properties of hexagonal WO3 nanowires, Chin. Phys. B20 (2011) 036103.

[40] L. Ouyang, L.-N. Xu, W.Y. Ching, Electronic structure of cubic and orthorhombic phases of ZrW2O8, Phys. Rev. B 65 (2002) 113110.

[41] E. Deltombe, N. de Zoubov, M. Pourbaix, Section 10.3: tungsten, Atlas Electrochem. Equilib. Aqueous Solutions (1974) 280–285.

[42] K.C. Leonard, W.E. Suyama, M.A. Anderson, Evaluating the electrochemical capacitance of surface-charged nanoparticle oxide coatings, Langmuir 28 (2012) 6476–6484.

[43] B.E. Conway, Transition from supercapacitor to battery behavior in electrochemical energy storage, J. Electrochem. Soc. 138 (1991) 1539–1548.

[44] D. Vanderbilt, X. Zhao, D. Ceresoli, Structural and dielectric properties of crystalline and amorphous ZrO2, Thin Solid Films 486 (2005) 125–128.

[45] A. Mansingh, M. Sayer, J.B. Webb, Electrical conduction in amorphous WO3 films, J. Non-Cryst. Solids 28 (1978) 123–137.

[46] F. La Mantia, H. Habazaki, M. Santamaria, F. Di Quarto, A Critical Assessment of the Mott–Schottky analysis for the characterization of passive film-electrolyte junctions, Russ. J. Electrochem. 46 (2010) 1306–1322.

CHAPTER 4

Effect of Morphology of ZrO_2-WO_3 Mixed Oxide on Electrochemical Energy Storage

S. R. Whitman, K. S. Raja

This chapter forms the basis for an manuscript that will be submitted to the Journal of Power Sources. It is very likely that by that time the manuscript will have undergone several rewrites.

Abstract

ZrO_2-WO_3 mixed oxide is created via an anodization method and considered for application in electrochemical capacitors. Different anodization potentials, annealing temperatures, electrolytes, and other preparation conditions are examined to determine optimum capacitance. We report different nanostructures for the material. The anodized oxides contained different phases of ZrO_2, WO_3, and ZrW_2O_8. Values as high as 60 mF/cm^2 of anodized substrate are reported for the capacitance of the material in 1M H_2SO_4. The presence of ZrW_2O_8 improved the stability of the mixed oxide during extended cycling periods. Large concentrations of charge defects (on the order of 10^{21} cm^{-3}) were also reported for this material. The mixed oxide demonstrated significant power density and energy density to merit further ultracapacitor testing.

1. Introduction

Electrochemical ultracapacitors have capacitance in the order of several mF/cm^2 but store and deliver charge in the time scale of a few seconds. These capacitors are different from the conventional dielectric capacitors that operate in pulse mode and the pulse width is on the nanosecond scale [1]. Electrochemical capacitors store energy through double layer interfacial capacitance, reduction-oxidation reaction based pseudo capacitance, and space charge layer capacitance because of the accumulation of charges during band bending in the case of semiconductor-based electrodes. Carbon has been the most widely used electrode material for

ultracapacitors in the form of carbon foam, paste electrodes, pyrolysis of carbon based polymers, carbon nanotubes, and graphene. Carbon based materials are also used in combination with oxides of Ru, Rh, Pd, Os, Ir, Co, Ni, Mn, Pt, and Fe resulting in 'asymmetric' type capacitors. Pseudocapacitance based capacitors use both planar and porous electrode systems. Hydrated ruthenium oxide is considered as a superior material for ultracapacitor application with a capacitance of 720 F/g [2]. Even though $RuO_2 \bullet xH_2O$ shows very high capacitance, the high cost and limited availability restricts its commercial usage. Manganese oxide has been investigated in neutral electrolytes as potential ultracapacitor material that showed a capacitance of 250 F/g under optimized conditions [3]. Cadmium oxide has been shown to have a capacitance of only 0.35 F/g in K OH electrolyte [4]. Other oxide materials such as NiO, Ti-V-W oxides, and nitrides of V, Nb, Mo, and W have been investigated as ultracapacitor materials [5]. Since sulfuric acid is widely used as electrolyte for electrochemical capacitors, stability against sulfuric corrosion is a main consideration for selection of capacitor material. To overcome the corrosion problem, other electrolytes based on KCl, Na_2SO_4, and other neutral or organic solutions have been investigated. In order to increase the operating potential range of the capacitors and therefore the energy density organic based electrolytes are investigated.

Recently titanium dioxide based materials in combination with other oxides such as NiO have been investigated [6, 7, 8]. Furthermore, asymmetric or hybrid configurations of ultracapacitors with TiO_2 nanomaterial as anode and carbon nanotube electrode as cathode have been reported [9]. Composite electrode of NiO loaded TiO_2 nanotubes showed a maximum specific capacitance of 550 F/g. In this case, the TiO_2 nanotubes acted as support for NiO nanostructures. Even though higher capacitance was reported, stability of the electrode and lifetime of the electrode will be a problem because of the interfacial resistance between the TiO_2

and NiO. The ordered-oxide nanotubular arrays synthesized by the anodization route facilitate faster kinetics of charge/discharge processes that result in high power density. Recently Habazaki et al. [10] demonstrated that enhanced capacitance of anodic ZrO_2 film could be achieved by stabilizing the high permittivity, tetragonal phase in a highly resistive amorphous phase, when tested as a solid state capacitor. WO_3 has been considered to have dispersed but large dielectric constant as a function of frequency. Therefore, it is envisaged that very high charge storage capacity could be observed in the ZrO_2 oxide nanotubes by incorporating WO_3.

2. Experimental

2.1: Mixed-Oxide Preparation

Starting with a 2-mm thick, flat plate containing 20wt% W and 80wt% Zr, 1 x 1.5 cm^2 coupons were cut from the plate. The cut samples were wet-polished down to an 800 grit surface finish and one side of the metal was covered with polyester splicing silicone tape. About 1 cm^2 of the alloy was exposed to 200 mL of solution composed of 3.8 vol% water, 0.25 M NH_4F, and the remainder was ethylene glycol. The taped alloy was used as the positive electrode and, along with a 7.5 cm^2 Ti flag acting as the negative electrode it was subjected to anodization potentials of either 40 V or 60 V.

As part of the tests to improve the capacitance of the material, some of the samples were exposed to 1 M H2SO4 and cycled one thousand times between potentials of -0.5 V and +0.9 V at a rate of 1 V/s. Both cycled and un-cycled samples were annealed in a tube furnace with a constantly-flowing, commercial purity nitrogen stream. Using a constant temperature ramp of 5^oC/min, different target temperatures were reached and held steady for 2 h before cooling. The different annealing temperatures were: 350^oC, 450^oC, 550^oC, and 650^oC.

2.2: Morphological Characterization

The samples' surface morphology was characterized using electron microscopy (FESEM: LEO SUPRA 35VP, TEM: JEOL 2010). Structural characterization of the nanoporous anodic oxide layer was performed by grazing-angle XRD on a PANalytical X'Pert Pro MRD diffractometer equipped with a Copper x-ray tube and parallel-beam optics. The incident angle was fixed at 0.9°. X-ray photo electron spectroscopy (PHI Quantum 2000) was employed to evaluate the surface valence states and electron density of states at the surface of the samples. Mono-chromated Al-Kα (1488.6 eV) radiation was used as the source with an acceptance angle of ±23° and take-off angle of 45°. Charge correction was carried out by considering the C 1s peak at 284.8 eV.

2.3: Electrochemical Characterization

To characterize the electrochemical behavior of the mixed oxide, several tests were performed in different electrolytes. They were carried out using a three-electrode setup where the mixed oxide acted as the working electrode. A 7.5 cm^2 Pt flag acted as the counter electrode in the setup. A Luggin probe containing a AgCl-coated silver wire immersed in saturated KCl solution. ($V_{Ag/AgCl} \approx 0.23\ V_{SHE}$) A Gamry Instruments Model: Interface 1000 was the potentiostat used to collect data in this experiment.

Cyclic voltammetry (CV) was performed using three different scan rates: 10 mV/s, 100 mV/s, and 1000 mV/s. The potential range used for the samples was different depending on the electrolyte using during testing. Two aqueous electrolytes (1 M H_2SO_4 and 1 M LiCl) and one organic electrolyte (1 M $TEABF_4$ dissolved in acetonitrile) were used in this experiment. For 1 M H_2SO_4, the potential range was -0.5 $V_{Ag/AgCl}$ to +0.9 $V_{Ag/AgCl}$. For 1 M LiCl, the potential range was -0.8 $V_{Ag/AgCl}$ to +0.6 $V_{Ag/AgCl}$. For 1 M $TEABF_4$, the potential range was -2.0 $V_{Ag/AgCl}$

to +2.0 $V_{Ag/AgCl}$. Electrochemical impedance spectroscopy (EIS) was also performed in these electrolytes. Using a constant potential of 0.2 $V_{Ag/AgCl}$, measurements were taken over a range of frequencies from 100000 Hz to 0.1 Hz. Next, Mott-Schottky analyses were performed in the same electrolytes using the same potential range that was used in the CV tests. They were also performed at several different frequencies (usually 500, 1000, 2000, and 5000 Hz).

As a final test, the samples were charged up to a voltage specific to the electrolyte at a constant current and then discharged down to a different voltage with the same constant current. This process was repeated for 10 cycles. For 1 M H_2SO_4, the potential range was -0.4 $V_{Ag/AgCl}$ to +1.0 $V_{Ag/AgCl}$. For 1 M LiCl, the potential range was -1 $V_{Ag/AgCl}$ to +0.5 $V_{Ag/AgCl}$. For 1 M $TEABF_4$, the potential range was -2.0 $V_{Ag/AgCl}$ to +2.0 $V_{Ag/AgCl}$. This was mostly used to determine the maximum current the different samples were capable of handling and to see if cycling the mixed oxide 1000 times really did improve the capacitance of the material.

3. Results and Discussion

3.1: Oxide Structure: Anodization Potential and Annealing Effects

The TEM micrographs below display two distinct nanostructures for the different anodization potentials. The sample that was anodized at 40 V shows a nanotubular structure and is shown in Figure 4.1(a). A sample anodized at 60 V is shown in Figure 4.1(b) and it shows a nanoporous structure. The nanotubular array in Fig. 4.1(a) is very disordered. This high degree of disorder makes it very difficult to find images of the tubes from a lateral angle, especially considering the tube walls seem to merge with each other rather than be separate objects. For example, the SEM image in Fig. 4.2 shows a non-annealed sample that was anodized at 40 V and

cycled one thousand times in sulfuric acid. Several collapsed arrays of tubes dot the surface with those pyramid shapes.

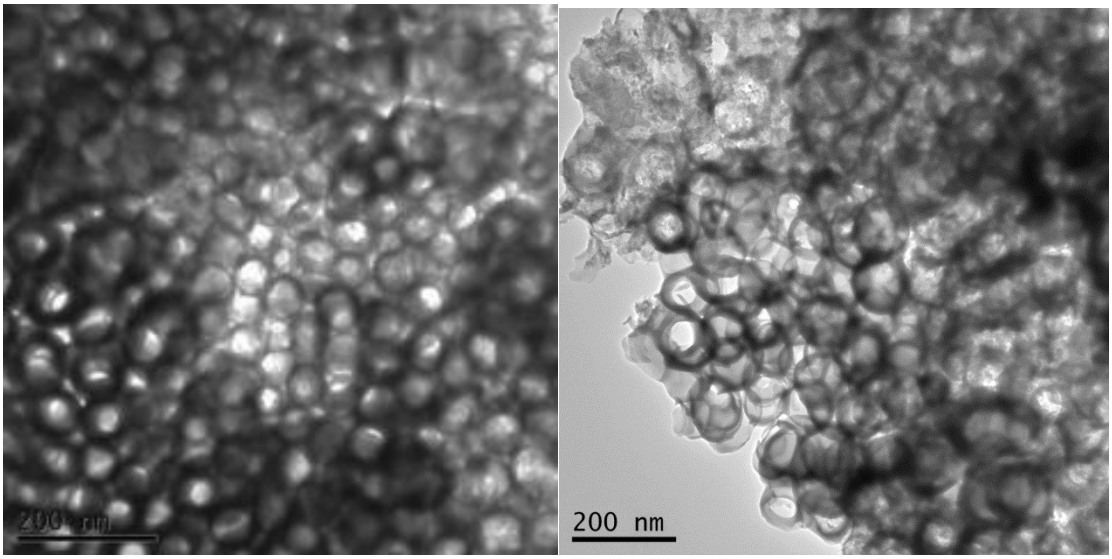

Figure 4.1: TEM images of ZrO_2-WO_3 mixed oxide nanostructure. (a) the samples anodized at 40V created nanotubes, (b) the samples anodized at 60V created nanopores.

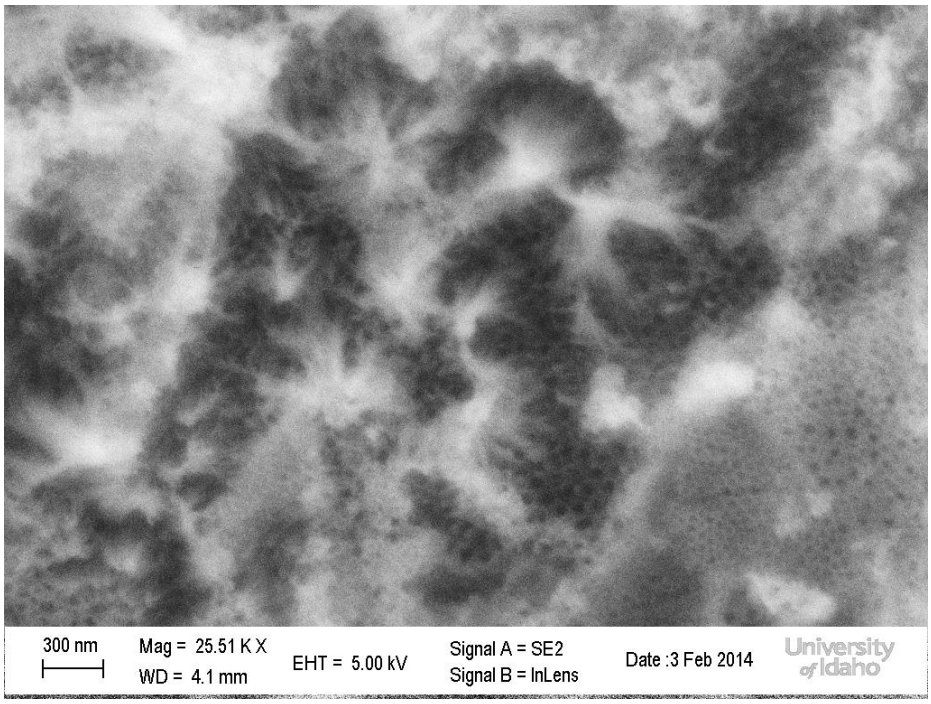

Figure 4.2: SEM image of ZrO_2-WO_3 mixed oxide nanotubes which were formed with an anodization potential of 40 V and then cycled 1000 times in 1 M H_2SO_4

For the metal samples anodized at 60 V, a more nanoporous structure develops on the surface. Figure 4.3 shows a common example of the surface of the 60 V samples. This material shows a large degree of disorder, much like the 40 V samples. It would certainly make sense if the cause of disorder in the 40 V samples was enhanced by the higher anodization potential and, essentially, broke down the walls between the tubes. It may be difficult to notice the difference between the two structures in Figures 4.2 and 4.3 from these pictures, but an easy sign to look for is the overlapping of circles in the image displaying the nanopores. In Figure 4.2, the circles representing the top of the nanotubes are much more rigidly defined.

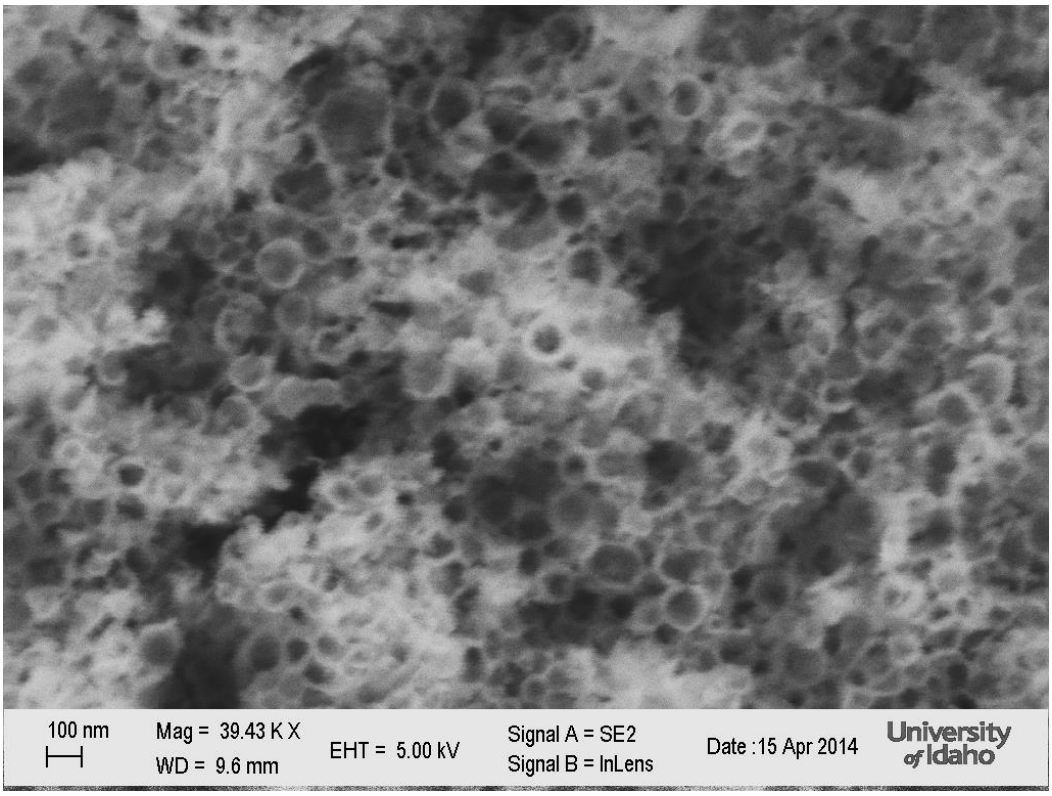

Figure 4.3: SEM image of ZrO_2-WO_3 mixed oxide nanotubes which were formed with an anodization potential of 60 V

These structures are generally consistent throughout the material, but they don't always maintain their forms after the annealing process. In the oxide layer anodized at 40 V, the

nanotubes are already in a high state of disarray. After annealing, a process which usually reduces energy due to internal stresses via mass transport, it would make sense that they would transform to a more nanoporous structure. Indeed, some SEM images demonstrate that exactly (Figure 4.4(a)). However, beneath the immediate surface the tubes still seem to be intact, but they do shatter and break along the face of the tube. The TEM image in Figure 4.4(b) shows some tubes that were part of an array, but began breaking apart during annealing. These images are of those tubes annealed at 450^{o}C. At 650^{o}C, the effect is even more noticeable. Figure 4.5 shows a sample that was anodized at 40 V then annealed at 650^{o}C and the picture bears a strong resemblance to the nanoporous structure in Figure 4.3.

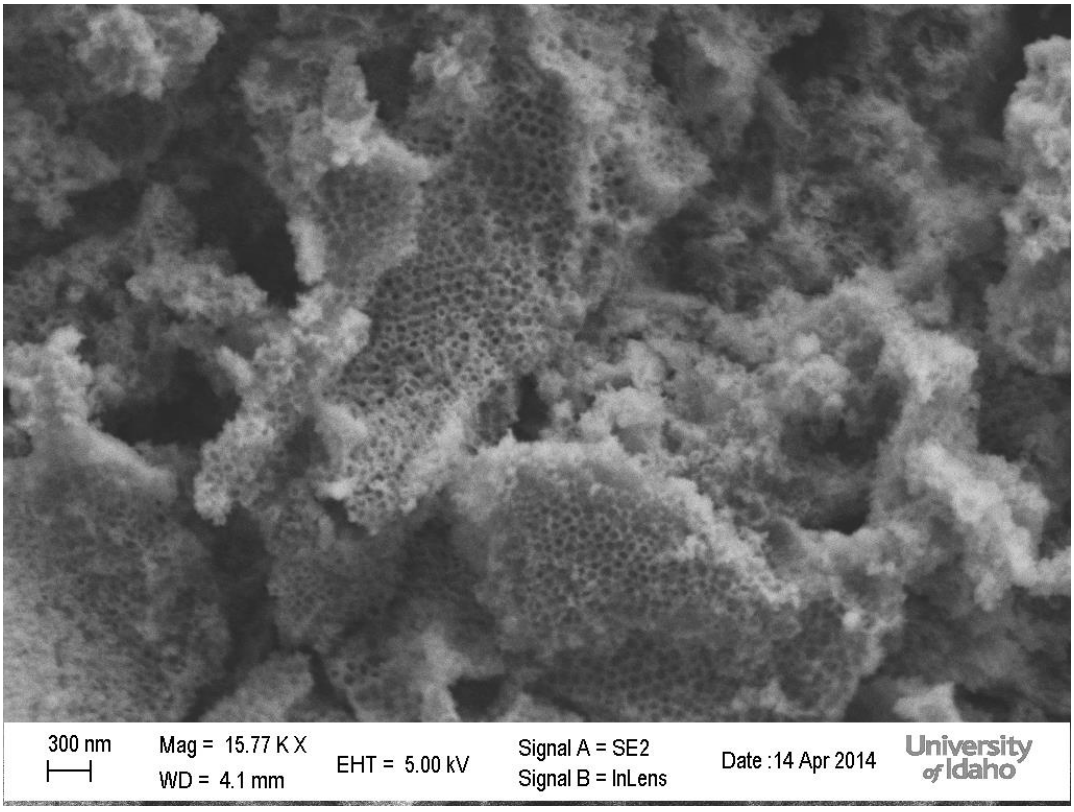

Figure 4.4(a): SEM image of ZrO_2-WO_3 mixed oxide structure formed by anodization at 40 V and then annealed at 450^{o}C

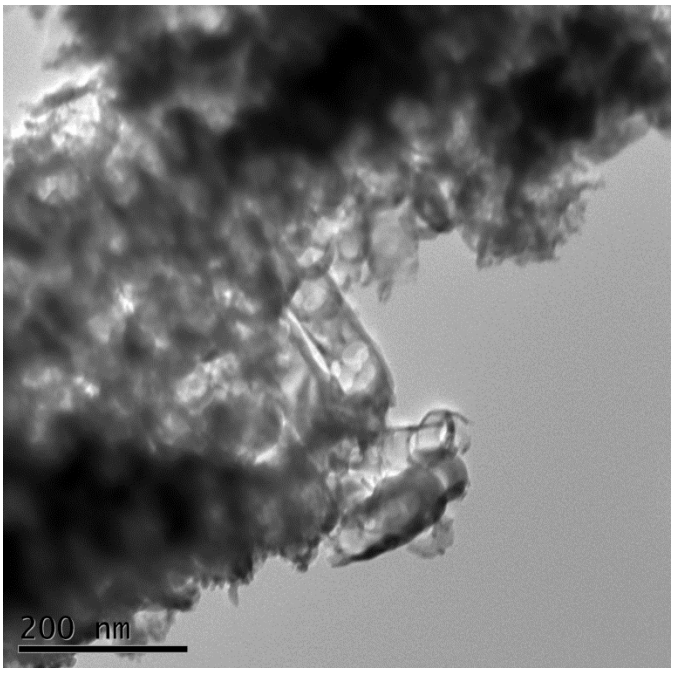

Figure 4.4(b): TEM image of ZrO_2-WO_3 mixed oxide nanotubes formed by anodized at 40 V then annealed at 450^{o}C

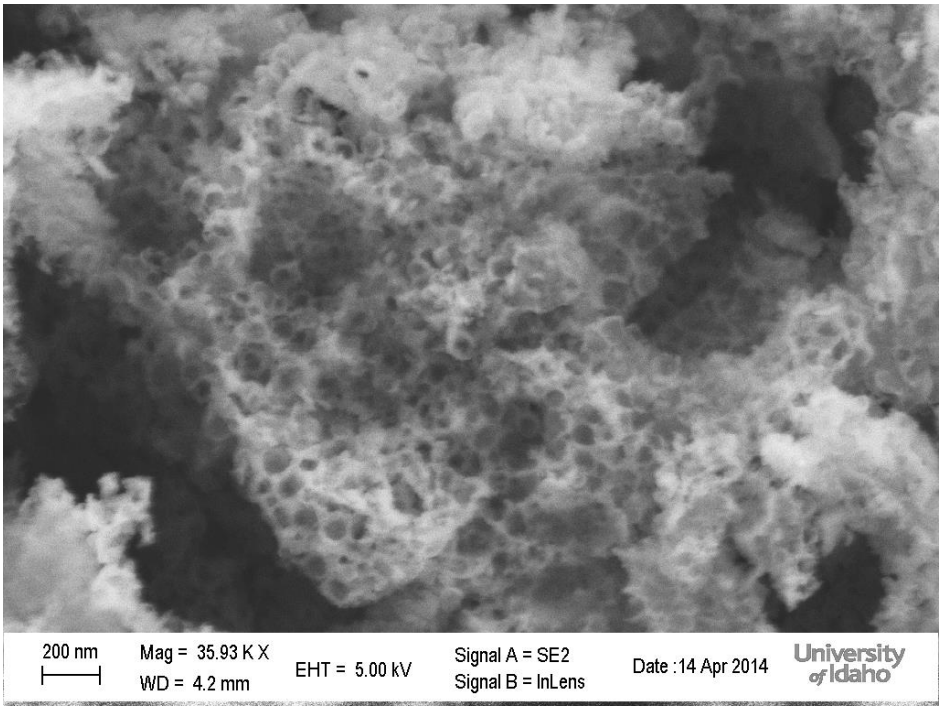

Figure 4.5: SEM image of ZrO_2-WO_3 mixed oxide nanostructure formed by anodization at 40 V then annealed at 650^{o}C

For the samples anodized at 60 V, there doesn't seem to be much change in the microstructure of the oxide layer. Since it is already nanoporous, perhaps it can't change any further. The nanopores from a sample annealed at 650^{o}C (Figure 4.6) don't appear very different from those in Figure 4.3. Ultimately, it seems that longer annealing time would likely cause a greater amount of nanotubular mixed-oxide to convert to nanoporous mixed oxide.

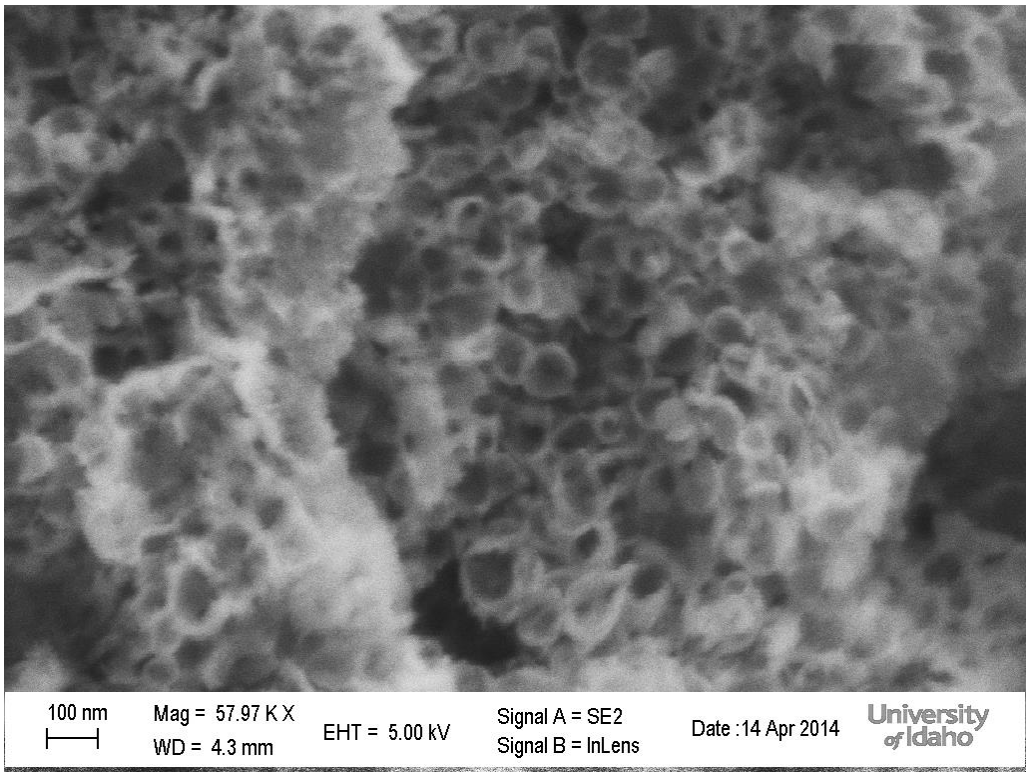

Figure 4.6: SEM image of ZrO_2-WO_3 mixed oxide nanostructure formed by anodization at 60 V then annealed at 650^{o}C

3.2: Oxide Structure: XRD and Binding Energy Analysis

Several notable phases were found on the surface of a sample (annealed at 450^{o}C for 2 h) that was analyzed using glancing angle XRD. The spectra shown in Figure 4.2 denote the presence of hexagonal WO_3, tetragonal ZrW_2O_8, and monoclinic and orthorhombic ZrO_2. The peaks labeled "Zr-W" are just from the metal substrate and are not relevant to this investigation. In the past, anodic oxide of pure Zr and pure W were reported as amorphous [11, 12] and only

after annealing did they transform to crystalline phases. It's the same for the monoclinic transformation for both WO_3 and ZrO_2.

In this sample, WO_3 was most commonly found in its hexagonal form which is well documented as a metastable phase. At room temperature, monoclinic WO_3 is the stable phase. It contains WO_6 octahedra connected at the corners in a chessboard-like arrangement [13]. The octahedra in h-WO_3 are connected in a ring-shaped structure that, in significant amounts, resembles a tunnel [14]. Incorporating cations like Na^+ or NH_4^+ or introducing oxygen vacancies that distort the lattice may serve a role in stabilizing the hexagonal phase [13]. The presence of NH_4^+ ions in this sample is likely due to the ammonium fluoride in the anodization solution and because of the high potential at which the sample was anodized, a high concentration of oxygen vacancies could be stabilizing the WO_3 phase in the as-anodized sample.

A rough estimate of the volume fraction of the phases in both as-anodized and annealed oxide can be made by integrating the intensities of the major peaks of the XRD spectra in Figure 4.7. There is a clear reduction in h-WO_3 after annealing. There are also increases in o-ZrO_2 and t-ZrW_2O_8 phases. The tunnel-like structure of h-WO_3 [15] and the relevance of the decrease of that phase after annealing will be discussed in section containing cyclic voltammetry data.

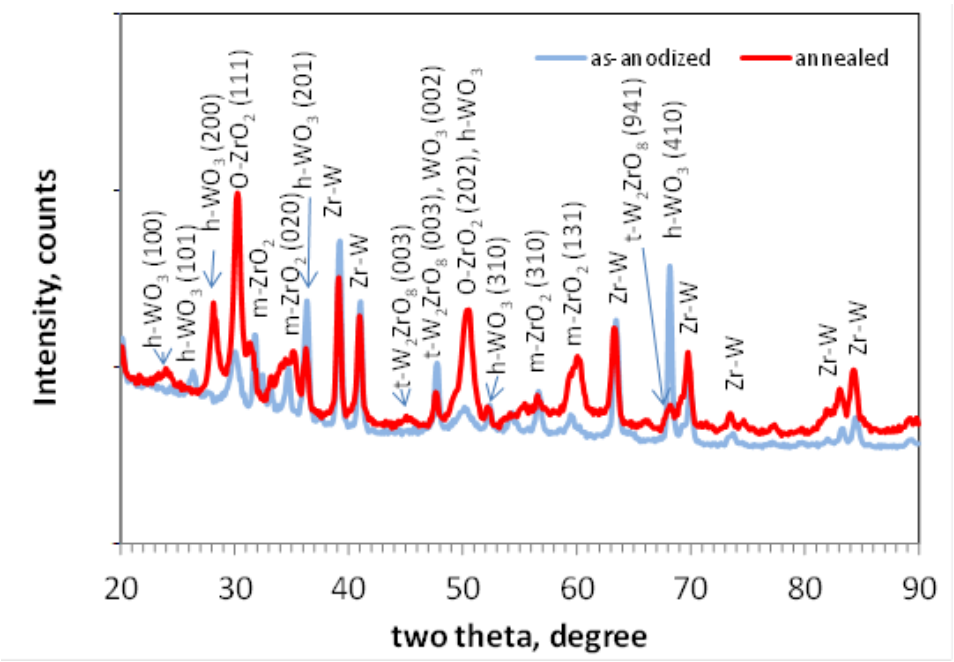

Figure 4.7: XRD spectrum of ZrO_2-WO_3 mixed oxide in a sample only anodized at 40V and a sample anodized at 450^{o}C.

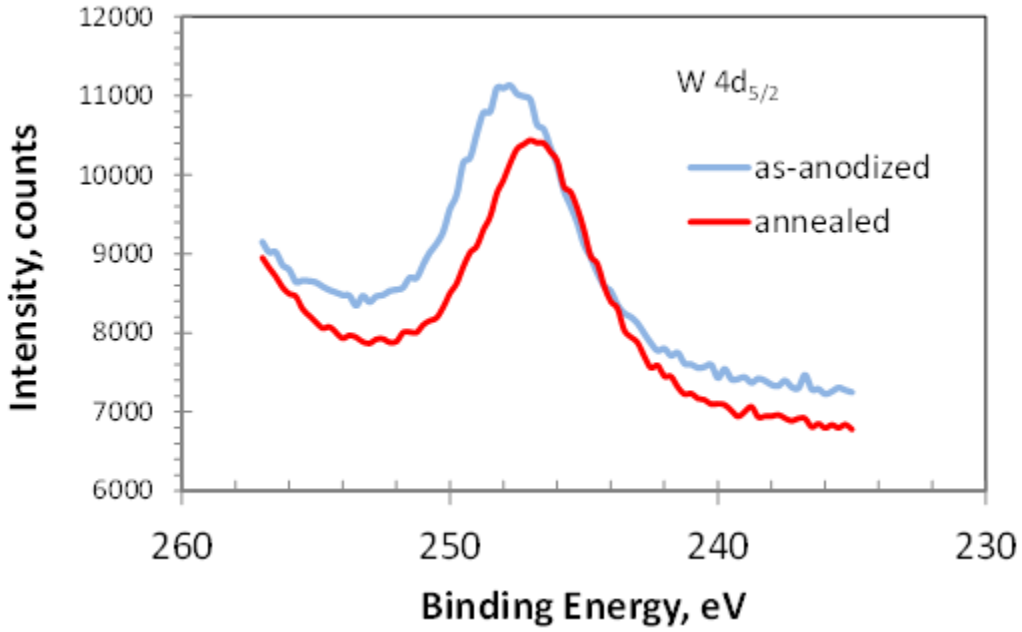

Figure 4.8(a): High resolution X-ray photo electron spectra of anodic oxide of Zr-W alloy prepared by anodization in EG electrolyte containing 0.2 M NH_4F + 5 vol% H_2O at 40 V for 1 h. (a) W-4d spectrum;

High resolution XPS spectra for W $4d_{5/2}$ for the as-anodized and annealed Zr-W mixed oxide sample are shown in Figure 4.8(a). The peak binding energies occurred at 248.25 and 247.25 eV for the as-anodized and annealed conditions, respectively. The binding energy of the anodized sample was similar to the literature reported value for the W $4d_{5/2}$ peak from WO_3 sample [16]. The formation of ZrW_2O_8 during the annealing process may increase the covalency of tungsten, thus lowering the binding energy of W $4d_{5/2}$. This notion is by Barr's [17] proposal that when a complex mixed oxide forms by the mixing of two oxides, the cation of the predominantly ionic oxide becomes even more ionic and the cation of the covalent oxide should experience an increase in its covalency.

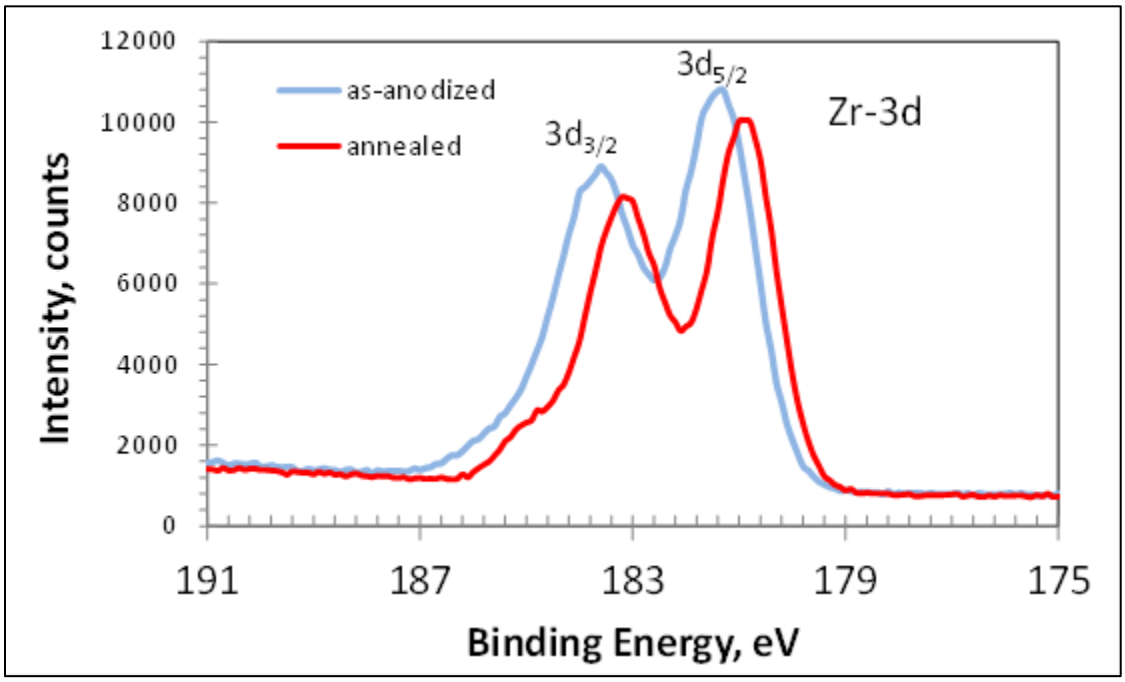

Figure 4.9(a): High resolution X-ray photo electron spectra of anodic oxide of Zr-W alloy prepared by anodization in EG electrolyte containing 0.2 M NH_4F + 5 vol% H_2O at 40 V for 1 h. (a) Zr-3d spectrum;

A similar explanation can be made for the Zr $3d_{5/2}$ peak shown in Figure 4.9(a). By the ab-initio modeling and XPS measurements, Guittet et al.[18] showed that the Zr $3d_{5/2}$ peak of

$ZrSiO_4$ shifted to a higher binding energy than that of ZrO_2 and the Si-2p peak of $ZrSiO_4$ shifted to a lower binding energy than that of SiO_2. In ZrW_2O_8, Zr is more ionic and W is more covalent. Thus the shifts in binding energy of W $4d_{5/2}$ and Zr $3d_{5/2}$ after annealing could be the result of h-WO_3 and ZrO_2 converting to ZrW_2O_8. The spin-orbital interaction of Zr-3d resulted in splitting of $3d_{5/2}$ and $3d_{3/2}$ by 2.3 eV and the peaks were at 181.0 and 183.3 eV, respectively, for the as-anodized sample as seen in Figure 4.9(a). The binding energy increased by 0.5 eV for the annealing condition as the ionic contribution increased for the Zr^{4+} in the mixed oxide phase. The energy shifts displayed in Figures 4.8(a) and 4.9(a) support the formation of this mixed oxide.

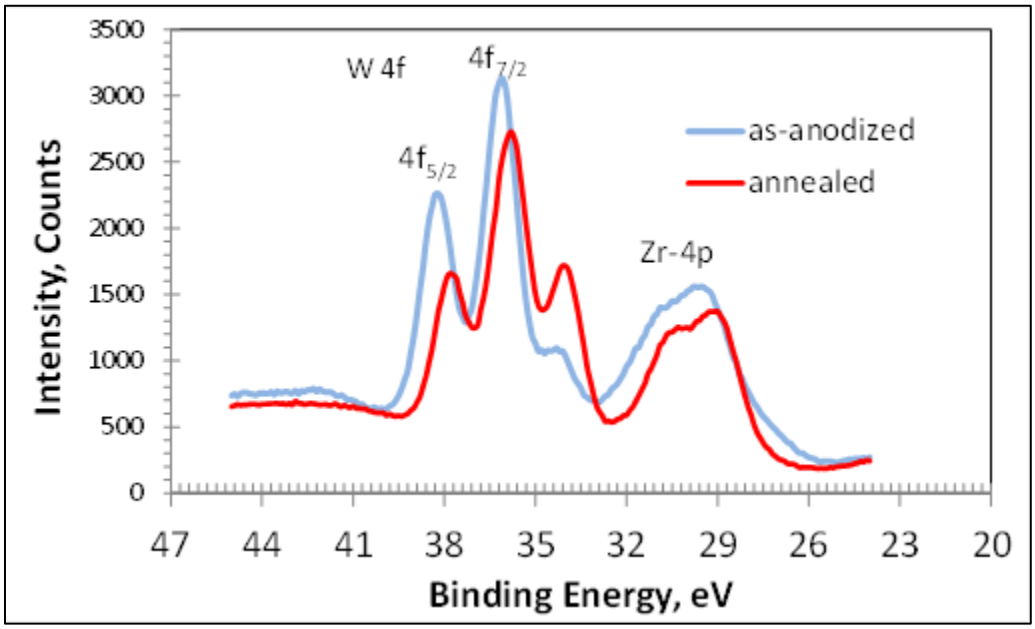

Figure 4.8(b): High resolution X-ray photo electron spectra of anodic oxide of Zr-W alloy prepared by anodization in EG electrolyte containing 0.2 M NH_4F + 5 vol% H_2O at 40 V for 1 h. (b) W-4f and Zr-4p spectrum

From Figure 4.8(b), no significant shift in the binding energy of the Zr-4p peaks was noticed. The spin-orbit splitting of W-4f of the as-anodized sample occurred at 36.2 and 38.2 eV as W-$4f_{7/2}$ and W-$4f_{5/2}$ peaks respectively. This corresponds to a W^{6+} oxidation state [19]. Lower valence W cations, such as W^{5+} and W^{4+}, are necessary for charge neutrality when there is a

large concentration of oxygen vacancies, such as those formed during anodization. The shoulder at 34.5 eV was larger for the annealed sample than for the as-anodized sample which is indicative of a higher concentration of W^{5+}. During the annealing process, NH_4^+ ions that were incorporated in the structure from the anodization step may have been removed causing the creation of a reducing atmosphere in the oxide layer. This resulted in the conversion of some W^{6+} ions into W^{5+} ions and is likely responsible for the drop in the intensity of the W-4f peaks associated with W^{6+}. Similar observations have been reported by other investigators [20].

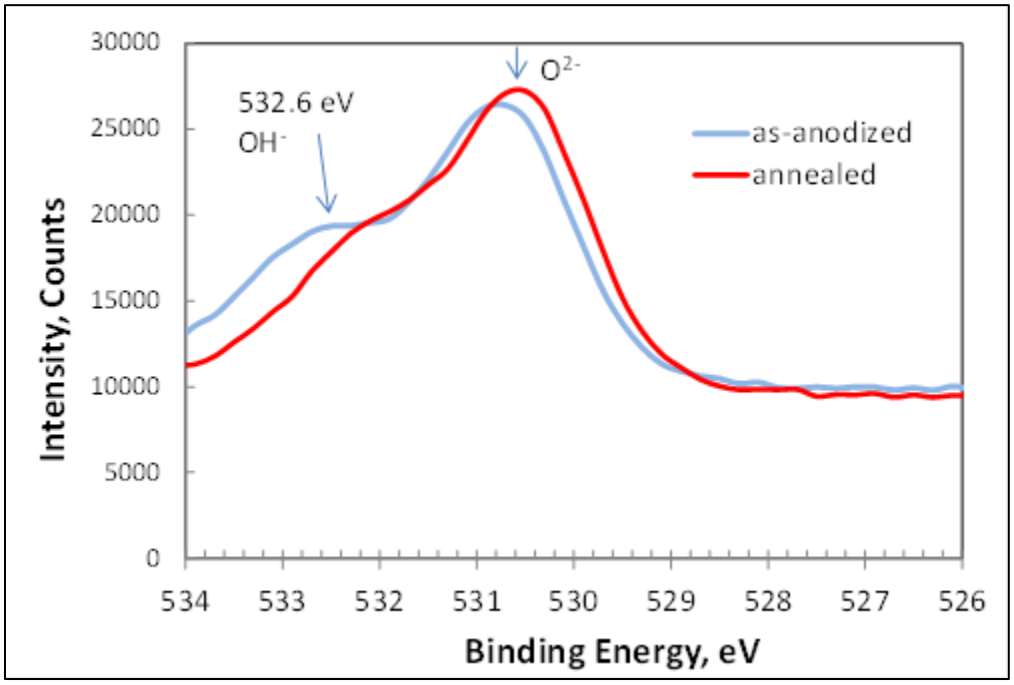

Figure 4.9(b): High resolution X-ray photo electron spectra of anodic oxide of Zr-W alloy prepared by anodization in EG electrolyte containing 0.2 M NH_4F + 5 vol% H_2O at 40 V for 1 h. (b) O-1s spectrum;

Figure 4.9(b) shows the XPS spectra for the oxygen involved in the complex mixed oxide system before and after annealing. The peaks at 530.7 and 530.9 eV are associated with the O^{2-} sub-lattice. The intensity counts recorded at binding energies greater than 531.9 eV could be attributed to the presence of oxygen deficient regions and chemisorbed oxygen or hydroxyl ions

[21, 22]. Considering the much broader shoulder in the as-anodized spectrum, Fig. 4.9(b) seems to indicate a greater presence of oxygen vacancies in the as-anodized samples than in the annealed samples. Additional corroboration with EIS data will be presented in the following section.

It should be noted that the annealed sample showed a larger W-4f shoulder peak in Figure 4.8(b) than the as-anodized sample. This is associated with W^{5+} ions. However, the smaller shoulder width for O-1s annealed sample would seemingly lead to a conflicting idea of oxygen vacancy concentration in the system given the assumption that charge neutrality determines the presence of W^{5+} ions in the oxide. During annealing, it's possible that the binding energy of O-1s was shifted to a lower value. Meanwhile, strong W=O bond form and the shoulder observed at 531.3 eV in Figure 4.8(b) could be attributed to the O^{2-} ions in the oxygen deficient regions [23]. Also, the difference in the O 1s spectra of as-anodized and annealed samples could be attributed to the decrease in the h-WO_3 phase content upon annealing.

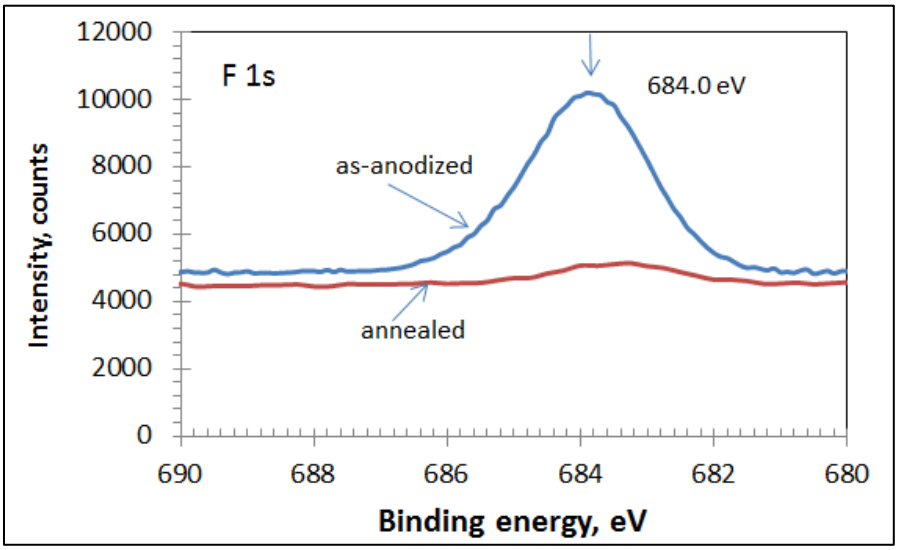

Figure 4.9(c): High resolution X-ray photo electron spectra of anodic oxide of Zr-W alloy prepared by anodization in EG electrolyte containing 0.2 M NH_4F + 5 vol% H_2O at 40 V for 1 h. (c) F-1s spectrum

During the anodization process fluorine from the NH4F-containing solution was incorporated into the mixed oxide layer. Figure 4.9(c) shows the F-1s spectra of the samples before and after annealing. Along with other carbonaceous species, annealing removed so much of the fluoride species that its presence was decreased by an order of magnitude. Similar results were reported by other researchers for the anodization of pure Zr [11] and Zr-W alloy [24].

3.3: Effect of Cycling on Oxide

One goal of this experiment was to use different preparation methods to improve the overall capacitance of the mixed oxide layer. At the beginning, even different electrolytes were tested. Other improvement steps were also attempted but the action that yielded the best results was repeated cycling of the material. During an early set of electrochemical tests, we performed a series of tests meant to show that this material had good stability during cycling in acidic solutions. This test involved using cyclic voltammetry to cycle the sample between -0.5 $V_{Ag/AgCl}$ and +0.9 $V_{Ag/AgCl}$ in 1 M H_2SO_4 one thousand times. As the test continued, the capacitance of the material actually increased.

After examination with a scanning electron microscope, the most likely reason for this occurrence is that cycling the material before annealing removes mixed oxide debris from the surface of the material and exposes more of the nanostructured surface below. For example, take a look at Figures 4.10(a) and 4.10(b). In Fig. 4.10(a), non-cycled material is shown at ~8000X. There is a noticeable lack of planarity, but that is usually a good trait for high double-layer capacitance. In Fig. 4.10(b), the cycled sample seems to have an even greater surface area. The nanostructures are much more visible in this image than in Fig. 4.10(a). After cycling, it seems that features deeper in the oxide layer are available for double-layer capacitance and pseudo-capacitance reactions.

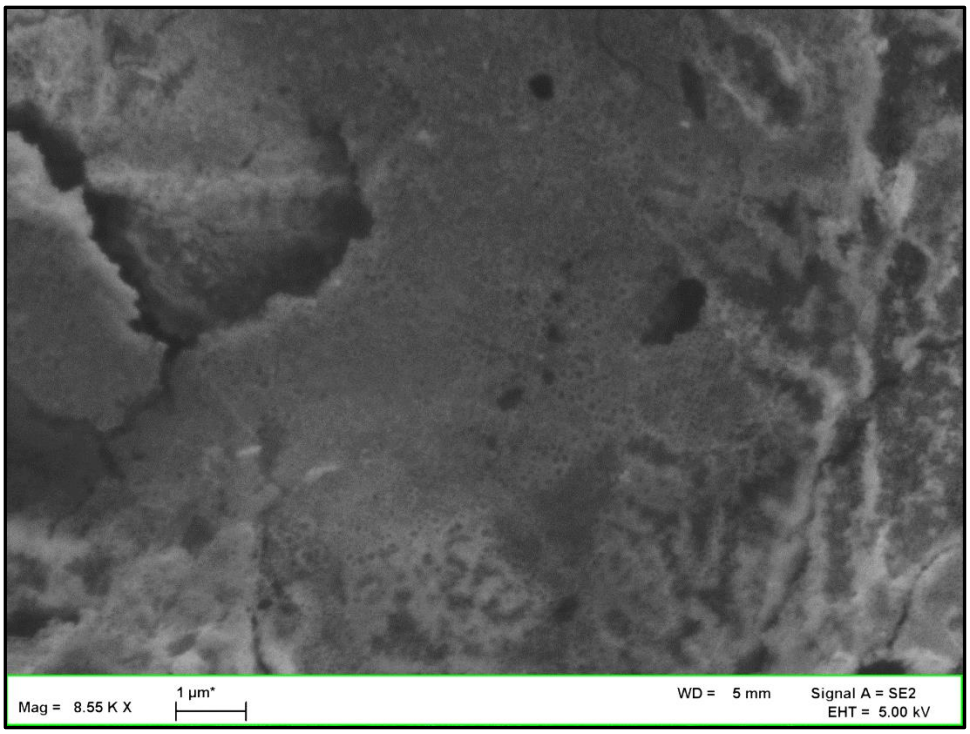

Figure 4.10(a): SEM image of ZrO_2-WO_3 mixed oxide layer formed by anodization at 40 V

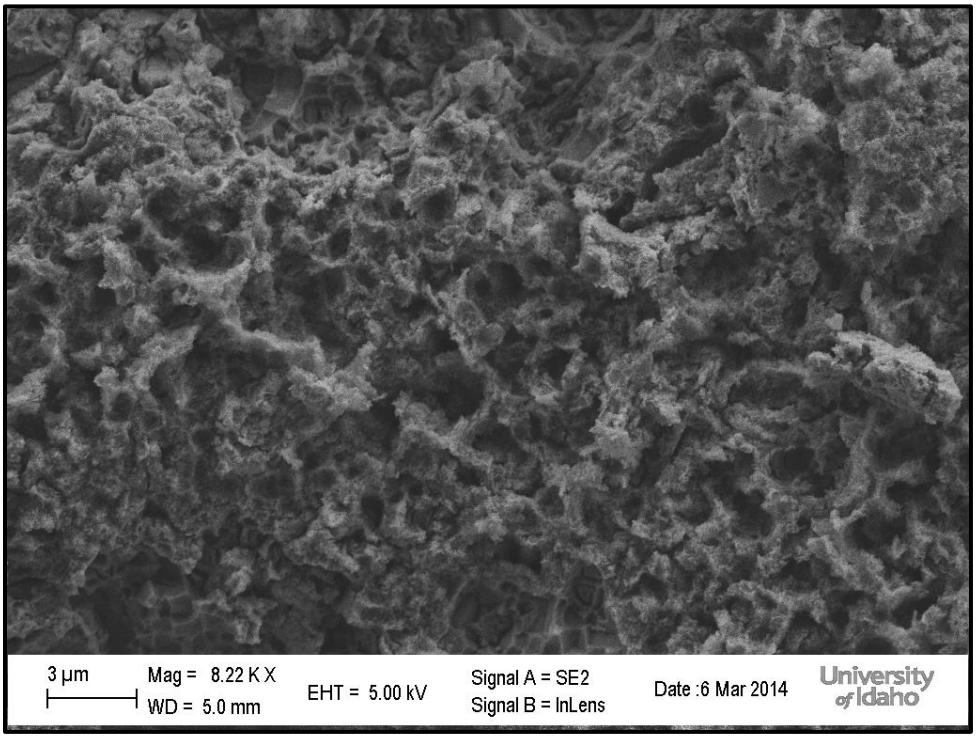

Figure 4.10(b): SEM image of ZrO_2-WO_3 mixed oxide layer formed by anodization at 40 V, then cycled for 1000 cycles in 1 M H_2SO_4

Another possible explanation for the increase in overall capacitance is that the removal of some of the surface oxides is that more WO_3-rich mixed oxide is now available for Faradaic reactions. As the anodization reaction continues, the upper part of the oxide layer contains less and less WO_3, so as that layer is removed via cycling more WO_3 is exposed to the solution increasing the overall capacitance.

4. Electrochemical Characterization

4.1: Cyclic Voltammetry

The cyclic voltammetry (CV) tests performed in this experiment occurred in three different electrolytes: 1 M H_2SO_4, 1 M LiCl, and 1 M $TEABF_4$ in acetonitrile. These three were chosen to see how well the capacitance of the material reacted when trying to intercalate the cations. It also seemed important to test the material in both aqueous and organic electrolyte to observe any noticeable differences.

Three processes contribute to the overall electrochemical capacitance in this system. First, the electrochemical double-layer (EDL) forms when disassociated ions (H^+/SO_4^{2-}, Li^+/Cl^-, TEA^+/BF_4^-) adsorb onto the surface of the nanostructures. They create a wall that prevents charges from moving through the system causing capacitance to form in the system. Ideal EDL capacitors usually form rectangular I-V curves. Second, pseudocapacitance (PC) in the material can be attributed to Faradaic reactions (1) and (2). These are the redox reactions of W^{6+}/W^{5+} and W^{5+}/W^{4+} [25].

$$WO_3 + 2H^+ + 2e^- \leftrightarrow 2\ W_2O_5 + H_2O;\ E_0 = -0.23\ V_{Ag/AgCl} \quad (1)$$

$$W_2O_5 + 2H^+ + 2e^- \leftrightarrow 2WO_2 + H_2O;\ E_0 = -0.225\ V_{Ag/AgCl} \quad (2)$$

The third and final type of capacitance in this system is space layer charging (SLC). This is a semiconductor-like process where oxygen vacancies in the mixed oxide layer act like holes in silicon semiconductors. When a potential bias is applied, such as that during a CV scan, electrons will fill some of the holes creating a depletion layer. The thickness of this layer depends on the amplitude and direction of the bias, but, regardless of its size, it still contributes to the capacitance because it exists as an insulating layer between two conductive layers.

The cyclic voltammetry results for samples formed at 40 V and tested in 1 M H_2SO_4 with a scan rate of 100 mV/s are given in Fig. 4.11(a). Another example of sulfuric acid samples are given in Fig. 4.11(b). These were formed at 60V and they were cycled one thousand times before testing/annealing.

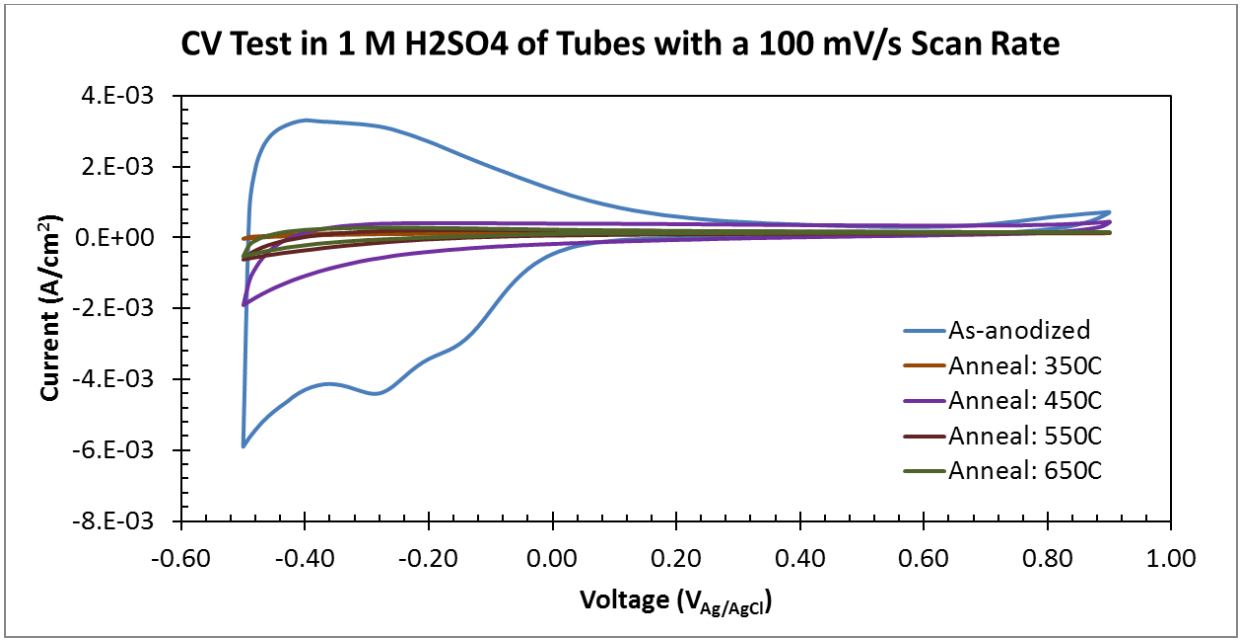

Figure 4.11(a): Representative cyclic voltammetry (CV) results of Zr–W mixed oxide layer tested in 1 M H_2SO_4 with a 100 mV/s scan rate; the tested samples are (a) formed at 40V and not cycled

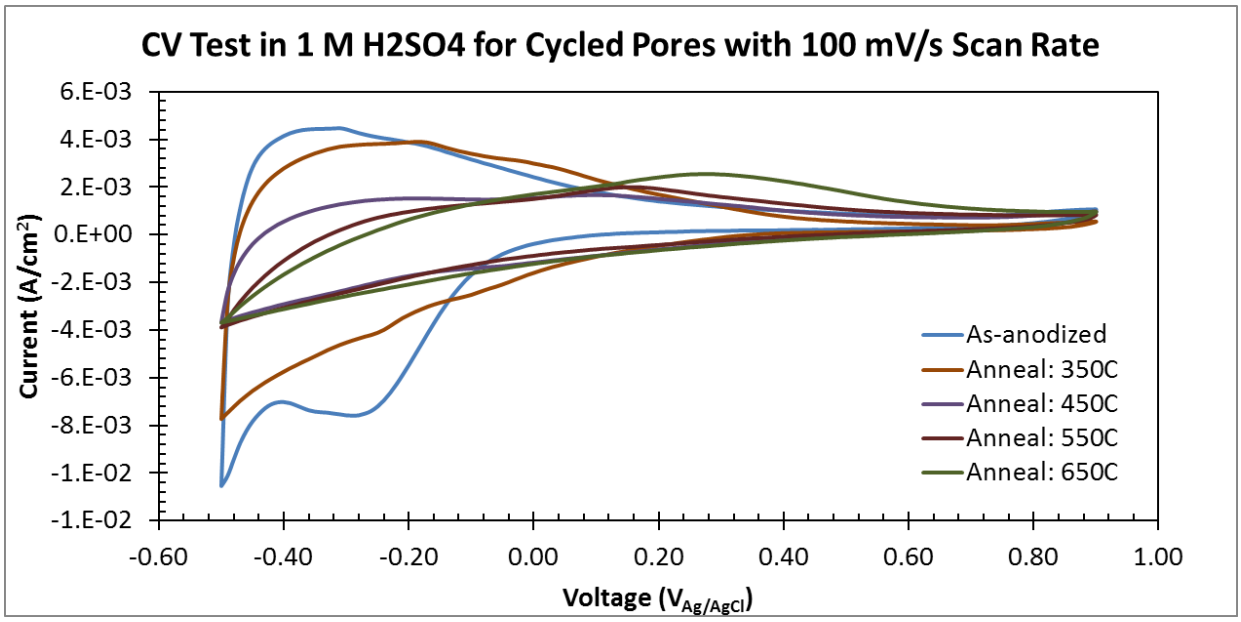

Figure 4.11(b): Representative cyclic voltammetry (CV) results of Zr–W mixed oxide layer tested in 1 M H_2SO_4 with a 100 mV/s scan rate; the tested samples are (b) formed at 60V and are cycled

The large current densities in the negative potential range are clearly the result of the tungsten reactions (1) and (2). The Zr^{4+} in the oxide did not undergo any redox reactions under this potential range for H_2SO_4. The isoelectric point of nanosized ZrO_2 could be around pH: 6 [26]. Therefore, much of the capacitance in the positive region is due to double layer capacitance from the surface potential of the ZrO_2 in the 1 M H_2SO_4 solution. It should be noted that the non-Faradaic current density has a linear dependence on the Faradaic current density [27]. In the absence of a redox reaction, an ideal EDL capacitor will show a rectangular I–V plot. The radius of the roundness of the corners of the I–V plot will increase with the increase in the charge transfer resistance present in series with the EDL capacitor.

Now, here is the same comparison for samples tested in the lithium chloride. Figures 4.12(a) and 4.12(b) show significantly different results. The most noticeable trait about these figures is the remarkably high current density in the positive regions of the voltage range that

seems to disappear with annealing. This is related to isoelectric point of this mixed oxide material. At a pH below 4, such as that in 1 M H_2SO_4, Zr^{4+} is usually covered with a monolayer of $–OH_2^+$ molecules stopping any reaction from occurring. Above that pH, such as that in 1 M LiCl (pH = 5-6), the monolayer consists more of $–O^-$ groups and Li^+ is able to react with the Zr^{4+}. That Zr^{4+} reaction misrepresents the actual magnitude of the capacitance and because of it, the capacitance data for those tests are disregarded. Even though it is noticeable here, it is even worse at the 10 mV/s scan rates because the additional diffusion time allows for even greater reactions.

One final note on this phenomenon, the occurrence of these reactions seems to disappear with higher-temperature annealing. One possible explanation is that oxygen from the commercial-purity nitrogen stream could be bonded with the remaining Zr^{4+} in the metal and preventing future reactions from occurring.

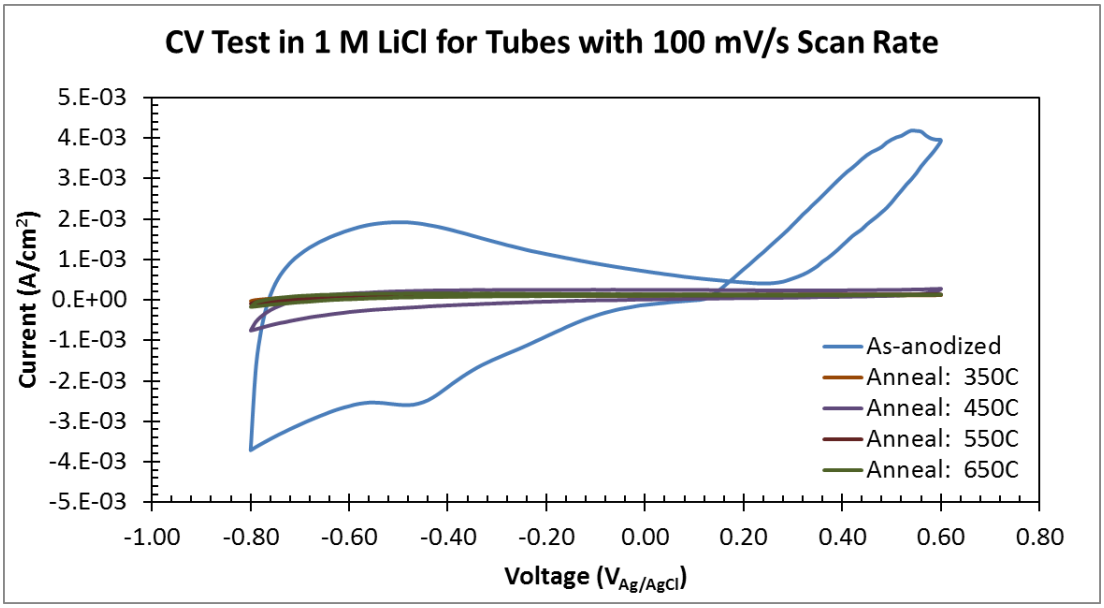

Figure 4.12(a): Representative cyclic voltammetry (CV) results of Zr–W mixed oxide layer tested in 1 M LiCl with a 100 mV/s scan rate; the tested samples are (a) formed at 40 V and not cycled

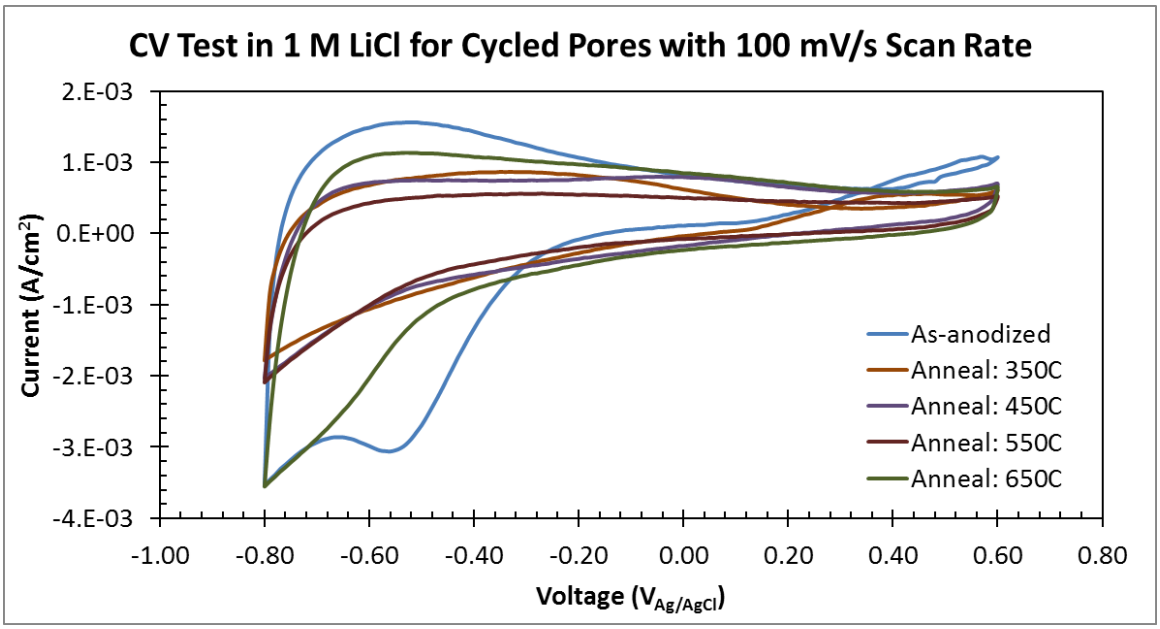

Figure 4.12(b): Representative cyclic voltammetry (CV) results of Zr–W mixed oxide layer tested in 1 M LiCl with a 100 mV/s scan rate; the tested samples are (b) formed at 60 V and are cycled

For the third and final electrolyte, only the cycled samples were tested. Figures 4.13(a) and 4.13(b) show the cyclic voltammetry graphs for the mixed oxide in 1M $TEABF_4$ acetonitrile solution for samples formed at 40 V and 60 V, respectively. There aren't many striking differences between the two graphs, but within them it is clear that something is happening in relation to the annealing temperature. For most of the potential range, the capacitance is dominated by EDL contributions. This is the flat, rectangular area from -0.5 V to +2.0 V. Below that potential, Faradaic reactions may be occurring and this is the cause of the large current densities. At any rate, annealing after cycling seems to allow for greater EDL and PC. This is likely due to the reorganization of material so that more surface area is available for reaction.

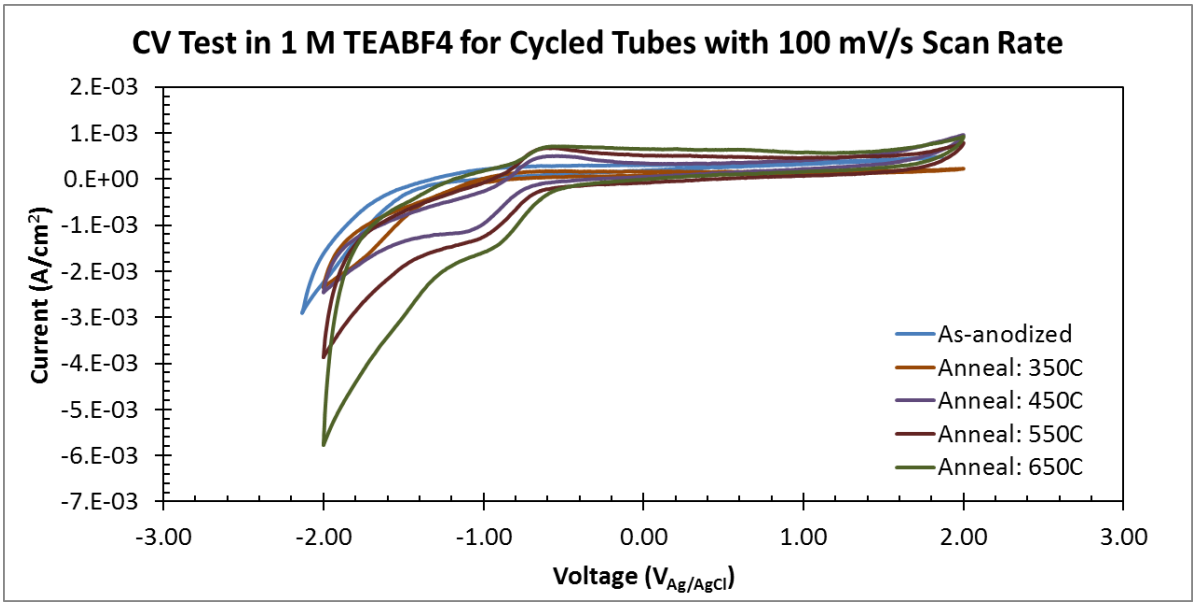

Figure 4.13(a): Representative cyclic voltammetry (CV) results of Zr–W mixed oxide layer tested in 1 M $TEABF_4$ with a 100 mV/s scan rate; the tested samples are (a) formed at 40 V and are cycled

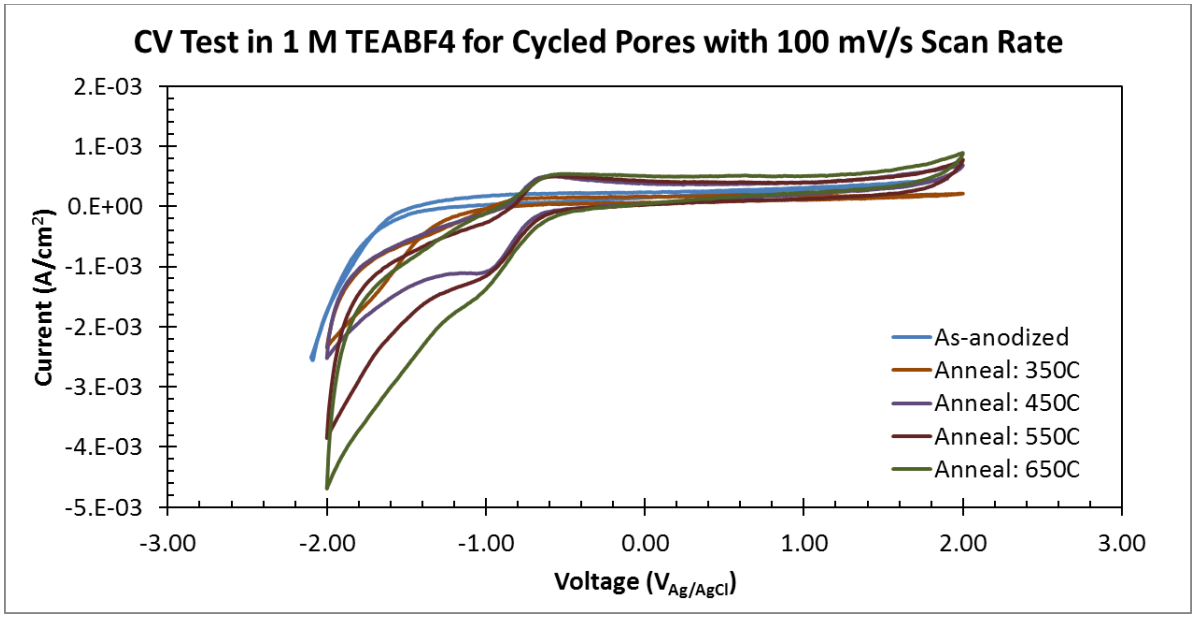

Figure 4.13(b): Representative cyclic voltammetry (CV) results of Zr–W mixed oxide layer tested in 1 M $TEABF_4$ with a 100 mV/s scan rate; the tested samples are (b) formed at 60 V and are cycled

One final comparison between the materials will help cement the idea that the cycled oxides are better than their non-cycled counterparts. Figures 4.14(a) and (b) show the same CV graphs as in Figures 4.11(a) and 4.11(b), but are compared by preparation method instead of annealing condition. The as-anodized condition shows a clear display of the tungsten reactions dominating the capacitance, while the samples annealed at 650^{o}C for two hours show the EDL dominating.

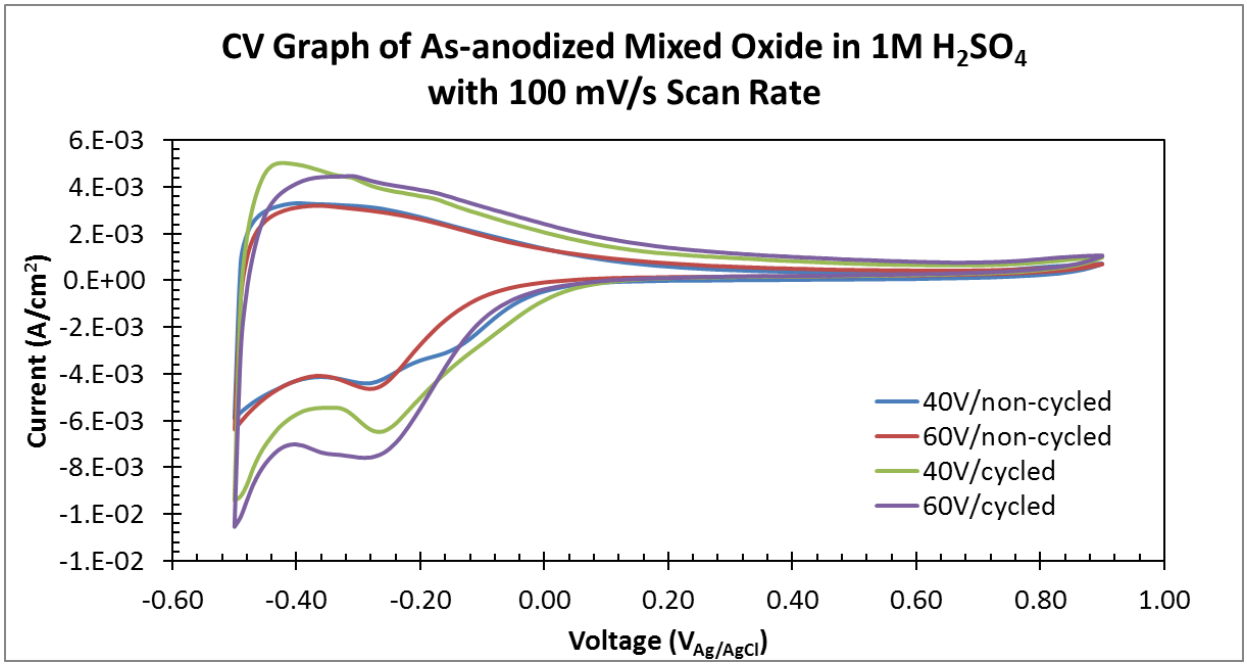

Figure 4.14(a): Representative cyclic voltammetry (CV) results of Zr–W mixed oxide layer tested in 1 M H_2SO_4 with a 100 mV/s scan rate; the tested samples are (a) as-anodized

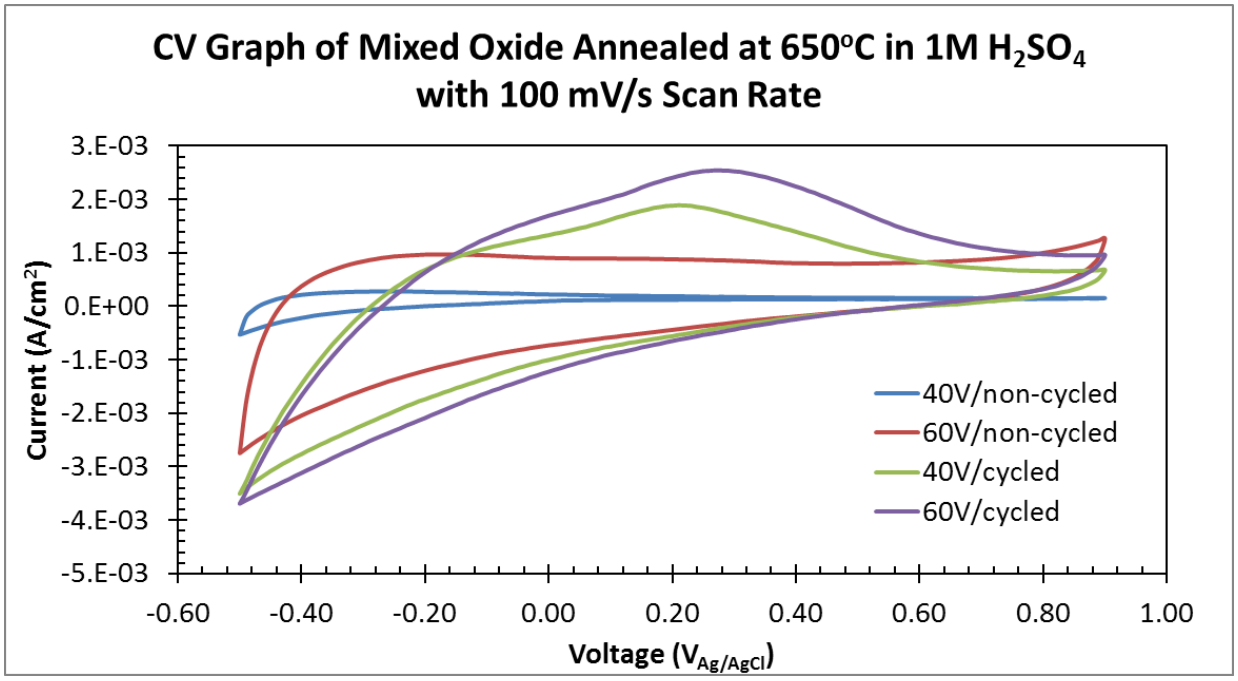

Figure 4.14(b): Representative cyclic voltammetry (CV) results of Zr–W mixed oxide layer tested in 1 M H_2SO_4 with a 100 mV/s scan rate; the tested samples are (b) annealed at 650°C

Overall, the cycled samples performed much better than the non-cycled samples. In fact, their capacitance values were greater than the non-cycled samples in nearly every case. Unfortunately, determining which anodization potential is the better option is not so clear. By comparing the capacitance values between the two potentials and their respective annealing conditions, Figures 4.15(a)-(c) were constructed. These graphs demonstrate some trends in the data.

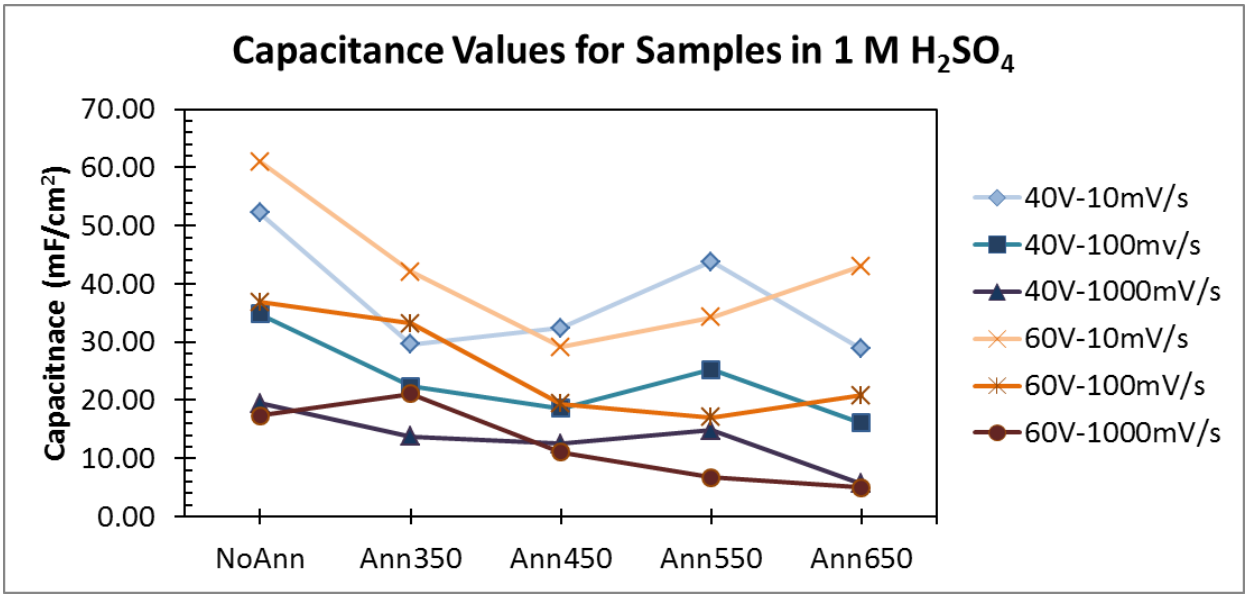

Figure 4.15(a): Capacitance values for cycled mixed oxide samples tested in 1 M H_2SO_4; each data set represents a different anodization condition and potential scan rate

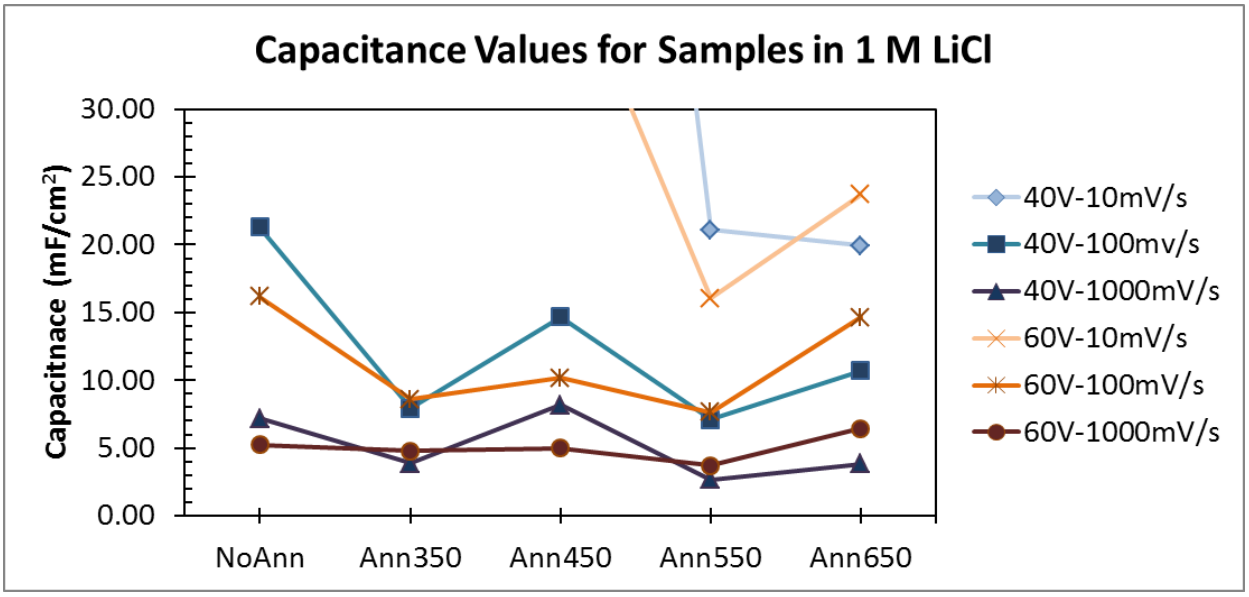

Figure 4.15(b): Capacitance values for cycled mixed oxide samples tested in 1 M LiCl; each data set represents a different anodization condition and potential scan rate; part of the data here is excluded due to Zr reactions interfering with the true results of the tests

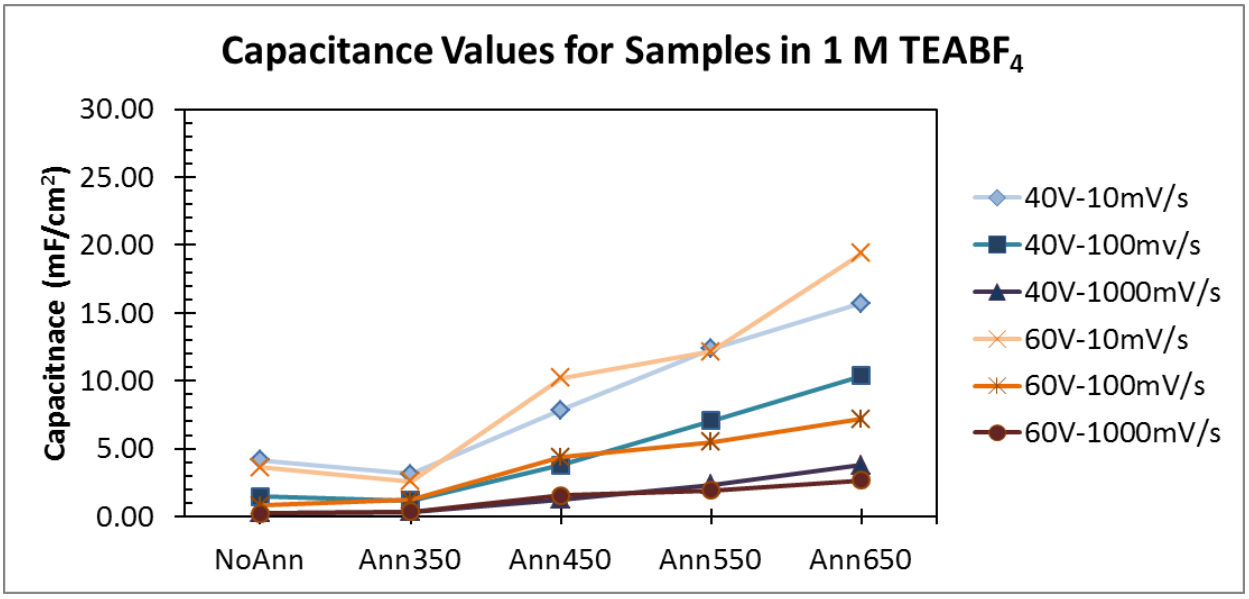

Figure 4.15(c): Capacitance values for cycled mixed oxide samples tested in 1 M $TEABF_4$; each data set represents a different anodization condition and potential scan rate

The first observation one might make from Figures 4.15(a)-(c) is that some of the data are not included in Figure 4.15(b). At the low scan rate of 10 mV/s, the mixed oxide is subject to increased effects from diffusion of the electrolyte into nanostructures. This is part of the reason why the 10 mV/s scan rate capacitances are generally greater than the other scan rate values. While this diffusion is occurring, the H^+, Li^+, and TEA^+ cations from their respective electrolytes are contacting unreacted Zr in the mixed oxide layer. The numerical values of the capacitance are given in Tables 4.1 and 4.2. Table 4.1 contains the data for the non-cycled samples and Table 4.2 contains the data for the cycled samples.

Table 4.1: Capacitance values for non-cycled mixed oxide samples

Voltage	Annealing Temperature	Electrolyte	Scan Rate (mV/s)	Capacitance (mF/cm^2)	Voltage	Annealing Temperature	Electrolyte	Scan Rate (mV/s)	Capacitance (mF/cm^2)
40 V	No Anneal	H2SO4	10	40.52	60 V	No Anneal	H2SO4	10	41.67
			100	24.39				100	30.01
			1000	14.67				1000	6.79
		LiCl	10	389.56			LiCl	10	343.03
			100	14.50				100	24.53
			1000	1.51				1000	3.14
	350 C	H2SO4	10	0.87		350 C	H2SO4	10	15.68
			100	0.13				100	6.82
			1000	0.04				1000	1.81
		LiCl	10	0.56			LiCl	10	97.99
			100	0.24				100	3.41
			1000	0.08				1000	1.06
	450 C	H2SO4	10	10.65		450 C	H2SO4	10	13.19
			100	5.42				100	6.02
			1000	1.94				1000	2.52
		LiCl	10	6.65			LiCl	10	5.82
			100	3.12				100	2.62
			1000	1.20				1000	1.18
	550 C	H2SO4	10	3.13		550 C	H2SO4	10	27.07
			100	1.39				100	13.81
			1000	0.27				1000	6.24
		LiCl	10	9.25			LiCl	10	4.39
			100	5.05				100	3.60
			1000	2.41				1000	1.64
	650 C	H2SO4	10	2.42		650 C	H2SO4	10	27.76
			100	1.33				100	13.97
			1000	0.50				1000	7.19
		LiCl	10	4.42			LiCl	10	29.82
			100	1.88				100	17.95
			1000	0.61				1000	9.93

Table 4.2: Capacitance Values for cycled mixed-oxide samples

Voltage	Annealing Temperature	Electrolyte	Scan Rate (mV/s)	Capacitance (mF/cm^2)	Voltage	Annealing Temperature	Electrolyte	Scan Rate (mV/s)	Capacitance (mF/cm^2)
40 V	No Anneal	H2SO4	10	52.25	60 V	No Anneal	H2SO4	10	61.04
			100	34.86				100	36.88
			1000	19.43				1000	17.36
		LiCl	10	269.90			LiCl	10	255.27
			100	21.31				100	16.17
			1000	7.17				1000	5.23
		TEABF4	10	4.18			TEABF4	10	3.63
			100	1.45				100	0.80
			1000	0.27				1000	0.23
	350	H2SO4	10	29.60		350	H2SO4	10	42.11
			100	22.41				100	33.16
			1000	13.76				1000	21.14
		LiCl	10	203.19			LiCl	10	273.48
			100	7.91				100	8.60
			1000	3.88				1000	4.79
		TEABF4	10	3.11			TEABF4	10	2.58
			100	1.18				100	1.22
			1000	0.36				1000	0.37
	450	H2SO4	10	32.46		450	H2SO4	10	29.13
			100	18.61				100	19.37
			1000	12.48				1000	11.07
		LiCl	10	113.18			LiCl	10	42.48
			100	14.69				100	10.17
			1000	8.19				1000	4.98
		TEABF4	10	7.83			TEABF4	10	10.21
			100	3.77				100	4.38
			1000	1.25				1000	1.55
	550	H2SO4	10	43.83		550	H2SO4	10	34.26
			100	25.26				100	17.01
			1000	14.84				1000	6.76
		LiCl	10	21.11			LiCl	10	16.07
			100	7.10				100	7.63
			1000	2.66				1000	3.69
		TEABF4	10	12.36			TEABF4	10	12.17
			100	7.08				100	5.47
			1000	2.35				1000	1.91
	650	H2SO4	10	28.80		650	H2SO4	10	43.07
			100	16.13				100	20.78
			1000	5.69				1000	4.97
		LiCl	10	19.93			LiCl	10	23.70
			100	10.70				100	14.64
			1000	3.82				1000	6.46
		TEABF4	10	15.71			TEABF4	10	19.42
			100	10.36				100	7.19
			1000	3.80				1000	2.67

4.2: Extended Cycling and Stability Testing

In addition to the basic cyclic voltammetry tests, two samples prepared at different conditions were subjected to 10000 cycles of rapid (1000 mV/s) CV tests in 1 M H_2SO_4. At every 1000 cycle interval, EIS and Mott-Schottky tests were performed to observe the change in the oxide layer properties. The first sample was prepared by anodizing at 40 V but no annealing occurred. The second sample was prepared by anodizing at 60 V and then it was annealed at 650^{o}C for 2 h. Figure 4.16 shows the change in the capacitance between the two samples during the cycling.

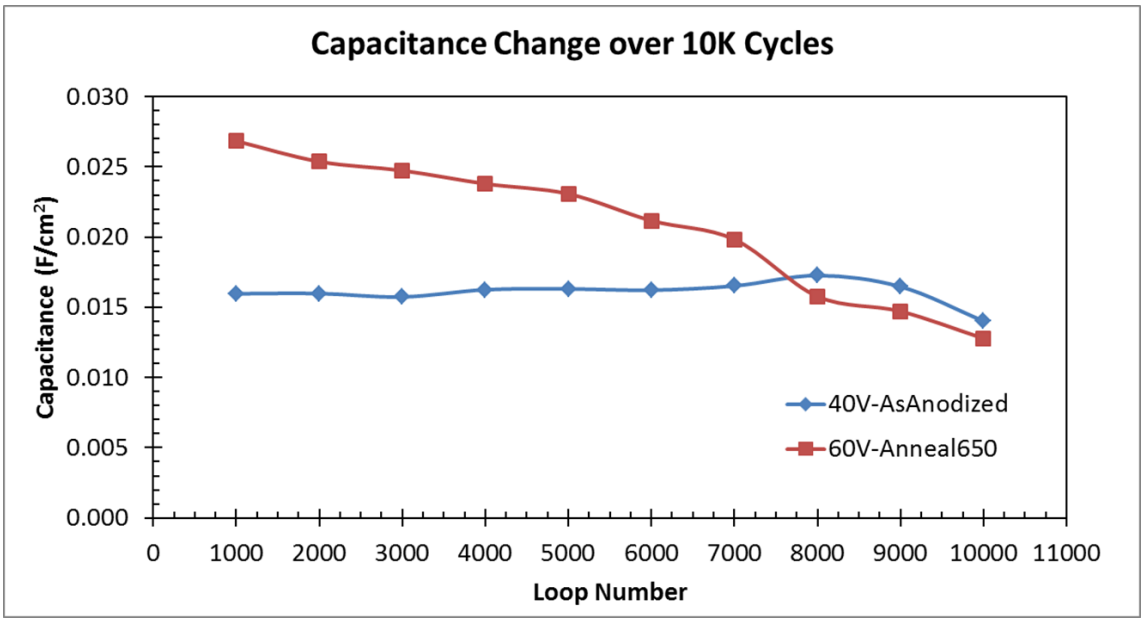

Figure 4.16: Change in capacitance of mixed oxide layer for two different preparation conditions during 10000 cycles of CV testing.

The capacitance of the as-anodized piece remained fairly constant for approximately 8000 cycles while the sample that was annealed at 650^{o}C lost capacitance over the entire testing range. Even though the annealed sample generally had a higher capacitance, the persistent loss of that capacitance during cycling is sign of the change in the material due to annealing. To get a better idea of the process occurring during cycling an examination of the respective Nyquist and

Bode plot may be necessary. Figures 4.17(a) and (b) show the Nyquist plots for the annealed and as-anodized samples, respectively, while Figures 4.18(a) and (b) show the Bode plots for the same samples.

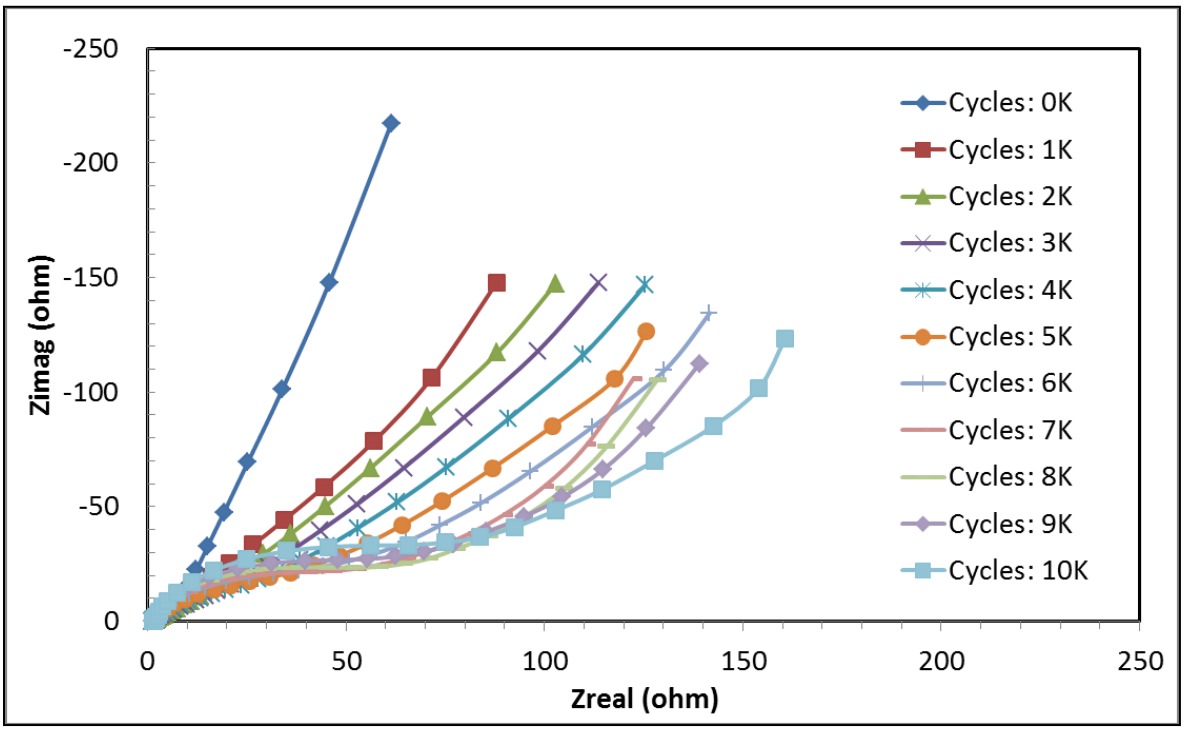

Figure 4.17(a): Nyquist plot for mixed oxide sample anodized at 60V and annealed at 650^{o}C during the course of 10000 cycles of CV testing

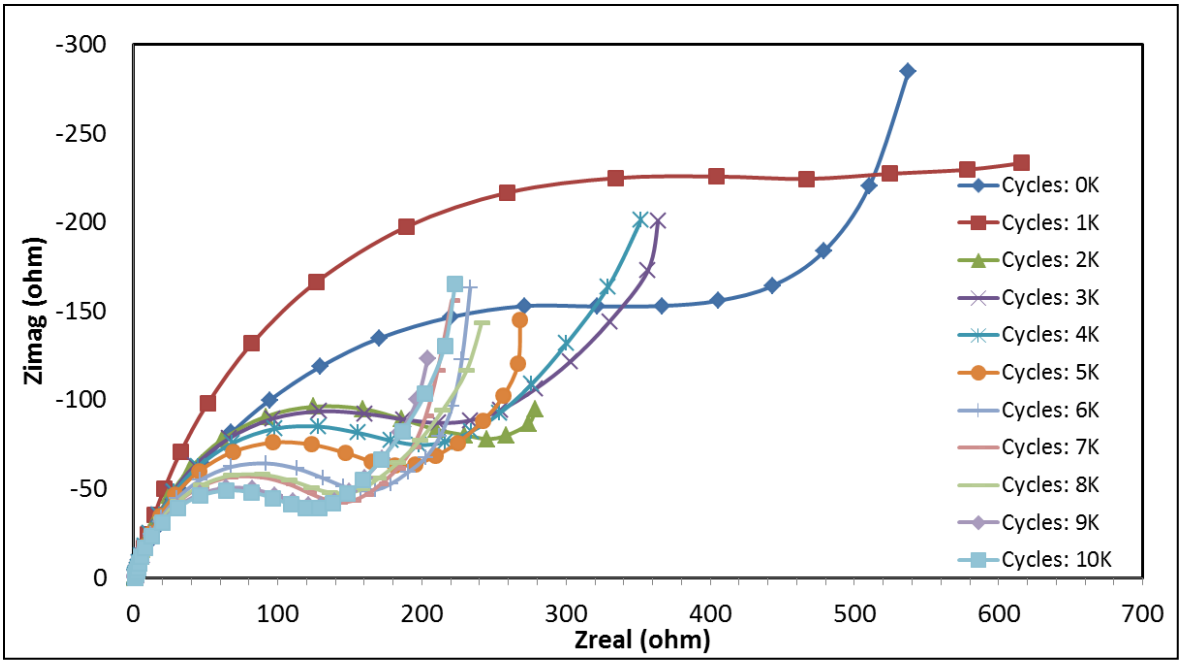

Figure 4.17(b): Nyquist plot for mixed oxide sample anodized at 40V and but not annealed during the course of 10000 cycles of CV testing

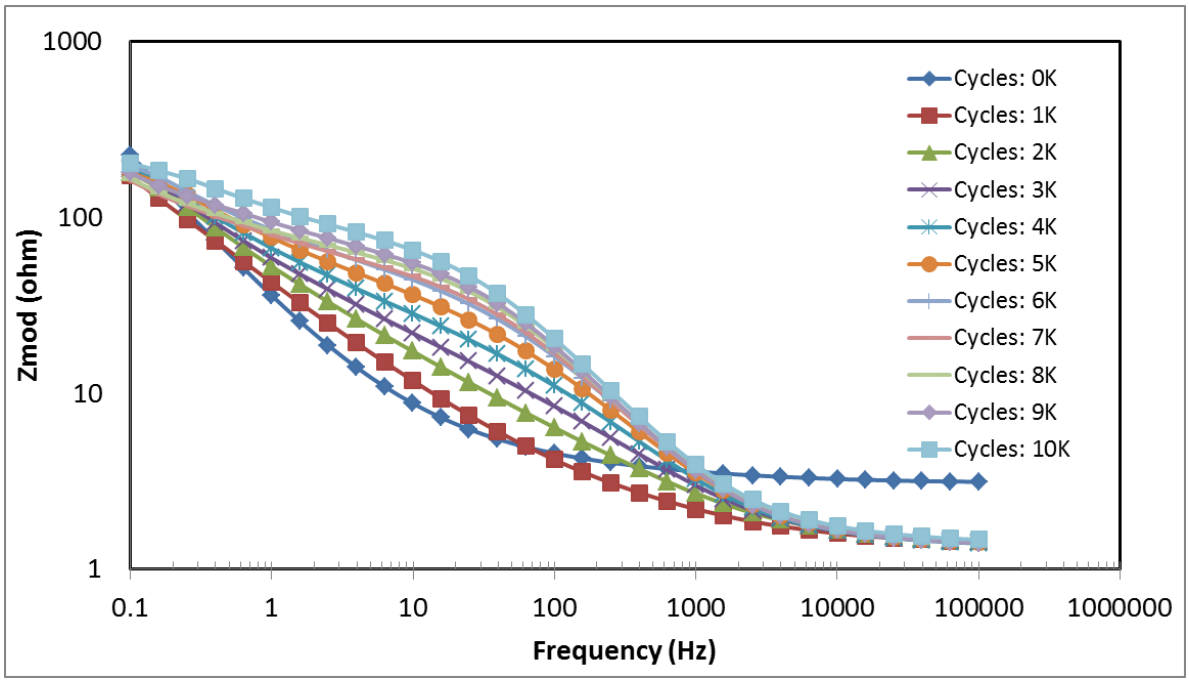

Figure 4.18(a): Bode plot for mixed oxide sample anodized at 60V and annealed at 650^{o}C during the course of 10000 cycles of CV testing

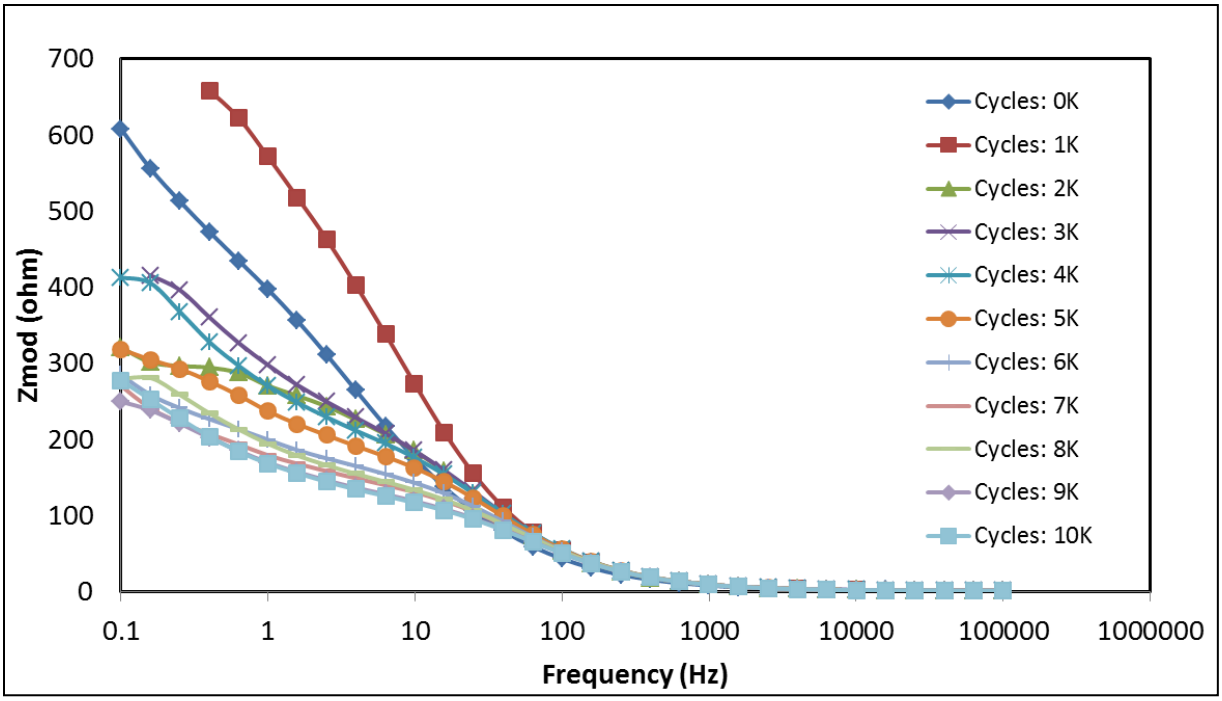

Figure 4.18(b): Bode plot for mixed oxide sample anodized at 40V but not annealed during the course of 10000 cycles of CV testing

When we compare the two Nyquist plots in Fig. 4.17, it becomes clear that two different effects are occurring. The resistance in the annealed sample increases with cycling, thus contributing to the decrease in capacitance, but the resistances in the as-anodized sample decrease. Several mechanisms might be at work in this system. First, during the annealing process, the ZrW_2O_8 phase decomposes into its binary oxides. This is the case when the annealing temperature is above 450^{o}C. Also at temperatures above 450^{o}C, hexagonal WO_3 transforms into monoclinic WO_3. M-WO_3 has been reported to have capacitance like h-WO_3 but not nearly as strong. This may seem strange considering the data from Fig. 4.16 demonstrates the annealed form have higher capacitance initially. This is more likely due to the higher surface area that the annealed sample possesses instead of tungsten-related pseudo-capacitance. At the 1000 mV/s scan rate the ions don't have time to diffuse to the surface of the oxide to undergo reactions but the double-layer capacitance mechanism is nearly instantaneous.

The next possible contributing factor to these changes during CV cycling involves physical changes to the mixed oxide. Observe the Bode plot in Fig. 4.18(a). During the beginning of the test, the impedance was constant from high frequency down to 100 Hz. As cycling continued, that transition frequency moved further and further right. The annealed sample was becoming more of an ion conductor than as electron conductor. Part of this might be due to the degradation of the mixed oxide due to cycling effects.

While the annealed sample decreased in capacitance, the as-anodized sample held nearly constant during the same process. Degradation and loss of the mixed oxide certainly occurred in this sample, it is what likely led to the decrease in capacitance after 8000 cycles. However, when comparing Figs. 4.17(b) and 4.18(b) a different picture than the one for the annealed sample is formed. The m-WO_3 and m-ZrO_2 which form due to the decomposition of ZrW_2O_8 may be preferentially removed during cycling. While this would certainly contribute to a decrease in capacitance, the loss of material may have been balanced out by the opening of ion pathways via the rotating polyhedrons in the ZrW_2O_8 phase for the as-anodized material only. This would explain the decreased resistance in Fig. 4.17(b). Also, the moving transition frequency that was notable in Fig. 4.18(a) is not moving in Fig. 4.18(b). The exact mechanism behind this phenomenon is not well understood at this time, but future research into these events is planned for future investigations.

4.3: Charge Carrier Density

Insight into the charge behavior of the different mixed oxides during cycling may be found by examining the electronic structure of the material. To that end, several Mott-Schottky tests were performed at each 1000^{th} interval of the 10,000 cycle test. These same Mott-Schottky tests were also performed on the regular series of samples that were not subject to 10,000 cycles

of CV testing but were still examined for the sake of research. Figures 4.19(a)-(c) show Mott-Schottky plots of no particular importance. All of the Mott-Schottky plots for both the cycled and non-cycled sample displayed a structure similar to those given in Fig. 4.19.

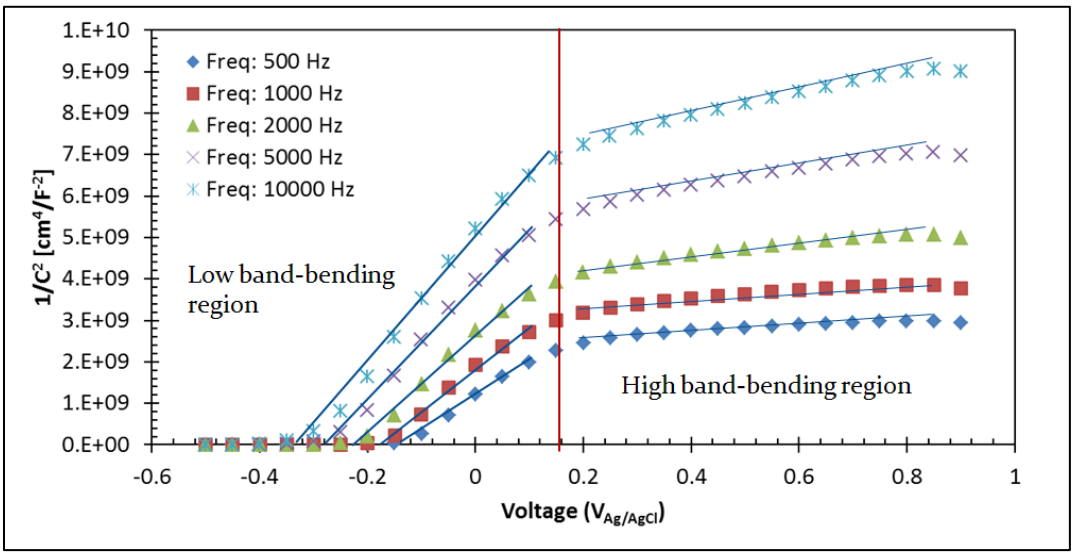

Figure 4.19(a): Mott-Schottky plot of mixed oxide in 1 M H_2SO_4; anodized at 40V and not annealed; this is after the 5000th CV cycle.

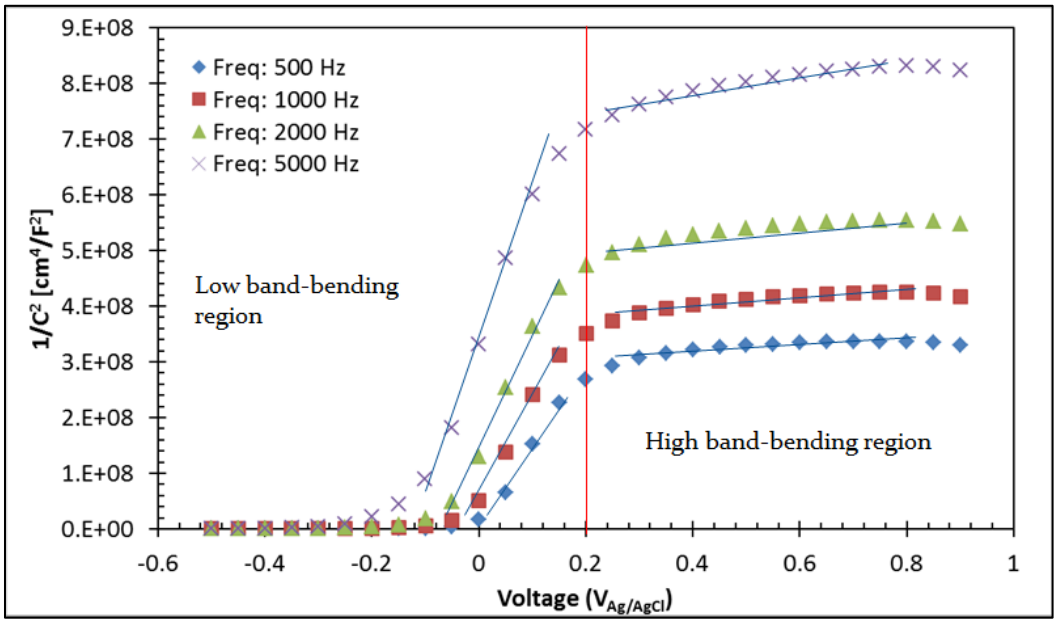

Figure 4.19(b): Mott-Schottky plot of mixed oxide in 1 M H_2SO_4; anodized at 60V and annealed at 650^{o}C; this is after the 8000th CV cycle.

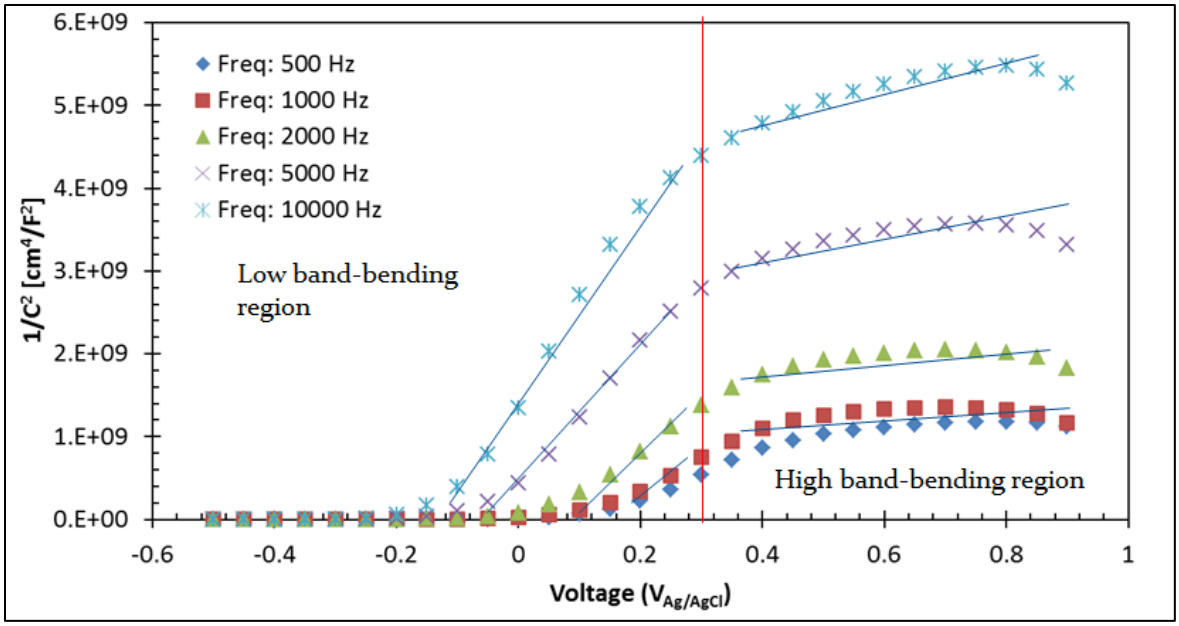

Figure 4.19(c): Mott-Schottky plot of mixed oxide in 1 M H_2SO_4; anodized at 40V and annealed at 350^{o}C; this one was not from the ten thousand cycle test

The Mott–Schottky relation assumes uniform distribution of the charge carriers in the material of investigation. However, such an assumption may not be valid when multiple phases are present in the Zr–W oxide nanotubes. Therefore, Mott–Schottky measurements were carried out at multiple frequencies from 500 to 5000 Hz. After collating the data, the Mott-Scottky plot showed two regions of linearity. The region at lower potentials, labeled as low band bending region, showed steeper slopes. The region at higher anodic potentials, labeled as high band bending region, showed shallower slopes. The positive slope of the Mott–Schottky plot indicated the material to be an n-type semi-conductor. Therefore, the charge carriers could be due to oxygen vacancies. The charge carrier densities of the samples were calculated from the slopes of the Mott–Schottky plots, assuming a lumped dielectric constant of 36. (The dielectric constant of amorphous ZrO_2 is about 22.2 [28], and the dielectric constant of amorphous WO_3 is 90 [29]. Based on their composition by mass in the material, we assumed the lumped dielectric constant of 36.) Values for the charge carrier densities of the two mixed oxide during the 10,000 cycle test

at 1000 Hz are given in Table 4.3. Values for the charge carrier densities of the regular materials that were only tested in 1 M H2SO4 and at 1000 Hz are given in Table 4.4.

Table 4.3: Charge carrier densities of mixed oxide samples tested in 1 M H_2SO_4 for 10000 cycles; the values displayed here are for the 1000 Hz frequency; density is measured in cm^{-3}

Number of Cycles	**Anodized: 40V Anneal: None**	**Anodized: 60V Anneal: 650°C**
Before Cycling	3.46E+20	2.81E+22
1000	3.50E+20	4.65E+21
2000	3.95E+20	4.13E+21
3000	4.04E+20	3.57E+21
4000	3.91E+20	3.16E+21
5000	3.96E+20	2.74E+21
6000	4.12E+20	2.60E+21
7000	4.30E+20	2.34E+21
8000	4.83E+20	2.22E+21
9000	5.10E+20	2.22E+21
10000	5.20E+20	2.18E+21

It is fairly easy to spot the trend in charge carrier density change from the data in Table 4.3. In the sample that was annealed at 650°C, the number of charge carriers decreases as cycling continues. One explanation may be that the tungsten in the mixed oxide tends to oxidize during the cycling. Because of this it creates more stoichiometric WO_3 in the mixed oxide. With fewer oxygen vacancies in the bulk material, fewer negative surface particles are necessary for charge neutrality. This is supported somewhat by the shifting flat-band potential as seen in Fig. 4.18(a).

This would result in decreased electron conductivity and decreased capacitance. The trend in the as-anodized sample is more difficult to explain. While it is obvious that the number of charge carriers is increasing, the reason for this change is not well known at this time. One possibility is that the dielectric constant of the material is changing (similar to how the resistance is changing as shown in Fig. 4.17(b)) and that would throw off the calculations.

Table 4.4: Charge carrier densities of mixed oxide samples; the values displayed here are for the 1000 Hz frequency; charge carrier density is measured in cm^{-3}

Annealing Condition	**Anodized at 40 V**	**Anodized at 60 V**
As-anodized	4.93E+18	2.33E+18
Annealed at 350 ^{o}C	9.56E+18	1.04E+19
Annealed at 450 ^{o}C	2.43E+20	2.84E+20
Annealed at 550 ^{o}C	2.96E+20	2.48E+20
Annealed at 650 ^{o}C	8.25E+20	1.72E+21

The data from Table 4.4 shows that annealing the mixed oxide samples increased the number of charge defects. The increase in charge defects could be due to additional oxygen vacancies forming during the annealing process when t-ZrW_2O_8 separates into its binary oxides. However, there are the energetics of the process to be concerned about, and as mentioned earlier the exact mechanism behind this phenomenon is not well known at this time, but further research into it has been planned for future investigations.

4.4: Charge/Discharge Testing

The final set of tests we performed on these samples was meant to see how they would react in a more realistic scenario. They were charged and discharged at constant currents and using that data, the approximate power and energy output for each preparation condition was found. Figures 4.20(a)-(d) show four examples of the collected charge-discharge curve data.

These are only for sample tested in 1M H_2SO_4. The curves are similar for the samples tested in LiCl and $TEABF_4$, but their voltage ranges are different. The charge/discharge curves consist of two major parts, the charge curve and the discharge curve. In the charge curve (where the voltage is rising) there are two semi-linear portions. They both indicate different processes contributing to the charging of the sample. The one with the flatter slope is indicative of the pseudo-capacitance reactions plus the double layer capacitance, whereas the steeper slope only benefits from the double-layer capacitance. The discharge curve contains an immediate and very steep drop right after the discharge stage begins. This is called the IR-drop and it is generally a poor trait to have as it indicates lost energy during the current switch. As is evident from Figs. 4.20(a) – (d), the IR-drops are really defined and are the reason for a majority of the lost energy. Comparing the annealing oxides of Figs. 4.20(c) and (d) to the as-anodized oxides in Figs. 4.20(a) and (b) it appears that annealing the mixed oxide reduces the IR-drop significantly.

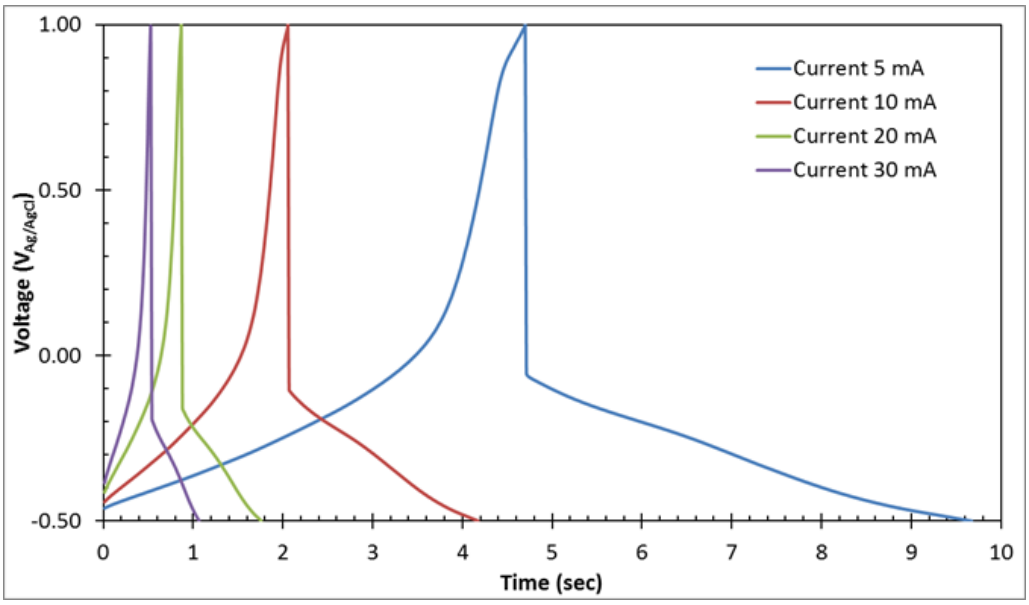

Figure 4.20(a): Charge/discharge curves for the sample anodized at 40 V but not annealed at four different constant currents tested in 1 M H_2SO_4

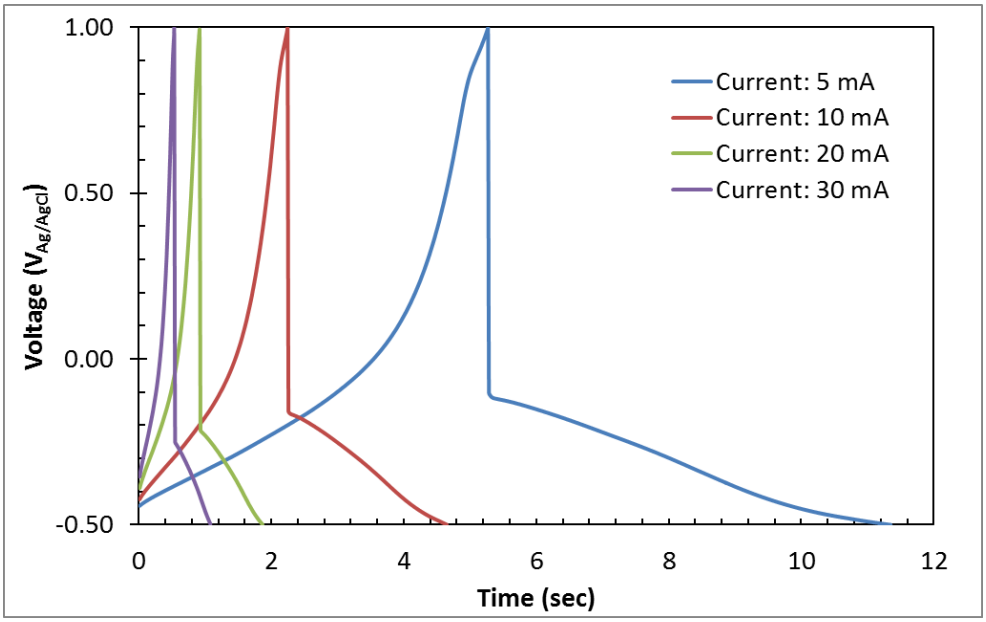

Figure 4.20(b): Charge/discharge curves for the sample anodized at 60 V but not annealed at four different constant currents tested in 1 M H_2SO_4

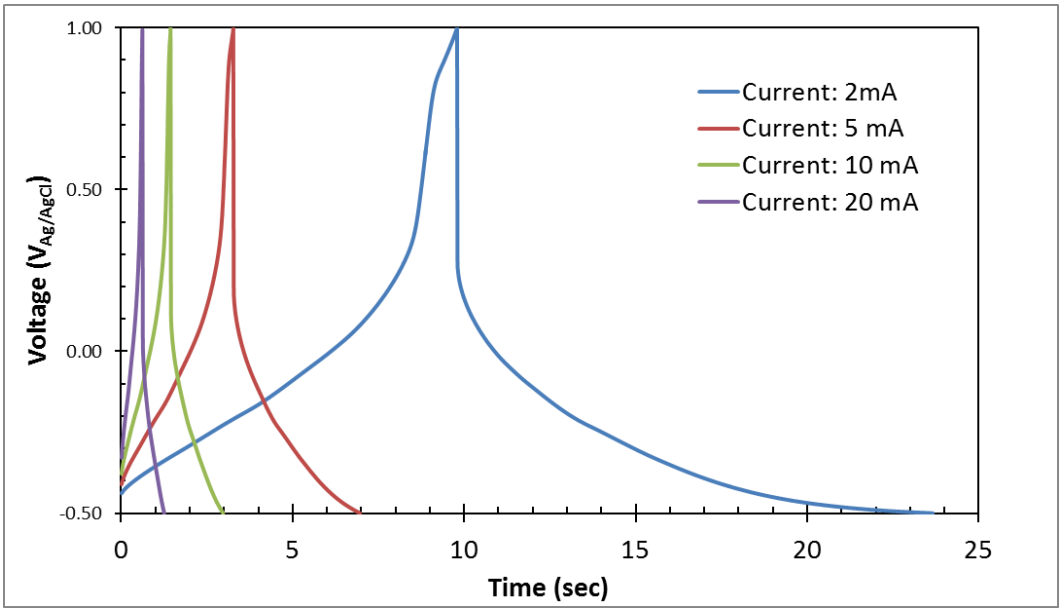

Figure 4.20(c): Charge/discharge curves for the sample anodized at 40 V and annealed at 350^{o}C at four different constant currents tested in 1 M H_2SO_4

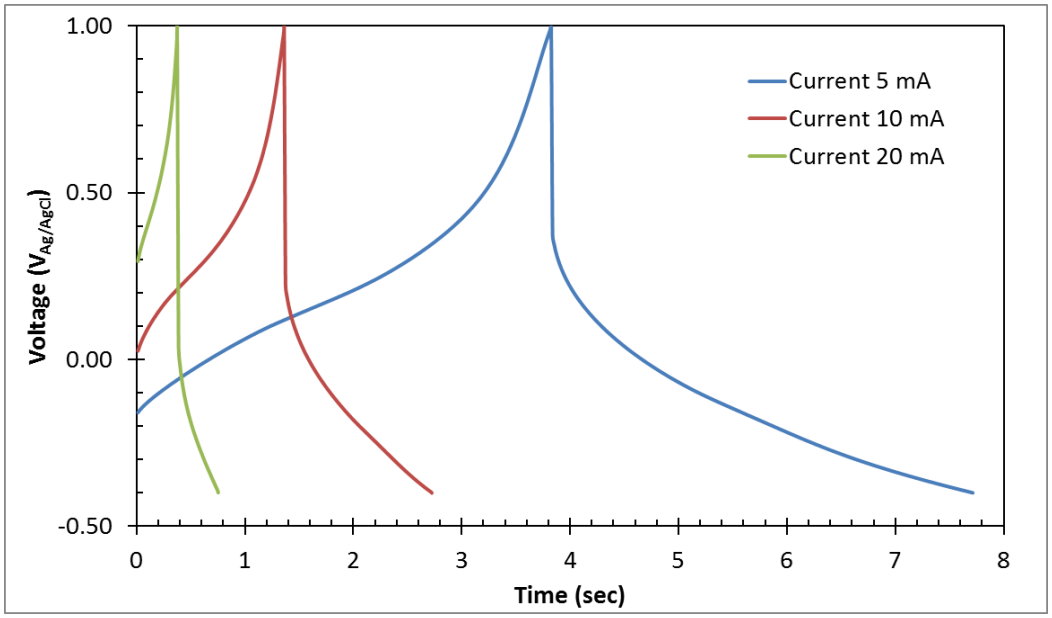

Figure 4.20(d): Charge/discharge curves for the sample anodized at 60 V and annealed at 650^{o}C at four different constant currents tested in 1 M H_2SO_4

Regardless of the capacitance values that were calculated from the CV tests, the power density and energy density are better indicator of how the material would behave in normal operating conditions. These values were determined solely from the output curve of the data, seeing that is the power/energy that would be available during normal conditions. The power (P=V*I) is calculated by multiplying the voltage change after the IR-drop and the constant current. The energy (E=P*t) is calculated by multiplying the power by the time it takes to discharge the sample. In the case of samples tested in 1M H_2SO_4, this would be the time it takes to discharge down to -0.5 V. In some cases though, like Fig. 4.20(d), this value is -0.4 V. The reason for this is that at lower currents, there would be a battery-like charging effect where the mixed oxide simple wouldn't reach -0.5 V and, in fact, would begin moving in a positive direction. Since that is not a desirable capacitor trait, the potential ranges were changed so that would not occur.

The value calculated for power and energy outputs for the mixed oxide samples were then divided by the area of the oxide on the metal alloy substrate. The area used in this calculation is not the surface area of the oxide, but it is the apparent area. That is, of the 1.0 cm x 1.5 cm surface area of the starting metal coupon, approximately 1.0 cm^2 was anodized. The actual value changed somewhat from sample to sample but they were still used to calculate a pseudo-specific power and energy. Determining the actual mass of the oxide layer is difficult due to its adherence to the metal surface. Instead of proper Ragone charts, Figures 4.21(a)-(f) contain the energy and power output of the mixed oxide samples at all their preparation conditions with respect to area instead of mass. Also, they are on linear plots instead of logarithmic plots.

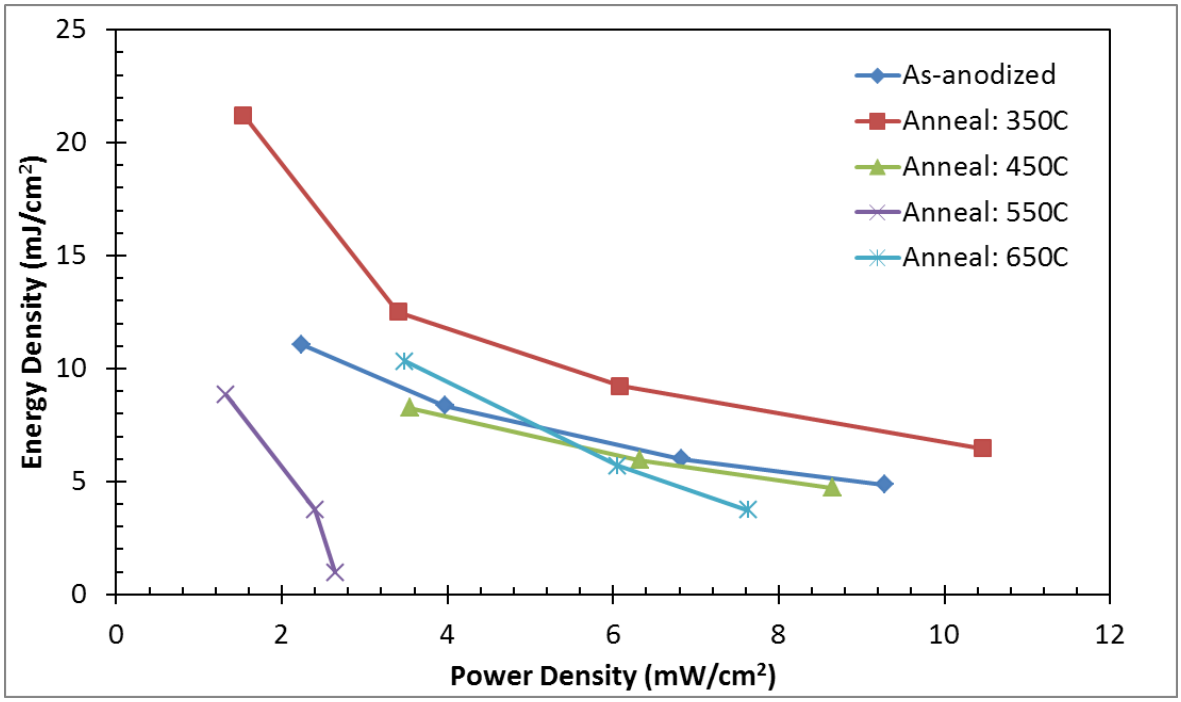

Figure 4.21(a): Chart of Energy Density vs. Power Density for all samples anodized at 40 V and tested in 1 M H_2SO_4

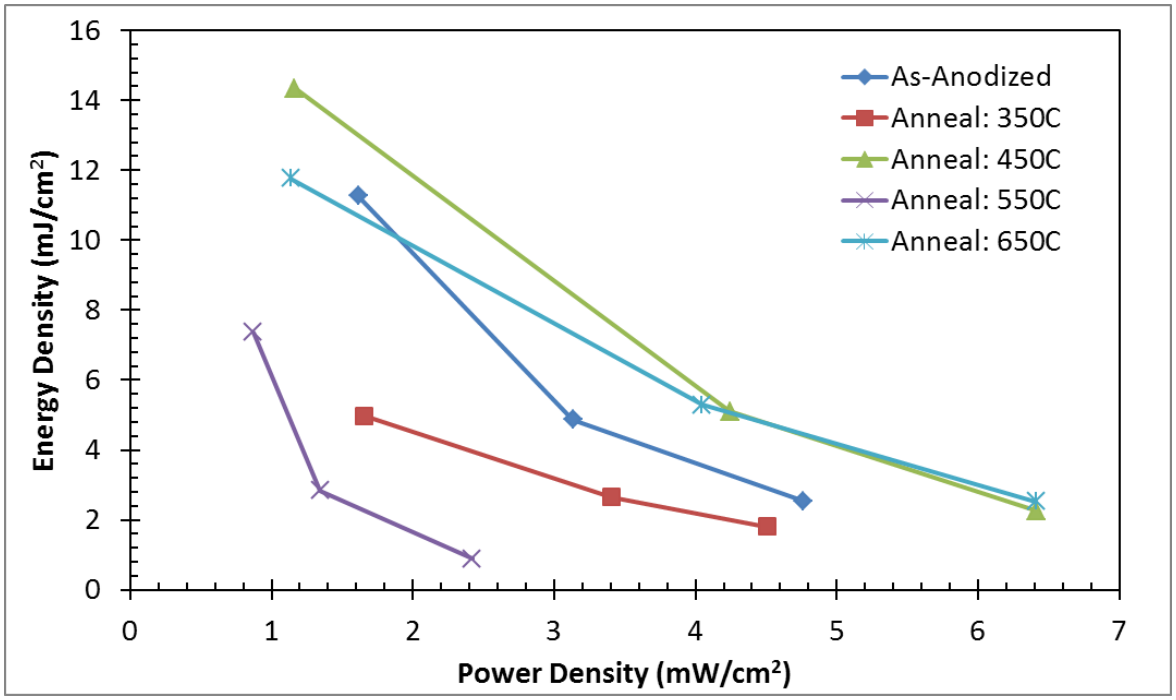

Figure 4.21(b): Chart of Energy Density vs. Power Density for all samples anodized at 40 V and tested in 1 M LiCl

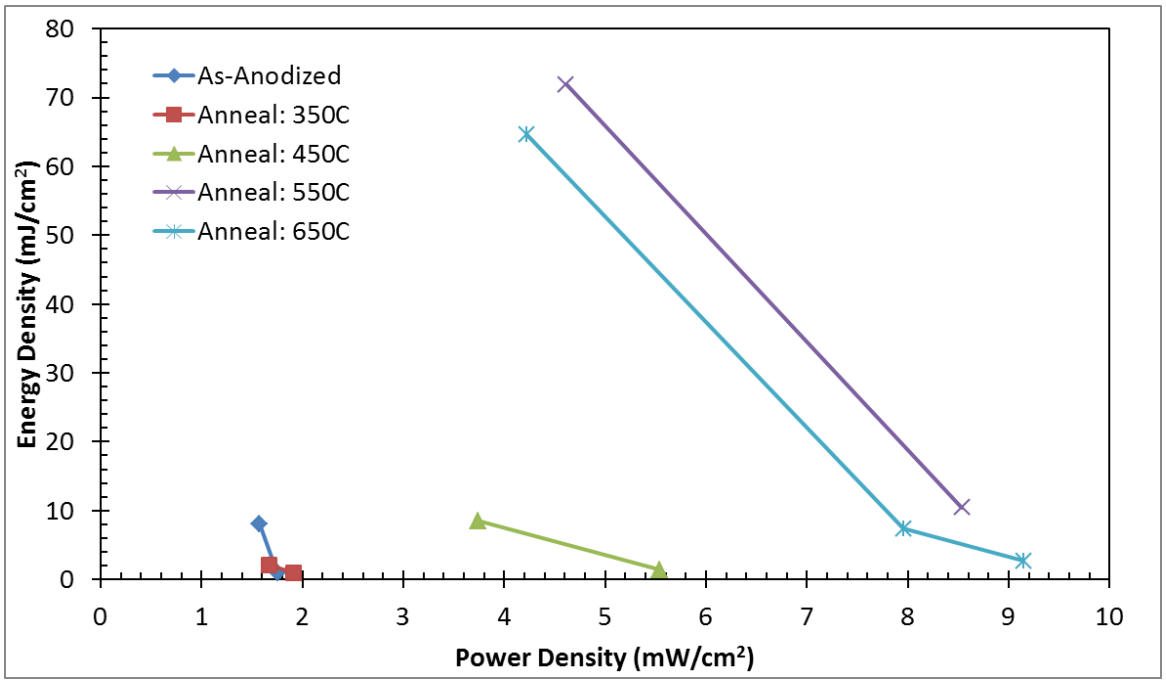

Figure 4.21(c): Chart of Energy Density vs. Power Density for all samples anodized at 40 V and tested in 1 M $TEABF_4$

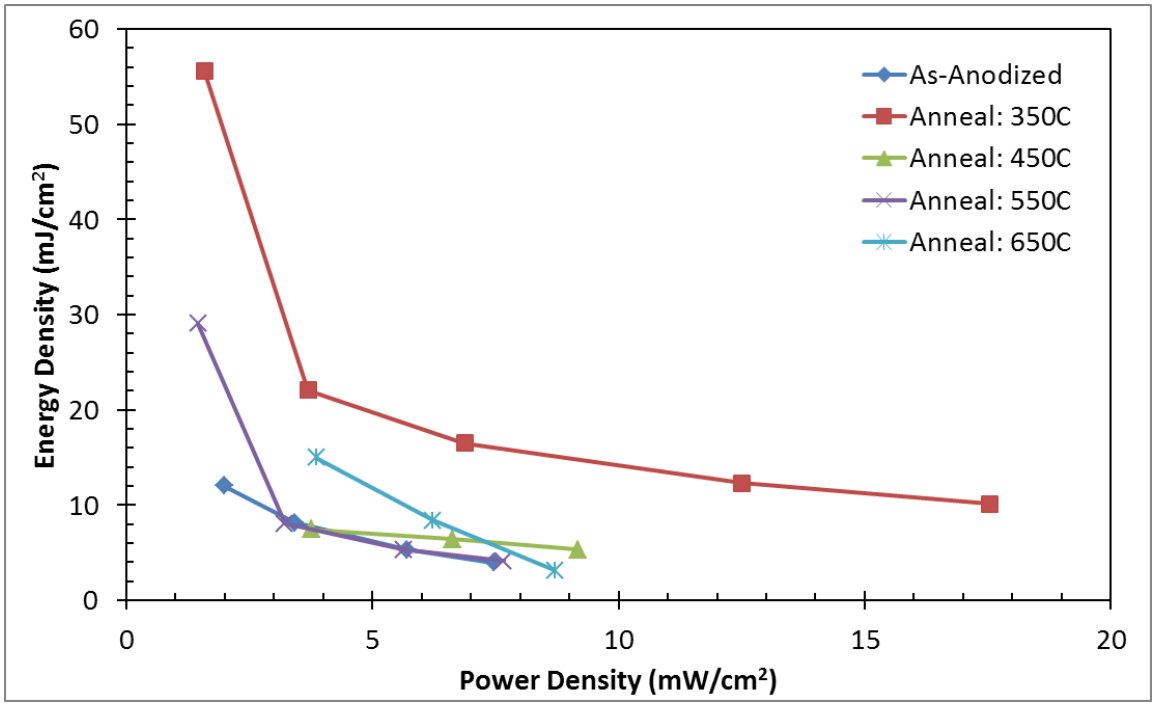

Figure 4.21(d): Chart of Energy Density vs. Power Density for all samples anodized at 60 V and tested in 1 M H_2SO_4

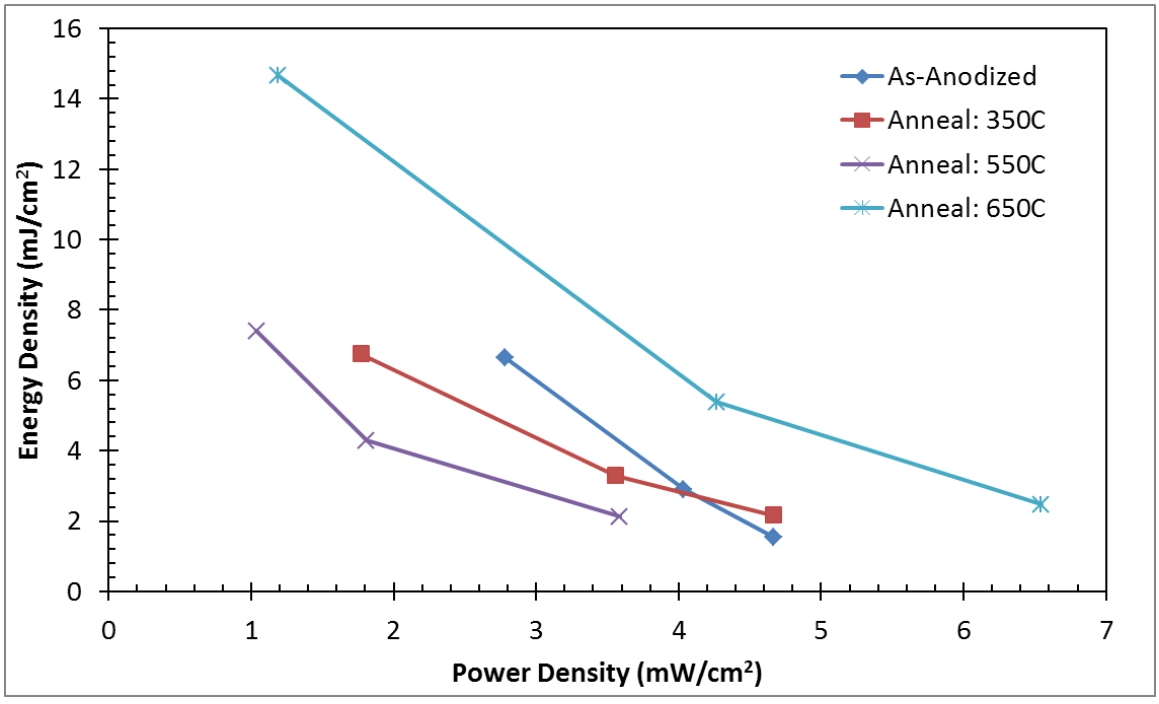

Figure 4.21(e): Chart of Energy Density vs. Power Density for all samples anodized at 60 V and tested in 1 M LiCl

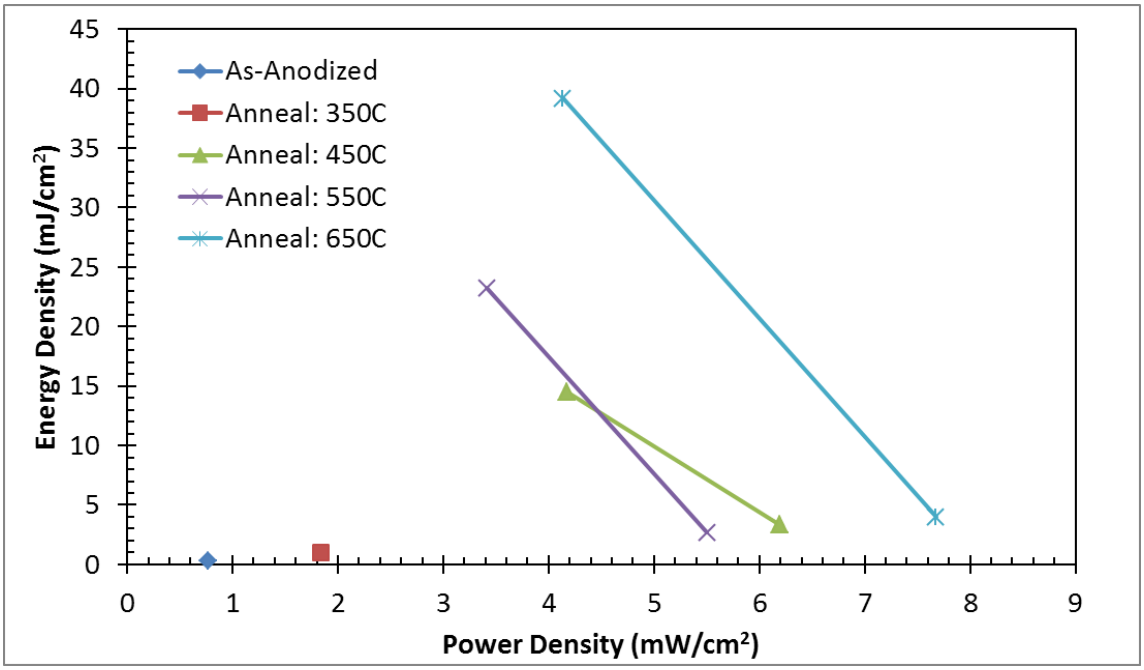

Figure 4.21(f): Chart of Energy Density vs. Power Density for all samples anodized at 60 V and tested in 1 M $TEABF_4$

5. Conclusions

Using a simple anodization method, ZrO_2-WO_3 mixed oxide was created on the surface of 80Zr-20W metal alloy. This substance was considered for application in electrochemical capacitors. A variety of preparation conditions including different anodization potentials, annealing temperatures, electrolytes, and even an additional step of 1000 CV cycles prior to annealing were examined to determine optimum capacitance. The material forms a highly disordered nanotubular array when it is anodized at 40 V and it forms nanoporous structures when it is anodized at 60 V. The anodized oxides contained different phases of ZrO_2, WO_3, and ZrW_2O_8.

Cyclic voltammetry tests were performed in three different electrolytes and values as high as 60 mF/cm^2 of anodized substrate are reported for the capacitance of the material in 1M

H_2SO_4. Cycling the material 1000 times noticeably improved the capacitance due to the process exposing more surface area for capacitance reactions. Additionally, extended cycling tests were performed and it was discovered that the presence of ZrW_2O_8 improved the stability of the mixed oxide during extended cycling periods. The exact mechanism that occurred is not fully understood and further investigation is recommended.

Large concentrations of charge defects were also reported for this material. Annealing the samples generally increased the number of charge defects. The mixed oxide demonstrated significant power density and energy density to merit further ultracapacitor testing.

6. References

[1] S. Sarangapani, B.V. Thilak, C. P. Chen, *J. Electrochem. Soc.* 143 (1996) 3791.

[2] J. P. Zheng, Electrochem. *Solid-State Lett.* 2 (1999) 359.

[3] Y. U. Jeong, A. Manthiram, *J. Electrochem. Soc.* 149 (2002) A1419 – A 1422.

[4] J. Chang et al., *Electrochim. Acta* 53 (2007) 695.

[5] K. Kordesch, J. Gsellmann, M. Peri, K. Tomantschger, and R. Chemelli, *Electrochim. Acta* 26 (1981) 1495.

[6] J. Wang, J. Polleux, J. Lim, B. Dunn, *J. Phys. Chem.* 111 (2007) 14925.

[7] Y. Xie, L. Zhou, C. Huang, H. Huang, J. Liu, *Electrochim. Acta,* 53 (2008) 3643.

[8] Y-G Wang, X-G. Zhang, *J. Electrochem. Soc.* 152 (2005) A671.

[9] Q. Wang, Z. Wen, J. Li, *Adv. Functional Materials* 16 (2006) 2141 – 2146.

[10] H. Habazaki, S. Koyama, Y. Aoki, N. Sakaguchi, S. Nagata, *ACS Appl. Mater. Interfaces* 3 (2011) 2665–2670.

[11] F. Muratore, A. Baron-Wieche´c, A. Gholinia, T. Hashimoto, P. Skeldon, G.E. Thompson, Comparison of nanotube formation on zirconium in fluoride/glycerol electrolytes at different anodizing potentials, Electrochim. Acta 58 (2011) 389–398.

[12] W. Li, J. Li, X. Wanga, S. Luoa, J. Xiaoa, Q. Chen, Visible light photoelectrochemical responsiveness of self-organized nanoporous WO3 films, Electrochim. Acta 56 (2010) 620–625.

[13] I.M. Szilágyi, J. Madarász, G. Pokol, P. Király, G. Tárkányi, S. Saukko, J. Mizsei,A.L. Tóth, A. Szabó, K. Varga-Josepovits, Stability and controlled composition of hexagonal WO3, Chem. Mater. 20 (2008) 4116–4125.

[14] I.M. Szilágyi, B. Fórizs, O. Rosseler, A. Szegedi, P. Németh, P. Király, G. Tárkányi,B. Vajna, K. Varga-Josepovits, K. László, A.L. Tóth, P. Baranyai, M. Leskelä, WO3 photocatalysts influence of structure and composition, J. Catal. 294 (2012)119–127.

[15] J.S. da Cruz, M.A. Fraga, S. Braun, L.G. Appel, Thermal spreading of WO3 onto zirconia support, Appl. Surf. Sci. 253 (2007) 3160–3167.

[16] G.E. McGuire, G.K. Schweitzer, T.A. Carlson, Core electron binding energies in some group IIIA, VB, and VIB compounds, Inorg. Chem. 12 (1973) 2450–2453.

[17] T.L. Barr, Recent advances in X-ray photoelectron spectroscopy studies of oxides, J. Vac. Sci. Technol. A 9 (1991) 1793.

[18] M.J. Guittet, J.P. Crocombette, M. Gautier-Soyer, Bonding and XPS chemical shifts in ZrSiO4 versus SiO2 and ZrO2: charge transfer and electrostatic effects, Phys. Rev. B 63 (2001) 125117.

[19] W. Grünert, E.S. Shpiro, R. Feldhaus, K. Anders, G.V. Antoshin, K.M. Minachev, Reduction behavior and metathesis activity of WO3/Al2O3 catalysts: I. An XPS investigation of WO3/Al2O3 catalysts, J. Catal. 107 (1987) 522.

[20] M.A. Cortes-Jacome, C. Angeles-Chavez, X. Bokhimi, J.A. Toledo-Antonio, Generation of WO3–ZrO2 catalysts from solid solutions of tungsten in zirconia, J. Solid State Chem. 179 (2006) 2663–2673.

[21] D.-Y. Cho, S.-J. Oha, Y.J. Chang, T.W. Noh, R. Jung, J.-C. Lee, Role of oxygen vacancy in HfO2/SiO2/Si(1 0 0) interfaces, Appl. Phys. Lett. 88 (2006) 193502.

[22] L. Xu, Z. Wu, W. Zhang, Y. Jin, Q. Yuan, Y. Ma, W. Huang, Oxygen vacancy-induced novel low-temperature water splitting reactions on FeO(1 1 1) monolayer-thick film, J. Phys. Chem. C 116 (2012) 22921–22929.

[23] J. Li, J. Zhu, X. Liu, Synthesis, characterization and enhanced gas sensing performance of WO3 nanotube bundles, New J. Chem. 37 (2013) 4241–4249.

[24] F. Muratore, A. Baron-Wiechec, T. Hashimoto, A. Gholinia, H. Habazaki, P. Skeldon, G.E. Thompson, Porous anodic film growth on a Zr–W alloy: corrosion, passivation, and anodic films, Electrochem. Solid State Lett. 15 (2012) C8–C11.

[25] E. Deltombe, N. de Zoubov, M. Pourbaix, Section 10.3: tungsten, Atlas Electrochem. Equilib. Aqueous Solutions (1974) 280–285.

[26] K.C. Leonard, W.E. Suyama, M.A. Anderson, Evaluating the electrochemical capacitance of surface-charged nanoparticle oxide coatings, Langmuir 28 (2012) 6476–6484.

[27] B.E. Conway, Transition from supercapacitor to battery behavior in electrochemical energy storage, J. Electrochem. Soc. 138 (1991) 1539–1548.

[28] D. Vanderbilt, X. Zhao, D. Ceresoli, Structural and dielectric properties of crystalline and amorphous ZrO2, Thin Solid Films 486 (2005) 125–128.

[29] A. Mansingh, M. Sayer, J.B. Webb, Electrical conduction in amorphous WO3 films, J. Non-Cryst. Solids 28 (1978) 123–137.